Hall A Annual Report
2011

Edited by Seamus Riordan & Robert Michaels

Contents

1 Introduction **7**

2 General Hall Developments **9**
2.1 The Compton Polarimeter Upgrade . . . 9
2.1.1 Overview . . . 9
2.1.2 Fabry-Perot Cavity . . . 9
2.1.3 Electron Detector . . . 14
2.1.4 Photon Detector . . . 16
2.1.5 Recent Results . . . 16
2.1.6 12 GeV Upgrade . . . 16
2.1.7 Conclusion . . . 17
2.2 Super Bigbite Developments . . . 19
2.3 Improving HRS DAQ Deadtime . . . 20
2.3.1 Deadtime Overview . . . 20
2.3.2 Improving Deadtime . . . 20
2.3.3 Deadtime Testing . . . 20

3 Summaries of Experimental Activities **22**
3.1 E97-110 - GDH . . . 22
3.1.1 The experiment . . . 22
3.1.2 **Analysis Progress** . . . 22
3.1.3 Remaining tasks. . . . 23
3.1.4 Outlook. . . . 23
3.2 E00-110, E07-007, E08-025 - DVCS . . . 26
3.2.1 Update on the analysis of experiments E07-007 (Hydrogen) and E08-025 (Deuterium) . . . 26
3.2.2 Latest physics result from experiment E00-110 . . . 27
3.3 E04-007 - pi0 . . . 29
3.3.1 Introduction . . . 29
3.3.2 Experimental Results . . . 29
3.4 E05-009 - HAPPEX-III . . . 32
3.5 E05-015 - A_y in ^{3}He(e,e') . . . 34
3.6 E05-102 - A_x, A_z in ^{3}He(e,e'd) . . . 38
3.7 E06-002 - PREX . . . 41
3.8 E06-010 - Transversity . . . 45
3.8.1 Introduction . . . 45
3.8.2 Inclusive Hadron Production . . . 46
3.9 E06-014 - d_2^n . . . 50
3.9.1 The Experiment . . . 50
3.9.2 Analysis Progress: Target and Beam . . . 52
3.9.3 Analysis Progress: LHRS . . . 54
3.9.4 Analysis Progress: BigBite . . . 56
3.10 E07-006 - SRC . . . 61
3.11 E07-013 - A_y in DIS ^{3}He(e,e') . . . 63
3.12 E08-005 - A_y in ^{3}He(e,e'n) . . . 66
3.12.1 Progress of $^3\mathrm{He}^{\uparrow}(e,e'n)$ Target Single-Spin Asymmetries . . . 66
3.13 E08-009 - ^{4}He . . . 68
3.13.1 Motivation . . . 68
3.13.2 The experiment . . . 69
3.13.3 Status of the Analysis . . . 69
3.14 E08-010 - N - Delta . . . 71
3.14.1 Introduction . . . 71
3.14.2 The Experiment . . . 72

3.15 E08-011 - PVDIS . . . 75
3.16 E08-014 - $x > 2$ . . . 80
3.16.1 Motivations . . . 80
3.16.2 Analysis status . . . 80
3.17 E08-027 - g_2^p . . . 84
3.17.1 Introduction . . . 84
3.17.2 The Experiment . . . 84
3.17.3 Recent Progress . . . 86
3.18 E12-10-009 - APEX . . . 89
3.18.1 Introduction . . . 89
3.18.2 Test Run Results and Future Plans . . . 91

4 Publications **94**

5 Theses **95**

6 Hall A Collaboration Member List **96**

List of Figures

1 *Schematic layout of the Hall A Compton polarimeter.* . . . 9
2 Optical setup of the green Compton polarimeter. . . . 10
3 The green Fabry-Perot cavity installed in Hall A Compton Polarimeter. . . . 11
4 First lock acquisition of the newly installed green Fabry-Perot cavity in Hall A seen as a steady CW laser beam spot transmitted through the cavity. . . . 12
5 Lock acquisition with 9 kW intra-cavity power in the green cavity. The The magenta line shows the power in the cavity whereas the red line show the power reflected by the cavity. . . . 12
6 Characteristic decay time of the cavity power measured with a photodiode monitoring the power transmitted from the cavity. The measured decay time of 28.46 μs corresponds to a cavity finesse of 26,825. 13
7 The silicon microstrip electron detector inside the vacuum chamber along with the additional Chromax beam viewer. . . . 14
8 Schematic layout of the cosmic test setup for the Si micro-strip detectors at Clermont Ferrand University . . . 15
9 Pulse height spectra obtained from the 0.5 mm thick (blue) and 1 mm thick (red)Si microstrip detectors with cosmic rays . . . 15
10 The GSO calorimeter installed in the Hall A Compton Polarimeter . . . 16
11 Electron beam polarization results from the PReX experiment obtained with the upgraded Compton polarimeter . . . 17
12 Model of the 12 GeV Compton polarimeter in Hall A Beam line. Shown in blue are the dipole magnets of the chicane, where the two middle dipoles are being raised by 82 mm for the 12GeV Upgrade . . . 18
13 LHRS: Deadtime with model prediction . . . 21
14 Preliminary unpolarized ^{3}He cross section (top) versus W. Acceptance corrected ^{3}He yield (bottom) versus ν after secondary acceptance corrections have been applied. . . . 24
15 Carbon cross section comparison for 3.775 GeV, 9° data: cross section from data (Top-left panel), elastic tail subtraction (Top-right panel), data and simulation cross section comparison (Bottom-left panel) and the cross section ratio of data to simulation (Bottom-right panel). . . . 25
16 Left: Total π^0 cross section ($\sigma_T + \varepsilon_l \sigma_L$) differential in t as a function of $t_{min} - t$ at $Q^2 = 1.9\,\mathrm{GeV}^2$ (black hollow circles) and $Q^2 = 2.3\,\mathrm{GeV}^2$ (red solid circles). Right: Harmonic components of the π^0 cross section ($\sigma_{TL}, \sigma_{TT}, \sigma_{TL'}$, top to bottom) differential in t as a function of $t_{min} - t$ at $Q^2 = 1.9\,\mathrm{GeV}^2$ (black hollow circles) and $Q^2 = 2.3\,\mathrm{GeV}^2$ (red solid circles). The bands are results from the fits of those components with their leading order in θ^{CM}, the angle of the pion w.r.t the virtual photon. The curves represent the model from J.-M. Laget [2], for $Q^2 = 1.9\,\mathrm{GeV}^2$ (dashed black curve) and for $Q^2 = 2.3\,\mathrm{GeV}^2$ (red solid curve). . . . 27
17 Angular distributions of $p\pi^0$ C.M. cross sections. . . . 30
18 Beam asymmetry measurements . . . 30
19 ^{3}He target performance during the A_y experiment . . . 35
20 The preliminary ^{3}He target single-spin asymmetry from left-arm data(top plot) and right-arm data (bottom plot) at Q^2= 0.98 GeV^2. The solid lines indicate a constant fit to the target single-spin asymmetry for each run. . . . 36
21 [Left] Schematics of the BigBite sieve-slit collimator. [Right] Reconstructed sieve pattern. The leftmost holes are missing due to geometrical obstacles between the target and BigBite. . . . 38
22 [Top-Left] Momentum losses of protons and deuterons inside the target and the total momentum losses up to the MWDCs. [Top-Right] Quality of reconstructed momentum for elastic protons and deuterons. If energy losses are not taken into account, two peaks are visible (center and right histograms summed to the full curve). With proper inclusion of energy losses both peaks merge into one (left histogram), resulting in better momentum resolution. [Bottom] Energy losses in the E-plane as a function of particle momentum for ^{3}He data. The deuterons can be clearly distinguished from the protons. The measurements agree well with the expectation (dot-dashed line). . . . 39

23 Double spin asymmetries in the quasi-elastic $^3\vec{\mathrm{He}}(\vec{e},e'p)$ process for two different target settings. In the longitudinal configuration the target spin was oriented in the direction of the beam. In the transverse configuration the target spin was pointing to the left of the beam direction. The asymmetries were measured at two different momentum transfers: [Left] $Q^2 = 0.35\,\mathrm{GeV}^2/c^2$, [Right] $Q^2 = 0.25\,\mathrm{GeV}^2/c^2$. 40
24 Result of this experiment (red square) vs neutron point radius R_n in ^{208}Pb. Distorted-wave calculations for seven mean-field neutron densities are circles, while the diamond marks the expectation for $R_n = R_p$. The blue squares show plane-wave impulse approximation results. 42
25 The PREX asymmetry for the PREX-I data, the PREX-II projections (new proposal for PAC38), and 8 selected models. Also shown is the asymmetry for the hypothesis that the neutron radius is the same as the proton radius. The references are shown in the PREX-II proposal. 43
26 The results of Collins and Sivers moments of neutron are shown. The error bars represent the statistical uncertainties. The different sources of experimental systematic uncertainties are shown as a red band and systematics due to fitting an angular modulation to the asymmetry is shown in blue band. The magenta curve is the theoretical calculations from Anselmino *et al.* [5, 6] 46
27 Neutron $A_{LT}^{cos(\phi_h-\phi_S)}$ azimuthal asymmetry for positive(left) and negative (right) charged pions vs Bjorken x. 47
28 Reconstructed Cerenkov angle in the RICH detector for negative (top left) and positive (top right) HRS polarity. The bottom plots show the angle after χ^2 probability cut on Kaon angle reconstruction as described in [13] 48
29 The phase space of P_T vs. x_F for different particles in the left HRS and in the BigBite. The BigBite phase space is shown in different momentum bins. 49
30 Preliminary ^{3}He SSA of π^+, π^- and proton obtained from HRS (p_0=2.35 GeV/c) for transverse (left) and vertical (right) target spin states. The asymmetries are corrected for target polarization but not corrected for the nitrogen dilution. The error bars represent only statistical uncertainties. 49
31 E06-014:Coverage 51
32 E06-014:World d_2^n data 52
33 E06-014:^{3}He densities 53
34 E06-014:Target polarization 54
35 E06-014:Beam polarization 55
36 E06-014:SAMC 56
37 E06-014 LHRS Cross Sections 57
38 BB Nitrogen dilution factor 57
39 E06-014:Physics asymmetries 58
40 E06-014:A1 59
41 E07006: Missing Momentum Distributions. 61
42 ^{3}He target performance for vertical production data runs (plotted versus arbitrary run numbers). . . . 63
43 Contamination estimates of π^- (from negative polarity runs) and π^+ (from positive polarity runs) for six data bins. 64
44 Photo-induced positron contamination for six data bins. Only the central values are shown. Error bars are still to come, see 'Remaining Tasks'. 64
45 A_y^{raw} on ^{3}He for six W bins. Contamination corrections are applied; N_2 dilution is not. The red band on the right side plot corresponds to the BigBite systematic uncertainties. 65
46 quasi-elastic: Q2 1.0 Basic 66
47 quasi-elastic: Q2 1.0 ToF with vetoes 67
48 quasi-elastic: Q2 1.0 ToF with vetoes Bg Subtracted 67
49 quasi-elastic: Q2 0.5 ToF with vetoes Bg Subtracted 67
50 quasi-elastic: Q2 0.1 ToF No vetoes Bg Subtracted 67
51 E08009: Sample of Missing Energy Spectra for different Missing Momenta. 70
52 The effect of the pionic cloud to the resonant amplitudes as predicted by the Sato-Lee calculation [21]. Solid line includes the pion cloud contribution while the dashed line neglects the pion cloud effect. . . 72
53 The CMR at the low momentum transfer region. The projected E08-010 uncertainties are presented along with the world data and the theoretical model predictions 73

54 Overall statistical quality of the data after dithering correction. From top to bottom: kinematics #1 taken on the left HRS, kinematics #2 taken on the left HRS, and kinematics #2 taken on the right HRS. All asymmetries shown are blinded. 77
55 Preliminary results on the electron asymmetry at $Q^2 = 1.925$ (GeV$/c)^2$. All asymmetries shown are blinded. 78
56 Preliminary results from Hall C experiment E02-019 [4] 81
57 E08014-opt: HRS optics calibration. 82
58 E08014-calo: Calorimeter calibration. 83
59 E08014-ca: Isospin study statistical precision (blinded). 83
60 **Top**: Full kinematic coverage. **Bottom**: Reduced kinematics assuming Feb. 14 start date and use of the Hall B magnet coil. 85
61 E08-027 installation in Hall A. 86
62 E08-027 projection for the LT polarizability showing the data point at $Q^2 = 0.32$ that will be lost. . . 87
63 The reach of the APEX experiment (blue contour), existing constraints (gray shaded and hatched regions), and other proposed experiments (colored lines). The region in which an A' could explain the anomalous measurement of the muon $g-2$ is shaded in green. 90
64 The layout of the APEX experimental setup. 91
65 The components of the target for the APEX experiment. 91
66 Upper panel: The invariant mass spectrum of e^+e^- pair events in the final event sample (black points, with error bars), accidental e^+e^- coincidence events (blue short-dash line), and the QED calculation of the trident background added to the accidental event sample (red long-dash line). Lower panel: the bin-by-bin residuals with respect to a 10-parameter fit to the global distribution (for illustration only, not used in the analysis). 92
67 The 90% confidence upper limit on α'/α versus A' mass for the APEX test run (solid blue). Also shown are existing 90% confidence level limits from the muon anomalous magnetic moment a_μ (fine hatched) [7], KLOE (solid gray) [8], the result reported by Mainz (solid green) [9], and an estimate using a BaBar result (wide hatched) [2, 3, 10]. Between the red line and fine hatched region, the A' can explain the observed discrepancy between the calculated and measured muon anomalous magnetic moment [7] at 90% confidence level. The full APEX experiment will roughly cover the entire area of the plot. 93

1 Introduction

Robert Michaels

2011 has been a productive year in Hall A, with several experiments running in the Spring, followed by a 6-month shutdown during which we installed the g2p and GEp experiments, expected to be the last Hall A experiments of the 6 GeV era. From this past year, 18 new publications related to Hall A experiments were authored by members of the Hall A collaboration, a significant achievement and a sign of the vigor of our collaboration. It was also a year of transition, as I became the acting Hall A leader on March 1. It has been a humbling challenge to fill the shoes of Kees de Jager, striving to maintain his standards of excellence. In this acting position, I have benefited greatly from the advice, patience, and support of the Hall A staff and the user community, and I wish to thank you all.

The year began with a series of experiments that use the standard Hall A equipment. The Exclusive Study of Deuteron Electrodisintegration near Threshold, Experiment E08008 (B. Norum, W. Bertozzi, S. Gilad, K. Wang), was completed on Feb 22, followed by the Measurement of the Coulomb Quadrupole Amplitude in the Delta Resonance Region, Experiment E08010 (N. Sparveris, S. Gilad, D. Higinbotham, A. Sarty), which finished on March 9. In mid-April we also completed the short run of the Experiment E08009, a Study of ^{4}He Nuclei Through Response Separations at High Momentum Transfers (A. Saha, K. Aniol, F. Benmokhtar, S. Gilad, D. Higinbotham). All three experiments were completed successfully. Right after E08010 we started the first part of E07006 (E. Piasetzky, S. Gilad, D. Higinbotham, V. Sulkosky, J. Watson), a Study of the Short-Range Correlations in Nuclei via Triple Coincidence (e,e'pN). On April 16, we switched to the "$x > 2$" Experiment E08014, a Study of Short-Range Correlations in Inclusive Scattering (P. Solvignon-Slifer, J. Arrington, D. Day, D. Higinbotham), and then on May 8 we switched back to E07006 for the last five days of beam time. While this switching back and forth was not optimally efficient, it was done to reduce the risk to the beam time owing to the unusual budgetary process underway at the time.

On May 13, we began our 6 Month Shutdown, to complete several upgrades for the 12 GeV Project, while in Hall A we installed the g2p and GEp experiments, E08027 and E08007 respectively. The goals for the Accelerator Division during this shutdown included civil construction in the tunnel and beam switchyard, upgrades to the magnets and associated hardware, new RF zones in the linacs, and the installation of two new C100 cryomodules. All this was accomplished and the commissioning of the C100's is presently underway during beam study periods.

The upcoming experiments g2p (K. Slifer, A. Camsonne, J.P. Chen, D. Crabb) and GEp (R. Gilman, D. Higinbotham, G. Ron, J. Arrington, A. Sarty, D. Day) share a common setup. The installation involved extensive modification to the beamline in Hall A: new chicane magnets, the septum magnets to reach low Q^2, new low-current beam monitors, a local beam dump, as well as the UVa/JLab Polarized NH3 target. A technical review was conducted by a committee chaired by Nilanga Liyanage on May 6, 2011. The review identified several areas of concern which helped guide the efforts. Unfortunately, in September, as the polarized target was being tested with it's superconducting magnet at full current, it developed shorts to ground which were not reparable. The solution, being implemented at the present time, will be to use the magnet from the Hall B polarized proton target. As I write this report, the target is expected to be ready by February 15, at which point we will start the two experiments. Meanwhile, the experiments have had a successful 10-day commissioning period just before Christmas, in which they commissioned several of the new beamline elements, the septum, a new 3rd-arm detector for monitoring polarization, and the HRS detectors, in addition to taking data to characterize the optics of the HRS+septum and a parasitic test of Cherenkov detector components for future use. Many people have contributed to this effort, but let me bring particular attention to the outstanding efforts of Jian-Ping Chen (Project Manager), Tim Michalski (Lead Engineer for the beamline), Robin Wines (Lead Hall A Engineer), Christopher Keith (Head of Target Group), and Ed Folts (Hall A Work Coordinator) and their respective groups.

In October, the DOE conducted a review of the SuperBigbite Spectrometer (SBS) Program. The program consists of a set of three projects that are centered around capital equipment investments related to new experimental capabilities. The review went very well on the scientific and technical merits, but needed improvement on the management aspects. The program management team, consisting of John LeRose (Program Manager), the principal scientists of the SBS and me, worked together with the Director's Office to improve the program management plan (PMP), and a revised PMP was submitted to DOE on Dec 27. We are optimistic this will be accepted.

In the summer, PAC38 considered new proposals and completed the grading of existing proposals. Hall A did quite well; the PAC report is available on the User Liaison's web page. In the Fall of 2011, the Hall A Coordinating Committee appointed a special committee, chaired by Professor Ron Gilman, for recommending a schedule for the commissioning and early running in the 12 GeV era. I greatly appreciate the hard work this committee put into this report. At present, the schedule is being formulated in conjunction with Rolf Ent, Arne Freyberger, and JLab management. It is clear that we have an exciting and vibrant physics program ahead of us in Hall A, and I am excited about the 12 GeV era.

Finally, on a sad note, we mourned the passing away of our dear friend and colleague Arun Saha on May 9 of this year. He will be remembered for his gentle kindness and for his many contributions to the Hall A program.

2 General Hall Developments

2.1 The Compton Polarimeter Upgrade

Contributed by Sirish Nanda

2.1.1 Overview

The Hall A Compton Polarimeter provides electron beam polarization measurements in a continuous and non-intrusive manner using Compton scattering of polarized electrons from polarized photons. A schematic layout of the Compton polarimeter is shown in Fig.1. The electron beam is transported through a vertical magnetic chicane consisting of four dipole magnets. A high-finesse Fabry-Perot (FP) cavity located at the lower straight section of the chicane with the cavity axis at an angle of 24 mr with respect to the electron beam, serves as the photon target. The electron beam interacts with the photons trapped in the FP cavity at the Compton Interaction Point (CIP) located at the center of the cavity. The Compton back-scattered photons are detected in an electromagnetic calorimeter. The recoil electrons, dispersed from the primary beam by the third dipole of the chicane are detected in a silicon micro-strip detector. The electron beam polarization is deduced from the counting rate asymmetries of the detected particles. The electron and the photon arms provide redundant measurement of the electron beam polarization.

In the recent years the Compton polarimeter has undergone a major upgrade[1] to green optics, in order to improve polarimetry performance at lower energies to address the needs of demanding parity violating experiments such as PReX[3]. The main parameters of the green Compton upgrade are shown in Table.1. The conceptual design of the green upgrade utilizes much of the the existing infrastructure of the present Compton polarimeter. The FP cavity has been upgraded to a high power 532 nm system replacing the original Saclay built 1064 nm cavity. In addition, the electron detector, photon calorimeter, and data acquisition system have been upgraded to achieve beam polarimetry accuracy of 1% at 1 GeV beam energy. The new subsystems have been installed and commissioned successfully in Hall A beam line in 2010. Electron beam polarimetry was carried out successfully during the PReX experiment with the upgraded polarimeter. Preliminary results indicate 1.5% accuracy in the electron beam polarization has been achieved.

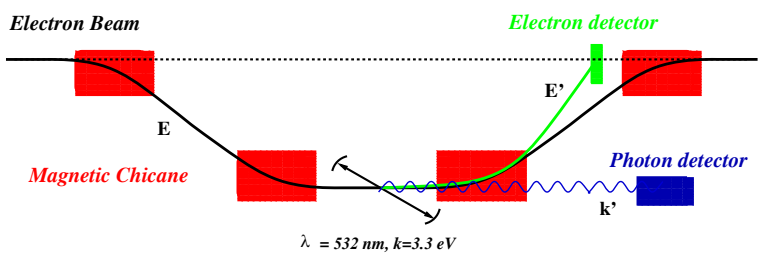

Figure 1: *Schematic layout of the Hall A Compton polarimeter.*

Additionally, as part of the 12 GeV upgrade CEBAF, the Hall Compton polarimeter will be upgraded to accommodate 11 GeV beam envisioned for Hall A. At present, designs for the 12GeV Upgrade of the Compton Polarimeter are being finalized in preparation for construction to commence soon.

2.1.2 Fabry-Perot Cavity

The heart of the upgrade plan is to replace the infrared cavity with a high gain 532 nm green cavity capable of delivering 3 kW of intra-cavity power. Recent advances in the manufacturing of high reflectivity and low loss dielectric mirrors as

Parameter	Previous	Upgrade
Wavelength (nm)	1064	532
Cavity Power (W)	900	3000
FOM ($\sigma.A^2$) @.85Gev	0.57	2.2
Energy Range (GeV)	3 - 6	0.8 - 11
$\delta P_e/P_e$ @.85Gev	-	1%

Table 1: Main deign parameters of the green Compton polarimeter upgrade compared to the present infra-red system

well as availability of narrow line width green lasers facilitates the feasibility of our challenging design goal. High gain cavities at 532 nm have been successfully constructed by the PVLAS[4] group with geometry and gain comparable to our proposed design. A schematic layout of the optical setup for the upgrade is shown in Fig. 2.

Our solution for the green laser system begins with a narrow line CW fiber coupled Nd:YAG seed laser operating at 1064 nm (Innolight Mephisto S [5]). The beam from the seed laser is then amplified by a Ytterbium doped fiber amplifier (IPG Photonics[6]) which can produce up to 10 W of CW beam while maintaining the line-width and the tunability of the seed laser. The amplified infrared beam is then shaped with lenses L_a and L_b to pump a Periodically Poled Lithium Niobate (PPLN) crystal supplied by HC Photonics [7]. The PPLN crystal is placed in a temperature controlled housing equipped with a thermo-electric heat pump to maintain the temperature of the PPLN crystal at about 60° with better than $.05^o$ regulation. This temperature corresponds to the quasi-phase matching condition for the PPLN necessary to generate the second harmonic of the pump beam at 532 nm. Typically about 2 W of 532 nm beam is generated with about 5 W of 1064 nm pump beam.

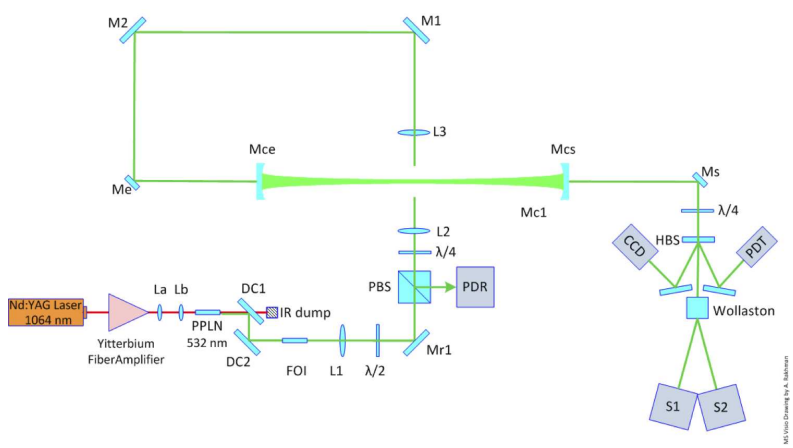

Figure 2: Optical setup of the green Compton polarimeter.

The green beam from the PPLN laser is then separated from the infrared pump with a pair of dichroic mirrors (DC1 and DC2), and transported through polarization conditioning optics and mode-matching lenses (L_1 - L_3) to produce circularly polarized light with the same Gaussian beam profile as the TEM_{00} mode of the FP cavity. The beam is then injected to the 850 mm long cavity using conventional beam steering optics to properly couple the beam to the cavity. The cavity, constructed out of Invar, has dielectric mirrors mounted on adjustable gimbaled mounts with special ports for the transport of the electron beam. The structure, held in ultra-high vacuum, is part of the electron beam line in

Hall A.

Part of the laser beam reflected from the cavity is steered by a polarizing beam splitter to a photo-diode receiver PDR. The PDR signal is used to lock the cavity on resonance using the well known Pound-Drever-Hall locking scheme. The part of the laser beam transmitted through the cavity is converted back to linearly polarized light and analyzed in a Wollaston polarimeter. The intensities of the analyzed horizontal and vertical polarization components of the beam are measured in integrating spheres S_1 and S_2. In addition, a small part of the transmitted beam, separated with a holographic beam splitter, is used for beam monitoring instruments.

The green laser systems and FP cavity have been in development in the Compton Lab for the past few years with participation from many graduate students from collaborating institutions. The development work was successful in late 2009 with stable lock acquisition with dielectric mirrors supplied by Advanced Thin Films[8] (ATF) and home-made locking electronics. The system was then installed and commissioned in the Hall A beam line in early 2010 in preparation for the PReX experiment. During the commissioning, calibration of the laser beam power and polarization transfer functions were carried out in order to accurately determine the power and polarization of the light trapped inside the cavity. Shown in Fig.3 is the newly installed cavity on the optics table in the Hall A beam line. Thorough calibration of the laser beam power and polarization transfer functions were carried out during the commissioning. Using the established electronics and instrumentation in the Hall, cavity lock was acquired at 2 kW power in Hall A. Shown in Fig. 4 is the laser beam sport transmitted through the cavity becoming an intense CW beam spot upon successful lock acquisition.

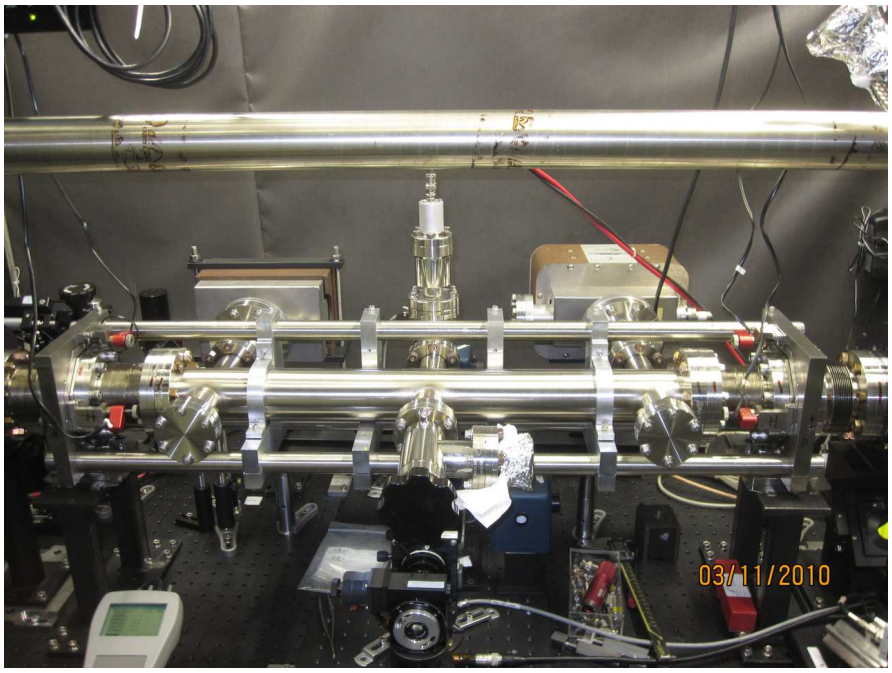

Figure 3: The green Fabry-Perot cavity installed in Hall A Compton Polarimeter.

Following the successful running of the Compton polarimeter for the PReX and DVCS experiments in 2011, the green cavity was dismantled in order to change the cavity mirrors to newer mirrors supplied by ATF with the goal of doubling the power in the cavity to more than 5 kW. During this down time, the PPLN setup was realigned to restore its conversion efficiency. The power and polarization transfer functions were measured again. With the entire system retuned, lock was acquired in the cavity with new mirror at 9 kW , far exceeding our expectation. Shown in Fig. 5 are strip-charts of various cavity parameters as a function of time during this lock acquisition. The magenta line shows the power in the cavity whereas the red line shows the power reflected by the cavity, both making a sharp transitions upon lock acquisition.

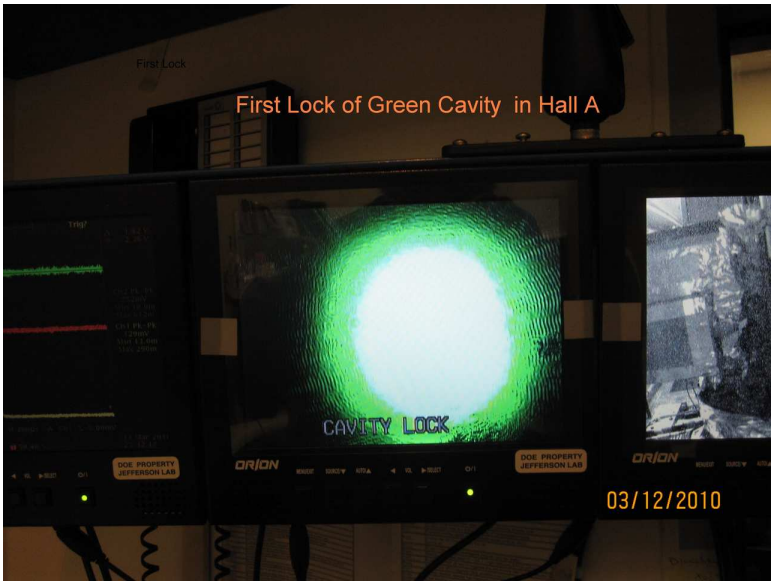

Figure 4: First lock acquisition of the newly installed green Fabry-Perot cavity in Hall A seen as a steady CW laser beam spot transmitted through the cavity.

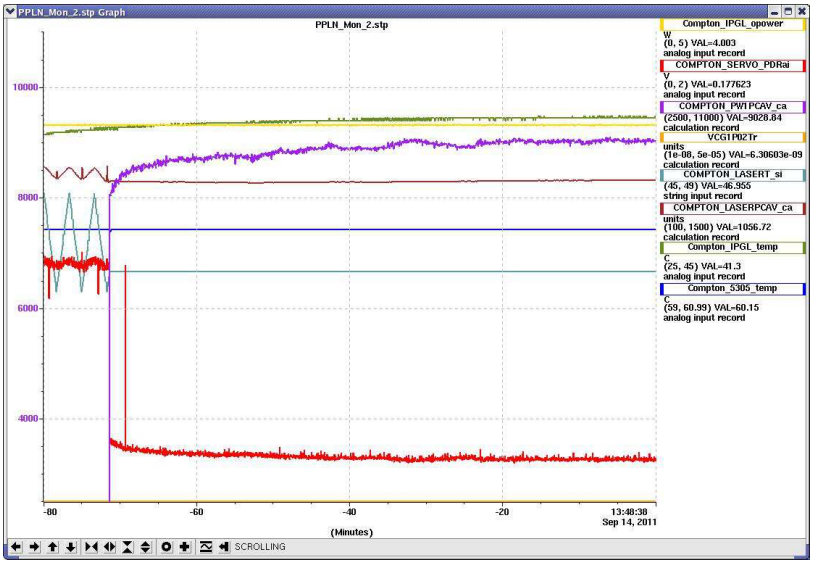

Figure 5: Lock acquisition with 9 kW intra-cavity power in the green cavity. The The magenta line shows the power in the cavity whereas the red line show the power reflected by the cavity.

Decay time of the cavity was measured by monitoring the power of the beam transmitted from the cavity with a fast photodiode after turning off the locking servo electronics. The transmitted power as a function of time as recorded by a digital storage oscilloscope is shown in Fig. 6. The measured decay time of 28.46 μs corresponds to a cavity finesse of 26,825. We further measure a transmittance and loss of 76 and 14 ppm as opposed to our specification of 80 and 10 ppm, respectively.The specifications and the measured parameters for the ATF mirrors are summarized in Table.2. The power gain achieved in the cavity was about 10^4.

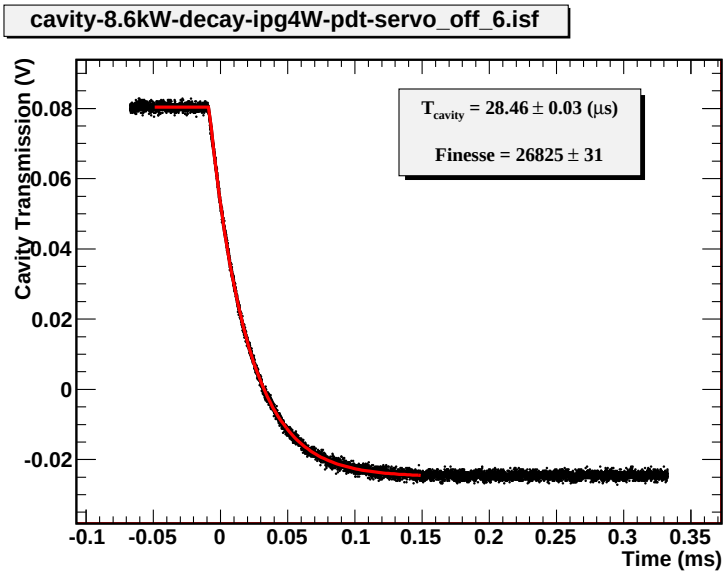

Figure 6: Characteristic decay time of the cavity power measured with a photodiode monitoring the power transmitted from the cavity. The measured decay time of 28.46 μs corresponds to a cavity finesse of 26,825.

	Specification	Measured
Diameter (mm)	7.75	
Thickness (mm)	4	
ROC (mm)	500	
Coating	HR@532 nm	
Transmittance (ppm)	80	76
Loss (ppm)	10	14
Finesse	28560	26825

Table 2: Performance of the ATF low loss mirrors

Test setup in the Compton Lab are being established in order to continue further development work on laser systems and FP cavities. In particular, the optical setup in the Compton lab is being modified to handle both 1064 nm infrared and 532 nm green beams with minimal setup changes. In the 12GeV era of CEBAF, the infrared system becomes competitive with green since the cavity power in the infrared is always going to be significantly higher, although the analyzing power is lower. The old Saclay cavity has been set up in the Compton Lab to provide a platform cavity development. The cavity ends have been modified with new mirror mounts to accommodate the smaller ATF mirrors while providing adjustment of their angular alignment. With the new mechanism the mirrors can be manually aligned with respect to the cavity axis prior to establishing vacuum in the cavity. Preliminary results indicate the alignment concept works well. However, vacuum load tests, lock acquisition, and stability tests with the new mechanics remains to be done. A new fiber amplifier with a maximum power of 30 W and a new PPLN setup have been brought into successful operation at the Compton Lab to facilitate for further studies in FP cavity development.

2.1.3 Electron Detector

The electron detector upgrade is being carried out by Laboratoire de Physique Corpusculaire IN2P3/Universit Blaise Pascal, Clermont-Ferrand. The new detector has 4 planes of 192 silicon micro-strip of 0.5 mm thickness with 240 μm pitch. The expected resolution is about 100 μm. A high precision vertical motion of 120 mm for the detector has been incorporated to the design so as to facilitate covering the recoil electrons corresponding to the Compton edge over a broad range of energies. The electron detector along with its associated mechanical structures and electronics were installed in Hall A in 2008. In subsequent commissioning trials, Compton scattering spectra were successfully obtained with 3 GeV electron beam and the old 1064 nm FP cavity. A clear Compton edge was observed at micro-strip number 14 corresponding to the expected position of the edge for 3 GeV electrons.

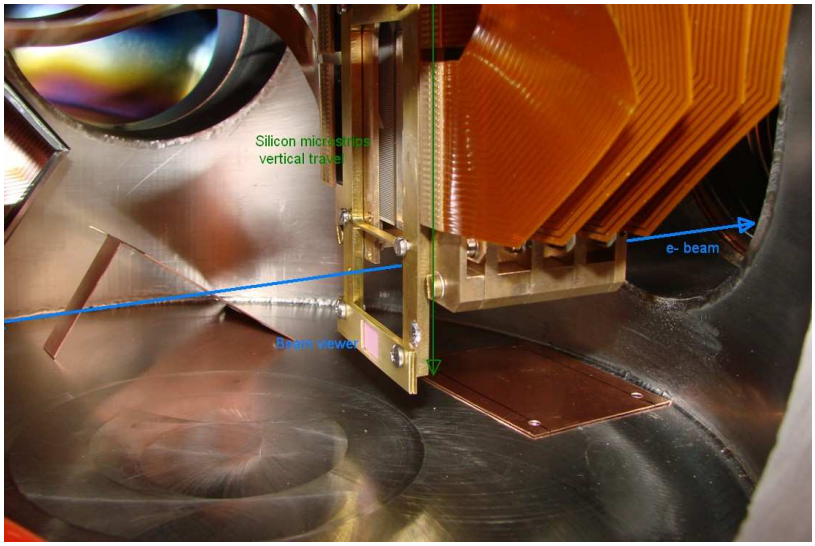

Figure 7: The silicon microstrip electron detector inside the vacuum chamber along with the additional Chromax beam viewer.

However, the detection efficiency of the micro-strips was found to be poor at about 10-20%. This is clearly unacceptable for successful operation of the electron detector. The primary reason for the poor efficiency was traced to poor signal-to-noise ratio encountered at the front-end electronics installed in the Hall. Whether signal from the micro-strips were inadequate or the noise in the electronics in the Hall A environment was excessive remained unclear. The detector was removed from the beam-line and sent back to Clermont-Ferrand in late 2010 to study the signal-to-noise characteristics of the micro-strips with a cosmic test setup. A schematic layout of the test set up consisting of two scintillation counters sandwiching the micro-strips under test is shown in Fig. 8. Only 32 micro-strips were used for the tests.

Meanwhile, a 1 mm thick Si micro-strip detector was ordered from Canberra systems to study its signal compared to the 0.5 mm micro-strips in the Clermont-Ferrand setup. After several fabrication delays, this detector was delivered to Clermont-Ferrand in November, 2011 for tests. Shown in Fig. 9 are pulse height spectra obtained from the 0.5mm (blue) and 1 mm (red) with cosmic rays. Both detector show clear peaks corresponding to energy deposited by minimum ionizing particles, above the noise pedestal. The 1 mm, as expected, shows about twice the signal compared to the 0.5 mm micro-strips. In principle, either detector should perform with good efficiency, unless the electronic noise or electron beam related noise in the Hall A environment is significantly worse than these bench test conditions. In such a case, the 1 mm thick detector is likely to perform with higher efficiency and is more desirable as the final design choice.

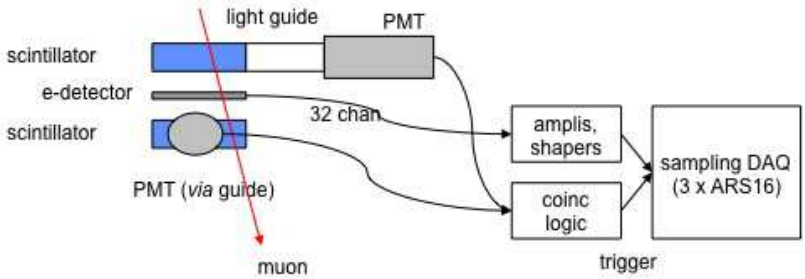

Figure 8: Schematic layout of the cosmic test setup for the Si micro-strip detectors at Clermont Ferrand University

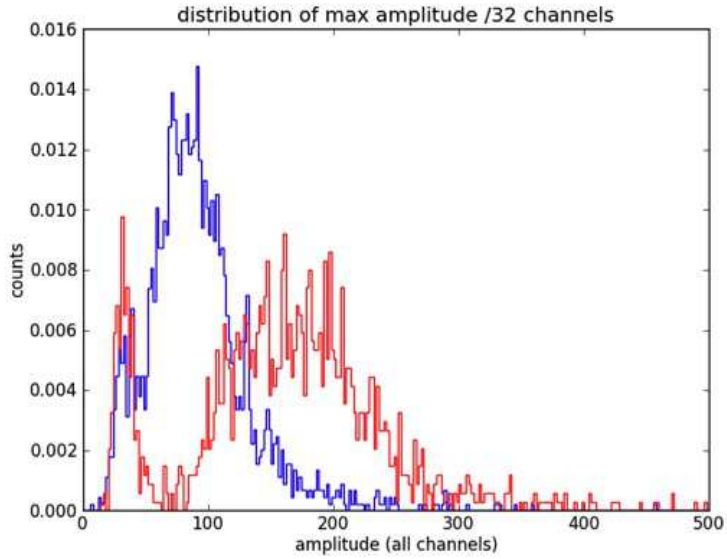

Figure 9: Pulse height spectra obtained from the 0.5 mm thick (blue) and 1 mm thick (red)Si microstrip detectors with cosmic rays

2.1.4 Photon Detector

The new photon detector, a Carnegie Mellon University (CMU) responsibility, consists of a single GSO crystal fabricated by Hitachi Chemicals Ltd, 60 mm in diameter and 150 mm in length. Following successful assembly and tests at CMU, The GSO calorimeter was installed (Fig. 10) and commissioned in Hall A beam line and commissioned in 2009. Driven by the needs of the PReX experiment the photon beam line was redesigned by CMU. The beam pipe was broadened to 1.5 inch from the existing 1 inch diameter to increase the acceptance for 1 GeV Compton scattering. In addition, a new adjustable lead collimator was designed for the GSO calorimeter. With the new hardware changes, satisfactory performance for the GSO calorimeter was obtained during the running of the Compton polarimeter during HAPPEX-III and PVDIS experiments during the latter part of 2009. Following the successful operation of the new green FP cavity, the GSO calorimeter was further tested to accommodate the higher cavity power and scattered photon energies. The FADC based integrating DAQ was fully operational for the PReX experiment.

Figure 10: The GSO calorimeter installed in the Hall A Compton Polarimeter

2.1.5 Recent Results

The Compton polarimeter was operated successfully during the recent PReX and DVCS experiments. Polarimetry with 1 GeV electron beam at 70 mA was successfully carried out during the PReX experiment. Illustrated in Fig. 11 is the polarization of the electron beam measured in the Compton polarimeter using the integrating GSO calorimeter. Some loss in cavity power was noticed as the experiment progressed. Examination of the cavity mirrors following the experiment suggest possible damage to the mirrors due to excessive electron beam related background.

2.1.6 12 GeV Upgrade

As part of the CEBAF 12GeV Upgrade, the Hall A Compton Polarimeter will be upgraded to accommodate 11 GeV beam. The present dipole magnets, the main transport elements of the electron beam line chicane, are configured to produce a 300 mm vertical displacement at 1.5 T corresponding to 8 GeV beam transport. We plan to retain the present magnets and simply elevate the lower section of the chicane to reduce the displacement to 218 mm. The scope of the upgrade (WBS 1.4.1.5.2) consists of reconfiguration the electron beam chicane, changes to the optical setup,

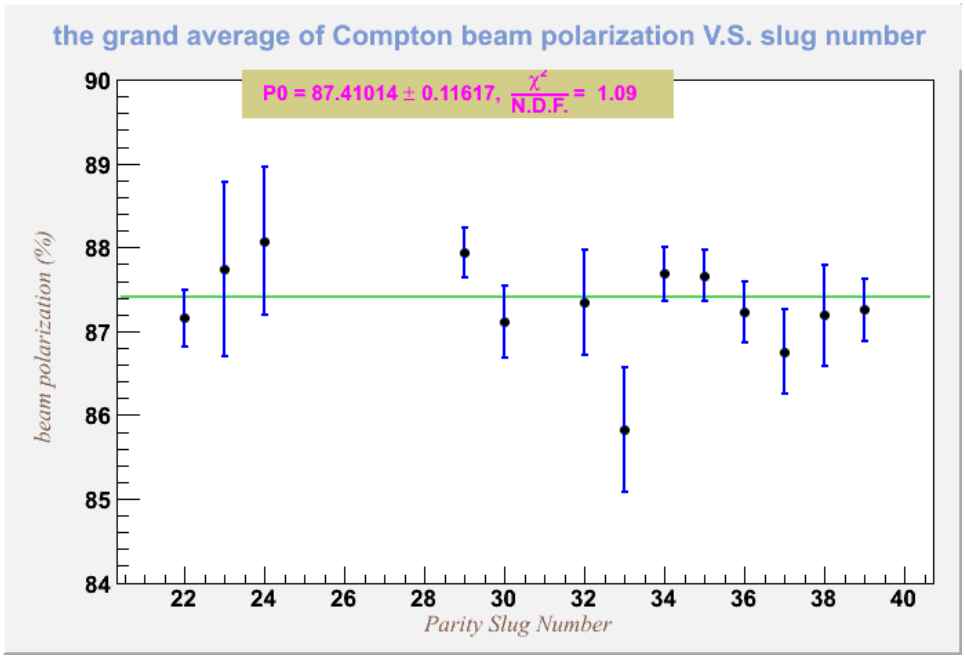

Figure 11: Electron beam polarization results from the PReX experiment obtained with the upgraded Compton polarimeter

electron and photon detectors to be compatible with 11 GeV configuration. Shown in Fig. 12 is a computer model of the 12GeV beam line.

Basic design of the reconfiguration has been completed. Fabrication of components will start in early 2012 with installation in the Hall scheduled to begin in summer 2012. The upgrade project is expected to be completed by October 2013.

2.1.7 Conclusion

The green laser upgrades of the Compton polarimeter for 6 GeV operations have been successfully completed. The upgraded polarimeter was put into operation successfully for the recent PReX and DVCS experiments. The green FP cavity far exceeds design goal by achieving upwards of 9 kW intra-cavity power. The green cavity along with the GSO photon calorimeter with integrating data acquisition system has provided the first set of high precision polarimetry results. Poor detection efficiencies in the silicon micro-strip electron detector are being investigated with bench tests with cosmic rays. Beam tests are scheduled during the upcoming g2p experiment to evaluate the performance of thicker micro-strip detector that shows promising results in the bench tests.

References

[1] S. Nanda and D. Lhuiellier, Conceptual Design Report for Hall A Compton Polarimeter Upgrade, Unpublished.

[2] G. Bardin et.al, Conceptual Design Report of a Compton Polarimeter for CEBAF Hall A, CEA, Saclay, France, Unpublished.

[3] Jlab Experiment E06002, Paul Souder, Robert Michaels, Guido Urciuoli spokespersons.

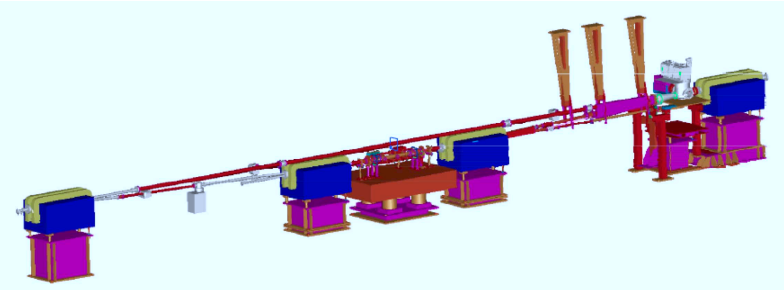

Figure 12: Model of the 12 GeV Compton polarimeter in Hall A Beam line. Shown in blue are the dipole magnets of the chicane, where the two middle dipoles are being raised by 82 mm for the 12GeV Upgrade

[4] M. Bregant *et al.*, arXIV:hep-ex/0202046 v1 28 Feb 2002.

[5] Innolight GmbH, http://www.innolight.de/

[6] IPG Photonics, http://www.ipgphotonics.com/

[7] HC Photonics, http://www.hcphotonics.com/

[8] Advanced Thin Films, http://www.atfilms.com/

2.2 Super Bigbite Developments

Contributed by John J. LeRose

The Super BigBite Spectrometer (SBS) concept is alive and well. In preparation for the October 13-14 DOE review the program was divided into three projects, each costing less than $2M. The three projects are:

- The first Project, **SBS Basic**, involves the acquisition of an existing magnet and the associated work of preparing it for use during the SBS research program. The effort includes modifications to the magnet, including machining a slot in the yoke for beam passage, field clamps, and a solenoid to reduce the transverse magnetic field on the beam line, the design and development of the infrastructure needed to run the magnet, and the construction of the platform on which it will stand.
- The second Project, **Neutron Form Factor**, involves the construction of twenty-nine GEM detector modules with associated front-end and DAQ modules to meet the requirements of the approved neutron form factor measurements (E12-09-016 and E12-07-109).
- The third and final Project, **Proton Form Factor**, involves the construction of thirty-five GEM detector modules with associated front-end and DAQ modules and the addition of pole shims for increased magnetic field integral to meet the requirements of the approved proton form factor measurements (E12-07-109).

The reviewers were extremely positive regarding the Physics potential of the proposed program, but wanted to see the management plan revised and improved. Subsequently, the Program Management Plan (PMP), which is actually three project management plans rolled into one, was thoroughly reworked and a formal document was submitted to DOE just before the New Year.

Independent of the DOE review process, pre-R&D work is ongoing at JLab and the University of Virginia, using Hall A funds, and in Rome using INFN funding. The bulk of the pre-R&D work centers around the development of the GEM detectors needed for the successful execution of the proposed experiments.

Interested parties are invited to visit the SBS webpage [1] for more information.

References

[1] http://hallaweb.jlab.org/12GeV/SuperBigBite/

2.3 Improving HRS DAQ Deadtime

Contributed by Ryan Zielinski and Vincent Sulkosky

2.3.1 Deadtime Overview

In a simple 1-trigger, non-prescaled system the DAQ deadtime is approximately

$$DT \approx D_r + D_c \,, \tag{1}$$

where D_r is the readout deadtime, and D_c is the conversion (frontend) deadtime [1]. Using Poisson probability theory, the two deadtime components can be broken down into two infinite sums:

$$D_c = \sum_{n=1}^{\infty} \frac{\mu_c^n e^{-\mu_c}}{n!} \,, \tag{2}$$

$$D_r = \sum_{n=1}^{\infty} \frac{\mu_r^{b+n} e^{-\mu_r}}{(b+n)!} \,, \tag{3}$$

where $\mu_c = R\tau_c$, $\mu_r = R(\tau_r - \tau_c)$, R is the rate, τ_c is the conversion time, τ_r is the readout time and b is the buffer factor [1]. The conversion time is fixed and module dependent. The readout time depends on the number of modules being read out and whether the readout is done via block reads or single module reads. When running the DAQ at low to moderate rate in buffered mode, b = 8, the buffer factor reduces the the readout contribution to the overall deadtime. The deadtime is then dominated by the conversion time. As the rate increases the probability of a full buffer also increases and the readout time begins to dominate the deadtime.

2.3.2 Improving Deadtime

Experiments typically aim for a maximum of 20% dead time. In the past, this translated into a maximum non-prescaled acceptable DAQ rate of $\sim$ 4 kHz. To increase the rate, a third Fastbus crate was added to the Left HRS. By distributing the module population throughout the three crates, the readout time of each was decreased, resulting in an improvement in the rate from 4 kHz to 6 kHz while maintaining comparable deadtime.

2.3.3 Deadtime Testing

The updated DAQ system was tested during commissioning for experiment E08-027. During the test the DAQ consisted of a Happex crate, three Fastbus crates and a Trigger Supervisor crate for scalers. The results in Table 3 highlight the 6 kHz improvement. Also using Eq. 2 and Eq. 3, we were able to model the deadtime. The model, plotted in Figure 13, compares favorably with the experimental data. As a comparison, the performance of two Fastbus crates is also presented for the Right HRS; the results are shown in Table 4 .

References

[1] R. Michaels, private communication.

Table 3: LHRS Deadtime. Included are the conversion and readout times used in the model in Figure 13. Note: The Happex and TS Scaler crates cannot be buffered; they operate on their own branch of the TS. The busy time listed for these components is the total busy time, and we have labeled it as the "readout" time.

Trigger Rate (kHz)	Deadtime (%)	Crate	τ_c (μs)	τ_r(μs)
14.2	49	TS/Happex		36
7.3	29	Fastbus	12	90
6.5	24			
5.3	20			
4.2	15			
3.2	12			

Table 4: RHRS Deadtime with two Fastbus crates, Happex crate and TS scaler crate.

Trigger Rate (kHz)	Deadtime (%)	Crate	τ_c (μs)	τ_r(μs)
19.5	60	TS/Happex		44
7.4	31	Fastbus	12	100
5.7	25			
4.4	20			

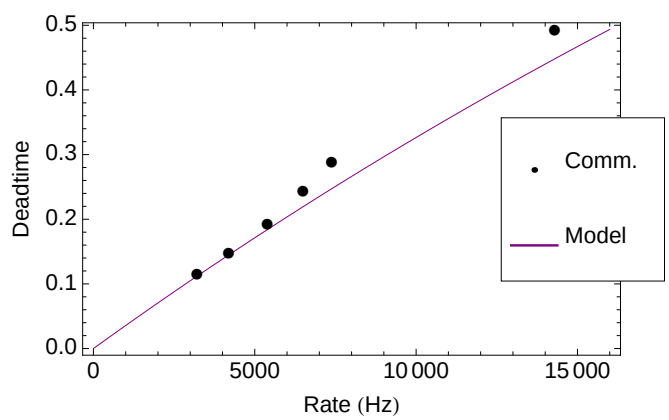

Figure 13: LHRS Deadtime with model prediction. The total deadtime is then a sum of the TS/Happex crate and slowest Fastbus crate.

3 Summaries of Experimental Activities

3.1 E97-110 - GDH

Progress report on E97-110: The GDH Sum Rule, the Spin Structure of ^{3}He and the Neutron using Nearly Real Photons

J.-P. Chen, A. Deur, F. Garibaldi spokespersons
and
the E97-110 Collaboration.

contributed by V. Sulkosky

3.1.1 The experiment

Experiment E97-110 was performed to provide a precise measurement of the ^{3}He spin structure functions at low Q^2 from 0.02 to 0.24 [GeV$/c$]^2. A longitudinally-polarized electron beam was scattered from a longitudinally or transversely (in-plane) polarized ^{3}He target. From these data, we have extracted the generalized Gerasimov-Drell-Hearn integral (GDH) and other moments of the neutron and ^{3}He spin structure functions at low Q^2. These data allow us to make a benchmark check of Chiral Perturbation Theory calculations in a region, where they are expected to be valid.

The experiment ran in two periods: April-May and July-August 2003. The first part of the experiment (low Q^2, April-May 2003) acquired data with a mis-wired septum magnet. The septum was repaired in June and the experiment was completed in July-August.

3.1.2 Analysis Progress

Work has concentrated on understanding the spectrometer acceptance for a beam energy of 3.775 GeV and spectrometer scattering angle of 9°. When the 9° data were first taken at this energy, we realized that the septum magnet indicated a saturation effect, i.e., the magnetic field is no longer linear with the septum current. The saturation curve was empirically determined using carbon foil data. The top panel of Fig. 14 shows the unpolarized ^{3}He cross section for this energy versus the invariant mass, W. For the 2.884 GeV/c momentum setting centered at 1500 MeV in W, the cross section is about 15% higher than the surrounding momentum settings. This is expected to be caused by having a mismatch between the septum field and the field settings for the standard HRS magnets.

A detailed cut study was performed using the Single Arm Monte-Carlo (SAMC) of A. Deur modified to include the septum magnet 9° transport functions and associated apertures. However, no optimal geometrical cuts were found to minimize the systematic shift for the 2.884 GeV/c momentum setting. For each of the momentum settings, the single carbon foil data were analyzed to extract the unpolarized carbon cross section and compared against an empirical model [2] weighted by the spectrometer acceptance. The elastic radiative tail was subtracted with the use of the program ROSETAIL.F [1], which was averaged over the solid angle acceptance. Fig. 15 shows the measured experimental cross section (top-left panel). The bottom-left panel shows the comparison between the data and the simulated cross section, and their ratio is shown in the bottom-right panel.

Overall there is about a 5-6% difference between the data and simulation for all settings with an additional $\sim$ 6% difference for the 2.884 GeV/c momentum setting. However for the problematic momentum setting, the experimental carbon cross section does not show any discontinuities unlike the ^{3}He data. This indicates that the jump in the cross section is primarily caused by the extended target acceptance. To test this hypothesis, a tight cut was placed on y_{tg} at $\pm$ 4 mm, and the discontinuity in the ^{3}He cross section vanished. This analysis has shown promise that the acceptance

for the ^{3}He data can be corrected as shown in the bottom panel of Fig. 14 of the ^{3}He normalized yield versus the energy transfer. We hope to finalize this analysis within the next couple of weeks.

Vivien Laine has completed the elastic asymmetry and cross section analysis for the 2.134 GeV, 6° data and has achieved good agreement with the expected values. He will continue his analysis for the other elastic settings for both 6° and 9° data sets.

Tim Holmstrom has completed work on smoothing the polarized cross-section differences for each of the incident beam energies. This is required prior to performing radiative corrections so that statistical fluctuations are not enhanced when the cross sections are unfolded.

Hai-jiang Lu, who is conducting the first period analysis (April-May 2003), was at JLab this past summer working on the spectrometer acceptance via the elastic carbon cross section data.

3.1.3 Remaining tasks.

Remaining tasks for the first paper are:

- Finalize the acceptance correction (V. Sulkosky)
- Complete the radiative corrections (T. Holmstrom and V. Sulkosky)
- Complete the polarimetry analysis (J. Singh. This task is nearly completed)
- Verify the polarimetry analysis and radiation lengths by analyzing the asymmetries and cross sections for the elastic kinematics (V. Laine).

3.1.4 Outlook.

Our goal is to publish the first paper in the first half of 2012, including only the data from the second period. This paper will concentrate on the generalized GDH sum and the neutron first moments. A draft of this paper has been internally circulated among the spokespersons. Work for subsequent papers includes the completion of the first period analysis, extraction of the higher moments for the neutron and both first and higher moments for ^{3}He.

References

[1] R. Altulmus and J. Wise, ROSETAIL.F, Fortran analysis code.

[2] P. Bosted *et al.*, FORTRAN Code for 2009 Fit, https://userweb.jlab.org/ bosted/fits.html.

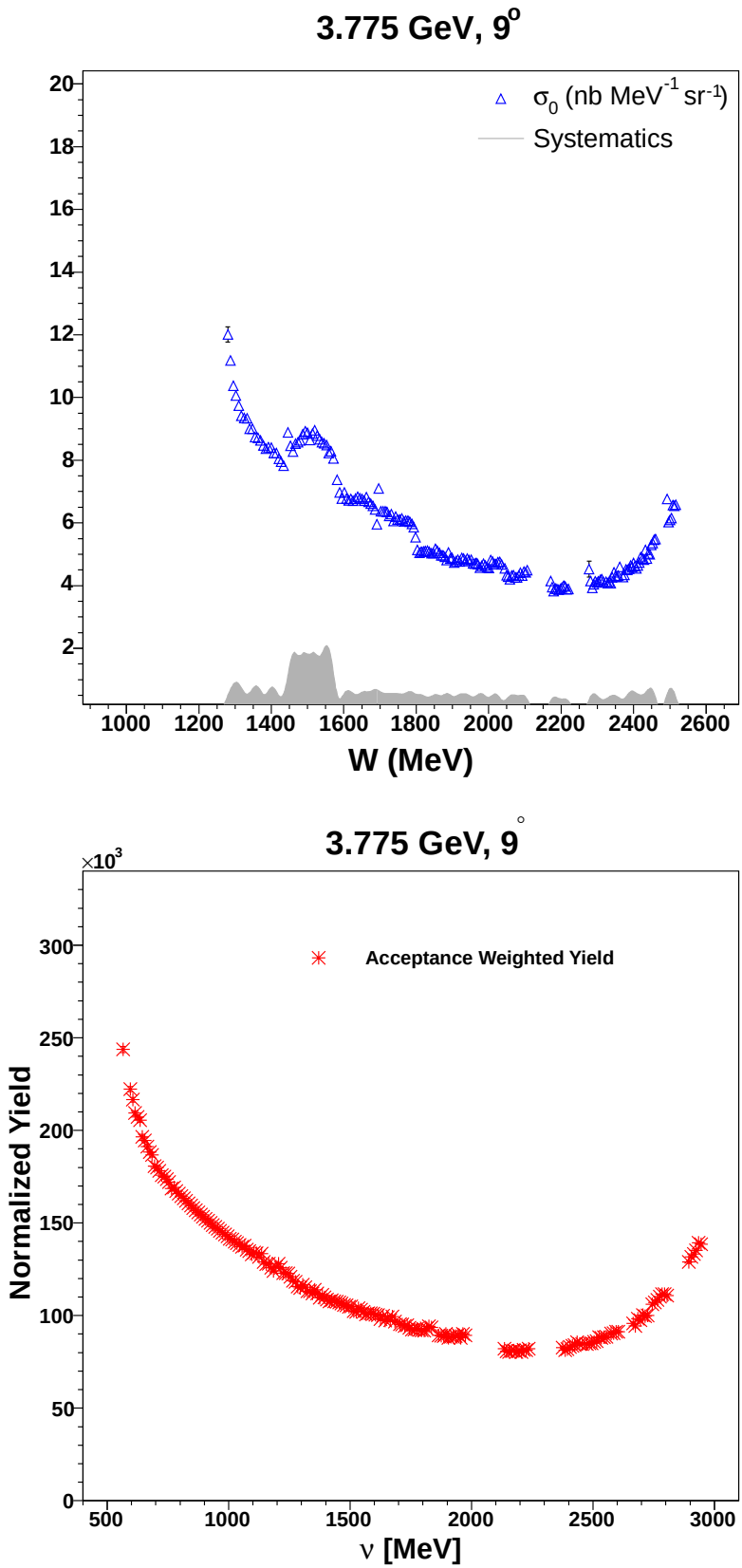

Figure 14: Preliminary unpolarized ^{3}He cross section (top) versus W. Acceptance corrected ^{3}He yield (bottom) versus ν after secondary acceptance corrections have been applied.

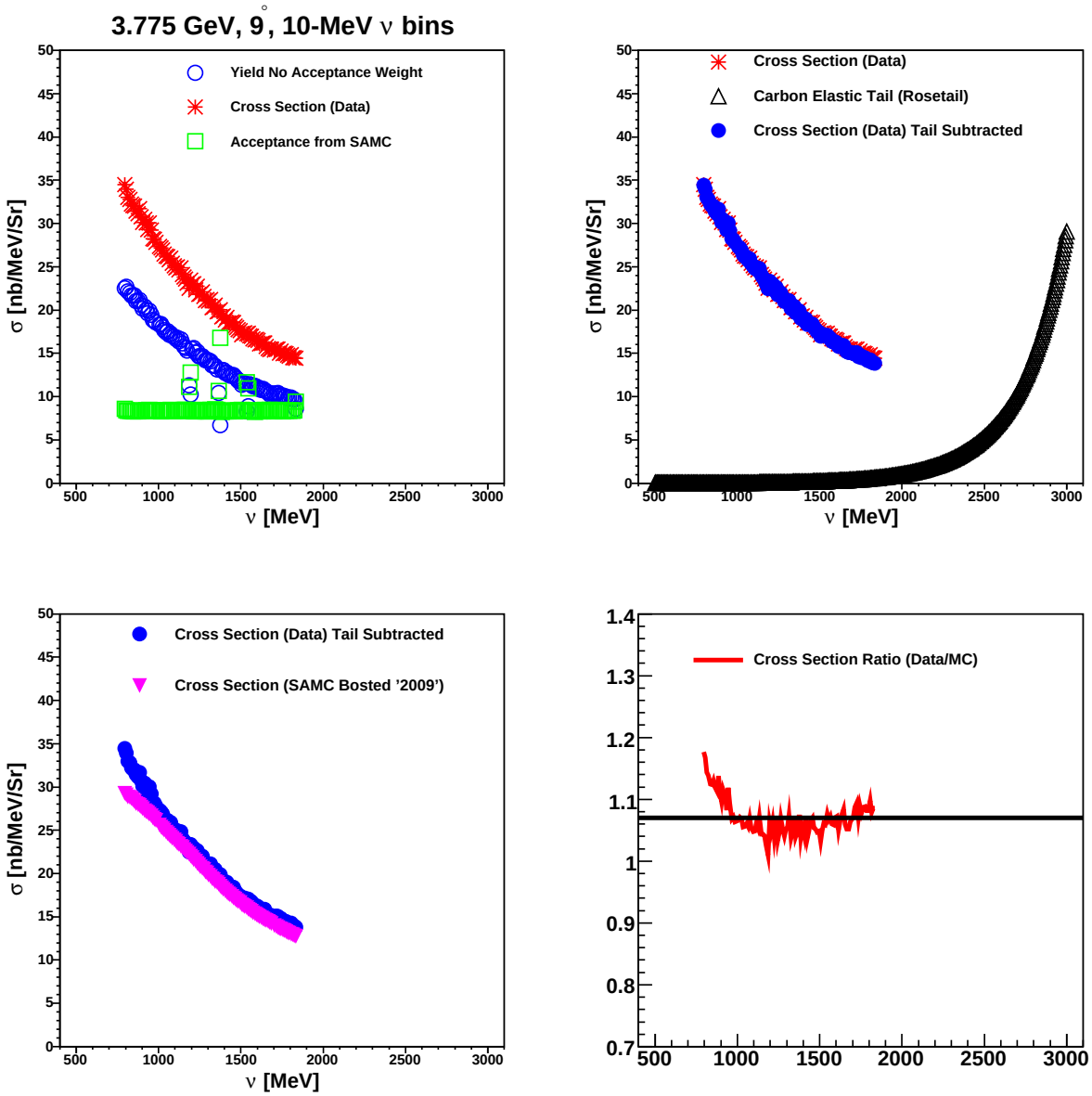

Figure 15: Carbon cross section comparison for 3.775 GeV, 9° data: cross section from data (Top-left panel), elastic tail subtraction (Top-right panel), data and simulation cross section comparison (Bottom-left panel) and the cross section ratio of data to simulation (Bottom-right panel).

3.2 E00-110, E07-007, E08-025 - DVCS

Contributed by E. Fuchey and J. Roche.

E00-110: Deeply Virtual Compton Scattering At 6 GeV. Spokespersons: P. Bertin, C. Hyde, R. Ransome and F. Sabatié.
E07-007: Complete Separation of Deeply Virtual Photon and π^0 Electroproduction Observables of Unpolarized Protons. Spokespersons: C. Hyde, C. Muñoz-Camacho, A. Camsonne, J. Roche.
E08-025: Measurement of the Deeply Virtual Compton Scattering cross-section off the neutron. Spokespersons: C. Hyde, M. Mazouz, A. Camsonne.

The Hall A DVCS program provides data relevant to the *"3-D structure of the nucleon"* program at JLab by measuring precise absolute cross-sections in the Deep Exclusive domain. A short update is given on the analysis of phase two of the program which ran during the Fall of 2010. The last section describes the latest publication from experiment E00-110 (phase one of the program) about deeply virtual pion production.

3.2.1 Update on the analysis of experiments E07-007 (Hydrogen) and E08-025 (Deuterium)

Deeply Virtual Compton Scattering off the nucleon ($\gamma^* N \to \gamma N$) is the simplest process which is sensitive to the Generalized Parton Distributions (GPDs). In the Bjorken limit, similar to DIS, the factorization theorem separates the reaction amplitude into the convolution of a known perturbative ($\gamma^* q \to \gamma q$) kernel with unknown soft matrix elements describing the nucleon structure (the GPDs). Experimentally, the DVCS process is measured coherently with the Bethe-Heitler process (BH), where the real photon is emitted by either the incoming or scattered electron. An important result of the previous generation of DVCS experiments in Hall A, was to show that the contribution from the calculable BH process accounts for only 50% of the total cross-section in certain kinematics. The goal of experiments E07-007 and E08-025 is to provide a complete separation of the two components to the unpolarized cross section: the pure DVCS contribution and the real part of the interference between the BH and the DVCS amplitudes. This is achieved using a Rosenbluth-like separation: cross-sections at a given Q^2, x_B and t are measured at two different beam energies. Experiment E07-007 off the hydrogen target will provide this separation at three different values of Q^2 (1.5, 1.75 and 2.0 GeV^2), while E08-025 will provide the separation at one Q^2 (1.75 GeV^2).

Both experiments took data in the Fall of 2010. After a longer than expected commissioning period and issues with the trigger, the DVCS setup was used as originally proposed and over 80% of the proposed data were collected. The proposals assumed a 6 GeV beam while the maximum that could be delivered to accommodate the low energy requirement of the QWeak experiment in Hall C was only 5.5 GeV. This resulted in a reduced lever arm in Q^2 (1.5-2.0 GeV^2 instead of 1.5-2.3), data being taken closer to the nucleon resonance region for the lowest Q^2 setting ($W^2 = 3.55$ instead of 3.78 GeV^2) and overall larger background noise. The online analysis showed that the data quality are good. The scattered electron is detected in the left HRS, while the radiated real photon is detected in the dedicated DVCS PbF_2 calorimeter. The recoil proton is identified by missing mass. The DVCS calorimeter was calibrated *via* elastic ep scattering three times during the data taking, and the analysis of these data reproduced the expected energy resolution for the calorimeter (σ/E 3.5% at E=3.05 GeV). During the DVCS data taking, the calibration constants of each PbF_2 block is tracked using two-photon events in the calorimeter, for these events the invariant mass of the π^0 is reconstructed, the online analysis showed that the mass of the π^0 was correctly reconstructed. Finally, online data showed that the invariant mass squared reconstructed from events of type $ep \to e\gamma X$ peaks at the nucleon mass squared.

The offline analysis of the data so far has been focused on the beam instrumentation data and on the LHRS. The polarimetry data have been analyzed and the BCM calibrations were performed (taking into account an initial period during which the BCM were not thermally regulated and two sudden jumps in the gains of the downstream BCM). An extensive effort went into the analysis of the single arm HRS data taken in parallel to the DVCS data, these allow to cross-check our understanding of the spectrometer acceptance and the luminosity of the experiment.

Preliminary results show that the DIS absolute cross-section is reproduced at better than 3% in most kinematics, with only one kinematic being problematic with experimental cross-sections being measured at 10% above the expected ones. Other preliminary analysis focused on the fine tuning of the calorimeter calibration constants, of the coincidence time between the LHRS and the calorimeter, of the parameters of the calorimeter wave form analysis.

3.2.2 Latest physics result from experiment E00-110

This section reports on the latest publication [1] from the phase one of the DVCS program in Hall A (data taken in the Fall of 2004 during experiment E00-110). This publication presents the analysis of the triple coincidence events $H(e,e'\gamma\gamma)X$ in order to extract the cross section of exclusive neutral pion electro-production in the Deep Inelastic Scattering regime ($Q^2 > 1\,\mathrm{GeV}^2$, $W > 2\,\mathrm{GeV}$). These results were accepted for publication by Physical Review C in February of 2011. They constitute the first set of exclusive π^0 electro-production cross sections in the deep inelastic scattering regime. Previously, only exclusive charged pion electro-production production were available from Hall C [6], and neutral beam spin asymmetry was available from Hall B [7]. Exclusive π^0 electroproduction cross sections

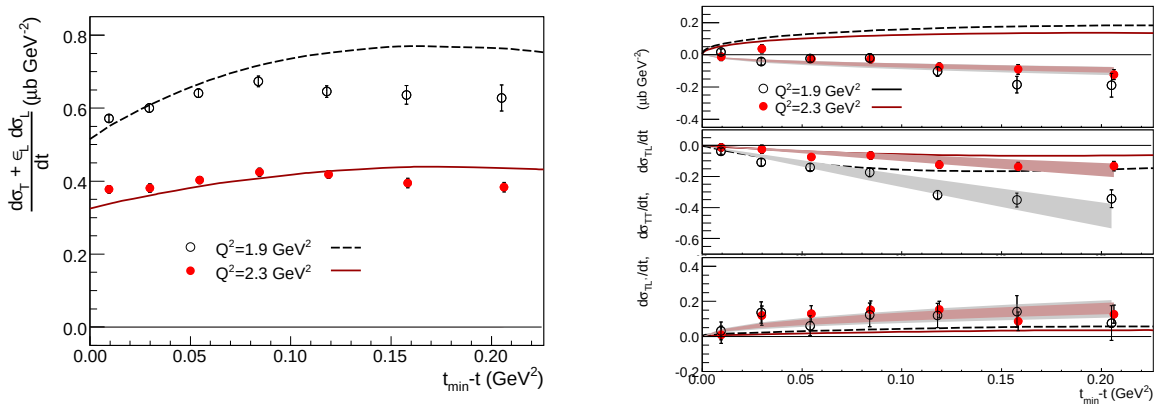

Figure 16: Left: Total π^0 cross section ($\sigma_T + \varepsilon_l \sigma_L$) differential in t as a function of $t_{min} - t$ at $Q^2 = 1.9\,\mathrm{GeV}^2$ (black hollow circles) and $Q^2 = 2.3\,\mathrm{GeV}^2$ (red solid circles). Right: Harmonic components of the π^0 cross section ($\sigma_{TL}, \sigma_{TT}, \sigma_{TL'}$, top to bottom) differential in t as a function of $t_{min} - t$ at $Q^2 = 1.9\,\mathrm{GeV}^2$ (black hollow circles) and $Q^2 = 2.3\,\mathrm{GeV}^2$ (red solid circles). The bands are results from the fits of those components with their leading order in θ^{CM}, the angle of the pion w.r.t the virtual photon. The curves represent the model from J.-M. Laget [2], for $Q^2 = 1.9\,\mathrm{GeV}^2$ (dashed black curve) and for $Q^2 = 2.3\,\mathrm{GeV}^2$ (red solid curve).

have been extracted at two different values of Q^2 (1.9 and 2.3 GeV^2) at fixed $x_{Bj} = 0.36$, and at two different values of W (2.0 and 2.3 GeV) at fixed $Q^2 = 2.1\,\mathrm{GeV}^2$. Moreover, harmonic decompositions of the cross section were performed. Figure 16 shows the resulting total cross section (left panel) and the components of the harmonic decomposition of the cross section (right panel), as functions of $t_{min} - t$, for $x_{Bj} = 0.36$. In the paper, the total cross section and its Q^2-dependence have been compared to several models available for the description of π^0 electro-production. Those models include a Regge-inspired model from J.-M. Laget [2], the GPD formalism applied to pseudo-scalar meson electro-production [4, 3], and the model of Kaskulov, Gallmeister and Mosel, which uses quark fragmentation functions for a successful description of the exclusive charged pion electro-production transverse cross section [5]. The model from J.-M. Laget is plotted along our data on figure 16. It successfully describes the total cross section and the helicity-dependent component of the cross section. However, it fails to describe the other components of the harmonic decomposition of the cross section. The main result of the paper is that the Q^2-dependence of the total cross section is roughly in $1/Q^5$. On the one hand, such a Q^2-dependence clearly disagrees with the predictions from the GPD model. On the other hand, it is consistent with the Q^2-dependence of the transverse π^+ cross section extracted by Hall C. This suggests dominance of the transverse cross section over the longitudinal cross section in these kinematics. Since the publication of these results, a new publication of M. Kaskulov [8] presents a model of neutral pion production from the real photon point to the DIS regime. This model is in good agreement with our data, including the separated cross sections.

References

[1] E. Fuchey *et al.*, Phys. Rev. **C83**, 025201 (2011).

[2] J.-M. Laget, Phys. Lett. **B695**, 199 (2011).

[3] M. Vanderhaeghen, P.A.M. Guichon, and M. Guidal, Phys. Rev. **D60**, 094017 (1999).

[4] K. Goeke, M.V. Polyakov, and M. Vanderhaeghen, Prog. Part. Nucl. Phys. **47**, 401 (2001).

[5] M. Kaskulov, K. Gallmeister, and U. Mosel, Phys. Rev. **D78**, 114022 (2008).

[6] T. Horn *et al.*, Phys. Rev. **C78**, 058201 (2008).

[7] R. De Masi *et al.*, Phys. Rev. **C77**, 042201 (2008).

[8] M. Kaskulov, arXiv:1105.1993v1[nucl-th] (2011).

[9] S.V. Goloskokov, and P. Kroll, Eur. Phys. J. **A47**, 112 (2011).

3.3 E04-007 - π^0

Precision Measurements of Electroproduction of π^0 near Threshold: A Test of Chiral QCD Dynamics

contributed by Richard Lindgren and Cole Smith
for
J.R.M. Annand, D.W. Higinbotham, R. Lindgren, B. Moffit, B. Norum, V. Nelyubin, spokespersons,
M. Shabestari and K. Chirapatimol, students
and
The Hall-A Collaboration

3.3.1 Introduction

The experiment is designed to measure the electroproduction reaction $p(e,e'p)\pi^0$ of neutral pions off the proton at the lowest possible invariant mass W. Results from previous electroproduction measurements at Mainz with four-momentum transfers of Q^2 = 0.10 GeV/c^2 [1] and Q^2 = 0.05 GeV/c^2 [2] were in disagreement with the Q^2 dependence predicted by Heavy Baryon Chiral perturbation theory (HBChPT) and also inconsistent with the predictions of the MAID model [3]. If the Mainz discrepancies remain unresolved, they will constitute a serious threat to the viability of Chiral Dynamics as a useful theory of low energy pion production. Our experiment has measured absolute cross sections as precisely as possible from threshold to ΔW = 30 MeV above threshold at four-momentum transfers in the range from Q^2 = 0.050 GeV/c^2 to Q^2 = 0.150 GeV/c^2 in small steps of ΔQ^2 = 0.01 GeV/c^2. This will cover and extend the Mainz kinematic range allowing a more sensitive test of chiral corrections to Low Energy Theorems for the S and P wave pion multipoles. In addition, the beam asymmetry will be measured, which can be used to test predictions for the imaginary components of the of S wave E_{0+} and L_{0+} pion multipoles, which are sensitive to unitary corrections above the $n\pi^+$ threshold. Mainz recently repeated the electroproduction measurements and now report [4] that the new results are more consistent with HBChPT predictions, but are in disagreement with their own previous measurements [2]. In view of the importance of knowing whether or not HBChPT is valid in this domain, it is imperative that an independent set of measurements be reported.

3.3.2 Experimental Results

The experiment was performed using the Hall A left High Resolution Spectrometer (LHRS) to detect the electron and the large acceptance BigBite spectrometer instrumented with MWDC followed by $E-\Delta E$ scintillation paddles to detect and identify the proton. The structure functions $\sigma_T+\varepsilon_L\sigma_L$, σ_{TL}, and σ_{TT} were extracted using the measured ϕ dependence of the cross section. Figure 1 shows our current results for Q^2=0.105 GeV^2 and ΔW = 8.5 MeV, which already extends the kinematic range previously explored in threshold electroproduction. Figure 2 shows our results for the beam asymmetry $A_{LT'}$, which is proportional to the sin ϕ^* dependence of the beam helicity weighted cross section.

We have made a number of improvements in our simulation of the BigBite spectrometer including a radiated physics event generator using the Dubna-Mainz-Taipei (DMT) dynamical model [5, 6] to improve simulation of energy loss and straggling, and including a more realistic magnetic field map for the dipole magnet calculated by V. Nelyubin to study fringe field effects. We have developed empirical corrections to improve the missing mass resolution and compensate for energy loss and low momentum transverse focusing of protons. Also we have studied the detection efficiency for low-momentum protons and developed procedures for recovering protons which fall below the ΔE counter hardware thresholds. We are investigating improvements in the LHRS simulation to better understand our W resolution at threshold and the effects of target straggling and bin migration due to resolution smearing. We are also working to improve the VDC calibration and energy loss corrections in LHRS to achieve the best performance at threshold.

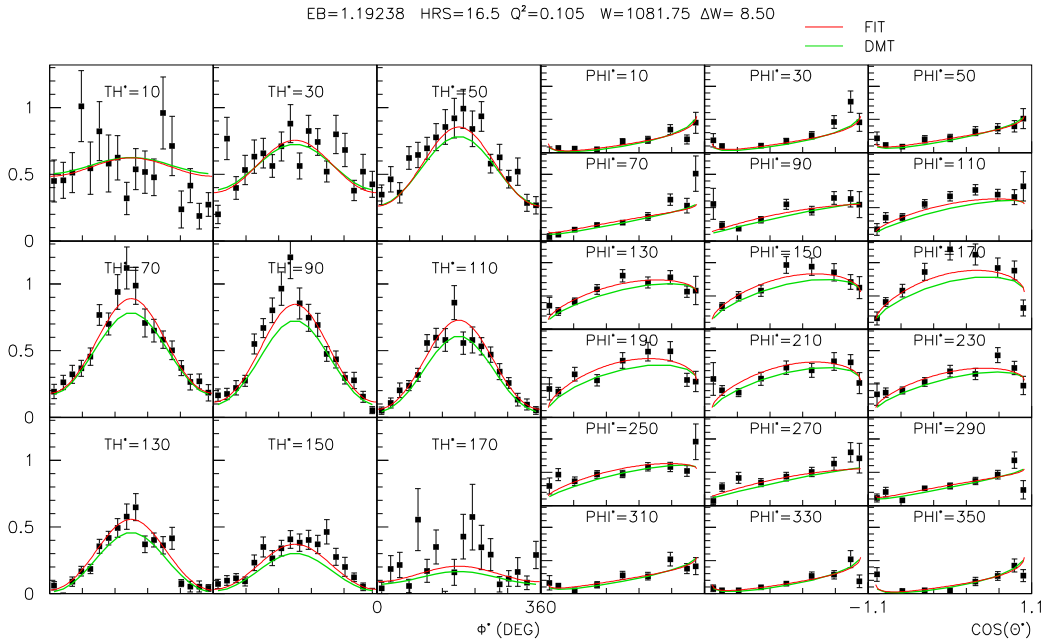

Figure 17: Angular distributions of $p\pi^0$ C.M. cross sections.

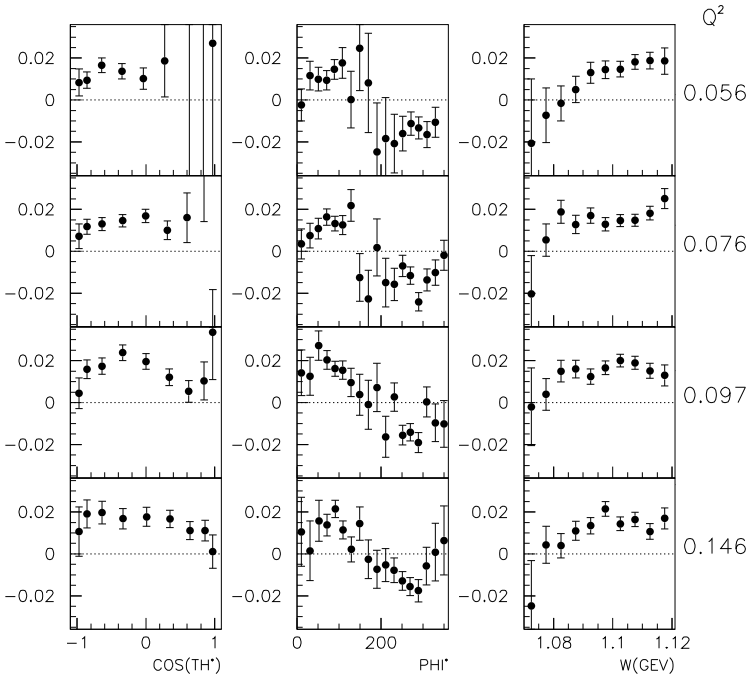

Figure 18: Beam asymmetry measurements

References

[1] M.O. Distler et al., Phys. Rev. Lett. **80**, 2294 (1988).

[2] H. Merkel et al., Phys. Rev. Lett. **88**, 12301 (2002).

[3] D. Drechsel, S.S. Kamalov and L. Tiator, Eur. Phys. J. **A 34**, 69 (2007).

[4] H. Merkel et al., ”Proceedings of the 6th International Workshop on Chiral Dynamics July 6-10 2009, Bern, Switzerland”.

[5] S.S. Kamalov and S.N. Yang, Phys. Rev. Lett. **83**, 4494 (1999).

[6] http://wwwkph.kph-uni-mainz.de/MAID//dmt/dmt2001.html.

3.4 E05-009 - HAPPEX-III

The HAPPEX Collaboration

Contributed by Robert Michaels

HAPPEX-III ran in the Fall of 2009. It is the third in the series of Hall A experiments to measure the strangeness content of the proton [1]. The data have been analyzed, presented at conferences, and a physics letter is on the archive [2]. The experiment measures the parity violating asymmetry in elastic scattering from a proton $A_{PV} = (\sigma_R - \sigma_L)/(\sigma_R + \sigma_L)$ at an beam energy $E_b = 3.48$ GeV and four-momentum transfer squared $Q^2 = 0.624$ GeV^2. The measured asymmetry was $A_{PV} = -23.80 \pm 0.78(\text{stat}) \pm 0.36(\text{syst})$ ppm and was consistent with the Standard Model prediction and with zero contribution of strange quarks to the electromagnetic structure of the proton.

Measurements of the contribution of strange quarks to nucleon structure provide a unique window on the quark-antiquark sea and make an important impact on our understanding of the low-energy QCD structure of nucleons. Parity violating electron scattering is a practical method to measure the strange vector matrix elements [3, 4, 5]. Purely electromagnetic scattering at a given kinematics can measure only two linear combinations of the Sachs form factors:

$$G^{\gamma p}_{E,M} = \frac{2}{3} G^u_{E,M} - \frac{1}{3} G^d_{E,M} - \frac{1}{3} G^s_{E,M} \tag{4}$$

$$G^{\gamma n}_{E,M} = \frac{2}{3} G^d_{E,M} - \frac{1}{3} G^u_{E,M} - \frac{1}{3} G^s_{E,M} \tag{5}$$

where $G^f_{E,M}$ is the electric (E) or magnetic (M) form factor for quark flavor f in the proton. Here it is assumed that the quark flavors u, d, and s contribute. Charge symmetry between proton p and neutron n is also assumed, so that for the quark form factors

$$G^u_p = G^d_n \; ; \quad G^d_p = G^u_n \; ; \quad G^s_p = G^s_n \tag{6}$$

where now the subscripts p and n are for proton and neutron.

Additional information is needed to determine whether or not there is a contribution from the strangeness form factors $G^s_{E,M}$. This is provided by parity violation in the scattering from protons, measuring a new pair of linear combinations

$$\begin{aligned} G^{Zp}_{E,M} \; = \; & \left(\frac{1}{4} - \frac{2}{3} \sin^2 \theta_W \right) G^u_{E,M} \; + \\ & \left(-\frac{1}{4} + \frac{1}{3} \sin^2 \theta_W \right) \times \left[G^d_{E,M} + G^s_{E,M} \right] \end{aligned} \tag{7}$$

where Z stands for the Z^0 boson of the neutral weak interaction. Thus by measuring these neutral weak form factors, in conjunction with the electromagnetic form factors, we are able to extract the strange quark contribution.

For more details about the HAPPEX-III results and their implications, the reader is referred to the archive paper [2]. At the present time, there are no new proposals at JLab to measure strangeness using parity violation. As summarized in the recently published chapter on strangeness in the JLab 10-Year Highlights book [6] the strangeness contributions are consistent with zero, i.e. small compared to the electromagnetic form factors, as well as consistent with modern QCD-based calculations. It might be impossible to push these experiments to a higher accuracy, owing to other limits on the precision such as radiative corrections and charge symmetry violation.

References

[1] K.A. Aniol *et.al.*, Phys. Lett. B **509** (2001) 211; K.A. Aniol *et.al.*, Phys. Rev. C**69** (2004) 065501; K.A. Aniol *et.al.*, Phys. Rev. Lett. **96** (2006) 022003; K.A. Aniol *et.al.*, Phys. Lett. B**635** (2006) 275; A. Acha *et.al.*, Phys. Rev. Lett. **98** (2007) 032301.

[2] Z. Ahmed *et.al.* arXiv:1107.0913 (2011), submitted to PRL.

[3] R. D. McKeown, Phys. Lett. B **219** (1989) 140.

[4] E. J. Beise and R. D. McKeown, Comments Nucl. Part. Phys. **20** (1991) 105.

[5] D. H. Beck, Phys. Rev. D **39** (1989) 3248.

[6] K. Paschke, A. Thomas, R. Michaels, and D. Armstrong, arXiv 1110.3426 [nucl-ex] (2011) published in the book D. Higinbotham, W. Melnitchouk, and A. Thomas, New Insights into the Structure of Matter, J. Phys. Conf. Ser. 299 (2011) 011002.

3.5 E05-015 - A_y in ^{3}He(e,e')

Measurement of the Target Single-Spin Asymmetry in Quasi-Elastic $^3\text{He}^\uparrow(e,e')$

T. Averett, J.-P. Chen and X. Jiang (spokespersons)
and the Hall A Collaboration.

contributed by Y.-W. Zhang

Experiment overview

In the past years, the structure of nucleons and nuclei was studied by measuring form factors using the Born approximation, which assumes one photon exchange, with multiple photon exchange neglected. As new high precision data becomes available, the contribution of two-photon exchange can no longer be ignored, as demonstrated by the proton electric form factor data [1, 2, 3].

JLab experiment E05-015 measured the target single-spin asymmetry, A_y, for the neutron using the inclusive quasi-elastic $^3\text{He}^\uparrow(e,e')$ reaction with a vertically polarized ^{3}He target. In the one-photon exchange approximation, A_y is expected to be zero due to time-reversal invariance in elastic scattering. In recent calculations, A_y is expected to be non-zero from the interference between the one-photon exchange amplitude and the imaginary part of the two-photon exchange amplitude [4]. A precise measurement of A_y will provide a new experimental constraint on GPD model input [5].

This experiment ran from April 24 to May 12 in 2009. Data were collected in three different kinematic regions, listed in the following table:

E_0(GeV)	E'(GeV)	θ_{spec} (Deg)	Q^2 (GeV^2)	|q| (GeV)	θ_q (Deg)
1.25	1.22	17	0.13	0.359	71
2.43	2.18	17	0.46	0.681	62
3.61	3.09	17	0.98	0.988	54

Table 5: Ay experiment (E05-015) kinematic settings.

Data analysis

In this experiment, the Hall A left and right HRS's were both used to collect the data. All the important scalers were sent to both arms for a cross-check, which means there are two copies of each scaler. Left HRS and right HRS were synchronized so that they have the same run time for each production run pair. Then, in principle, the reading of scalers from the left-arm should be as same as that from the right-arm.

After the optics calibration (by Ge Jin) and detector calibration, the raw experimental data were processed with standard Hall A analysis software and saved as root files. Each event is reconstructed, and the scalers are decoded for later analysis.

It was easy to identify good electrons using gas Cerenkov counters and lead-glass calorimeters, since the pion background is very low in this quasi-elastic scattering experiment. However, we need to ensure the scalers do not cause a large false asymmetry. For this purpose, we checked the un-gated scalers from both LHRS and RHRS. Any data with scaler asymmetries between the left-arm and right-arm $>10^{-4}$ were discarded.

The experiment used the standard Hall-A polarized ^{3}He target with a vertical holding field. To extract the target

polarization, several measurements have been conducted to calibrate different target system components, including EPR, NMR and density measurements.

Preliminary results

The polarization in the target pumping chamber during the experiment is shown in the Fig. 19.

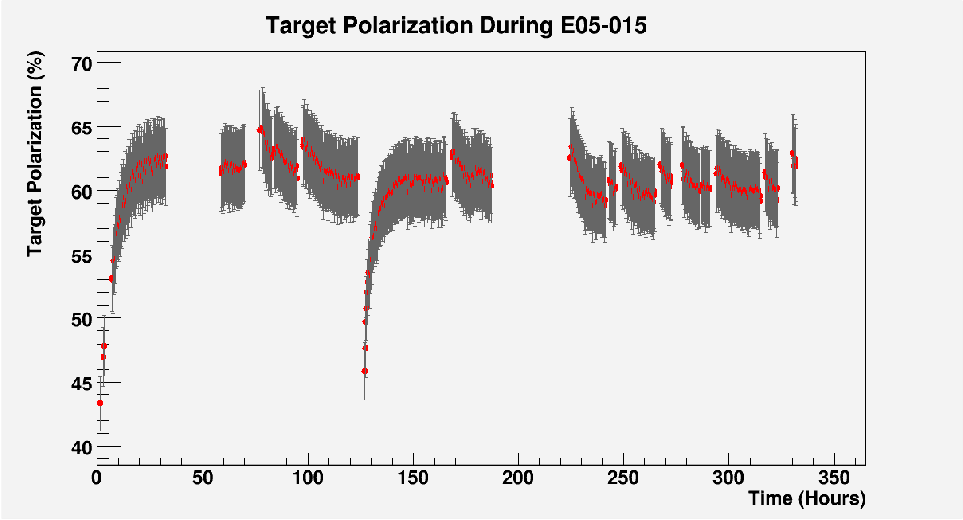

Figure 19: ^{3}He target performance during the A_y experiment

The preliminary target single-spin asymmetry at $Q^2 = 0.98$ GeV^2 is shown in Fig. 20. As mentioned in the previous section, the scattered electrons were detected on both sides of the beam line, so the target single-spin asymmetries calculated from left-arm data and right-arm data should have opposite signs, due to the fact that corresponding to a given target spin direction, say S_T pointing up, scattering to the beam left side, $(\vec{e} \times \vec{e'}) \cdot S_T > 0$, on the other hand, scattering to the beam right side, $(\vec{e} \times \vec{e'}) \cdot S_T < 0$.

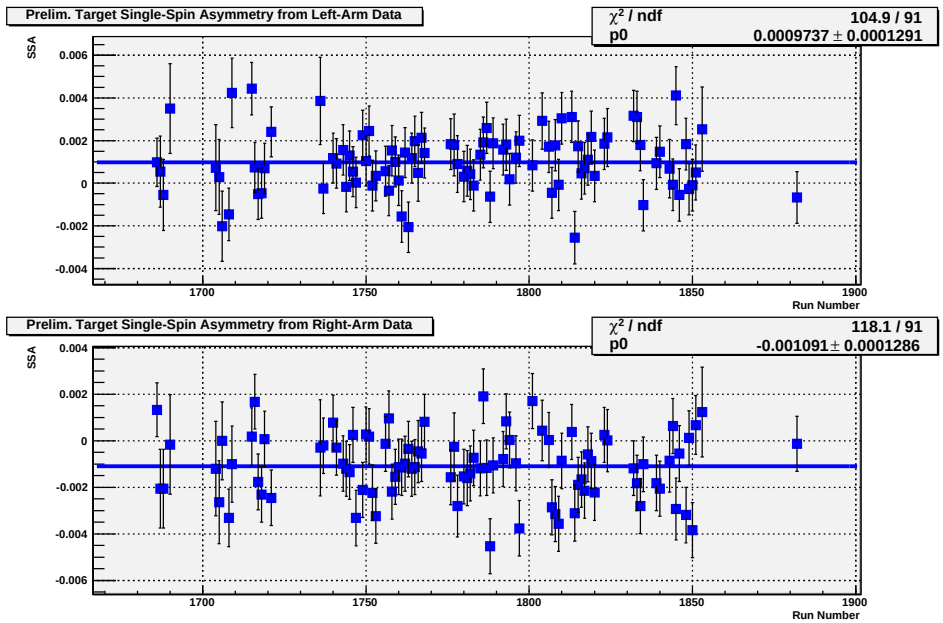

Figure 20: The preliminary ^{3}He target single-spin asymmetry from left-arm data(top plot) and right-arm data (bottom plot) at Q^2= 0.98 GeV^2. The solid lines indicate a constant fit to the target single-spin asymmetry for each run.

Remaining tasks

Estimation of systematic uncertainties for left-arm data at $Q^2 = 0.98$ GeV^2 is ongoing, but is expected to be completed soon. After this, we will apply the same analysis procedure to the right-arm data and to the other kinematic settings, $Q^2 = 0.46$ GeV^2 and $Q^2 = 0.13$ GeV^2. We expect to release the final results and submit for publication within 6 months.

References

[1] L. Andivahis *et al., Physical Review D, 50(9):5491-5517 (1994)*

[2] O. Gayou *et al., Physical Review Letters, 88(9), (2002)*

[3] M. Jones *et al., physical Review Letters, 84(7):1398-1402, (2002)*

[4] A. Afanasev *et al., hep-ph/0208260*

[5] Y.C. Chen *et al., physical Review Letters, 93, 122301 (2004)*

3.6 E05-102 - A_x, A_z in ^{3}He(e,e'd)

We have completed the optics calibration of the BigBite spectrometer, which was used to detect hadrons in the E05-102 experiment. We have adopted a matrix formalism approach based on the singular value decomposition (SVD) technique that allowed for a precise and reliable calibration of the spectrometer (see Fig. 21). For 0.55 GeV/c protons, we have established the vertex resolution of 1.2 cm, angular resolutions of 7 mrad and 16 mrad (in-plane and out-of-plane, respectively), and a relative momentum resolution of 1.6 %.

In order to obtain the optics matrix applicable to all types of particles, energy losses for particle transport through the target enclosure and materials within the BigBite spectrometer were studied carefully. The energy losses were estimated by the Bethe-Bloch formula, but since the losses were significant, the formula had to be integrated over the complete particle track for each particle type and each initial momentum. The two largest contributions to the total momentum loss come from the target cell walls and from the air inside BigBite. The resulting corrections that were taken into account are shown in Fig. 22 (top-left).

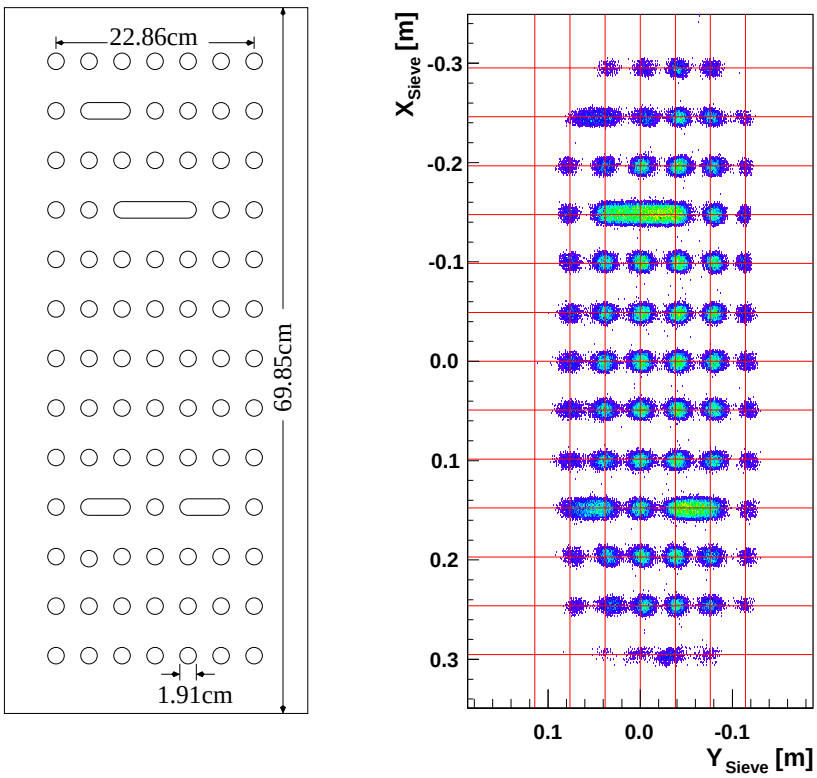

Figure 21: [Left] Schematics of the BigBite sieve-slit collimator. [Right] Reconstructed sieve pattern. The leftmost holes are missing due to geometrical obstacles between the target and BigBite.

Understanding the energy losses also enabled us to complete the ADC calibration of the BigBite scintillation detectors (E and dE). The readout (deposited energy in terms of the ADC channels) from these detectors was already properly gain matched and corrected for any offsets. However, a precise knowledge of the energy losses in the scintillators and surrounding materials was required for absolute calibration in terms of the deposited energy (in units of MeV). See Fig. 22 (Bottom).

The TDC calibration of the scintillation detectors was also performed. Offsets between the time information from the left and right PMTs were corrected for each scintillation bar. In addition, an energy scale for the TDC threshold, which sets the limits for particle detection, was determined (the threshold is set in terms of millivolts in the discriminator modules).

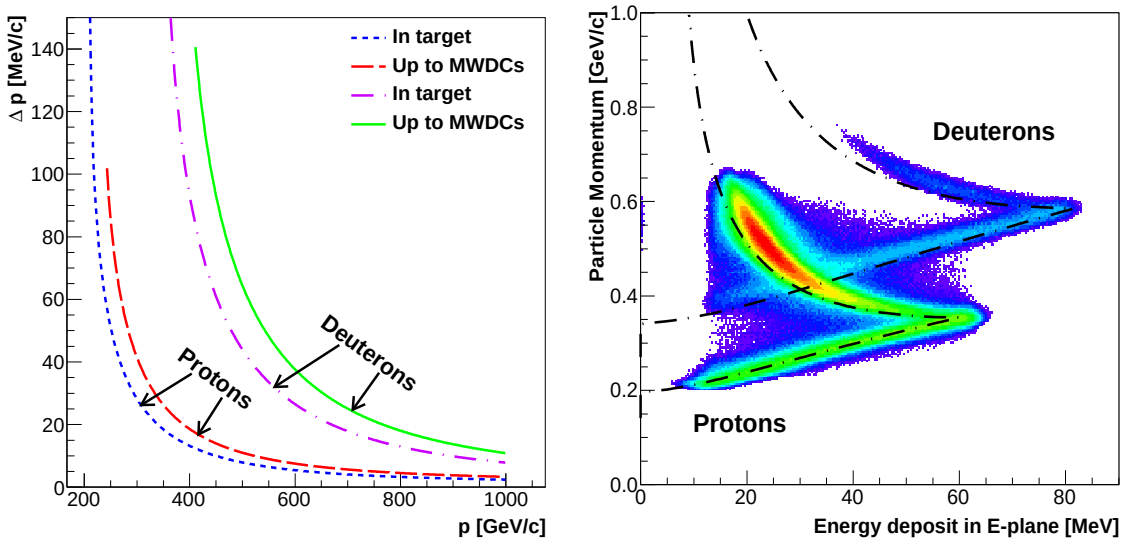

Figure 22: [Top-Left] Momentum losses of protons and deuterons inside the target and the total momentum losses up to the MWDCs. [Top-Right] Quality of reconstructed momentum for elastic protons and deuterons. If energy losses are not taken into account, two peaks are visible (center and right histograms summed to the full curve). With proper inclusion of energy losses both peaks merge into one (left histogram), resulting in better momentum resolution. [Bottom] Energy losses in the E-plane as a function of particle momentum for ^{3}He data. The deuterons can be clearly distinguished from the protons. The measurements agree well with the expectation (dot-dashed line).

A detailed analysis of BigBite scalers was also performed, and some problems in our scaler readout have been discovered. There are two scalers banks: `bbite` and `evbbite`. The first one is written into the data stream as a special event (type 140). The second one is recorded for each accepted event. When results from both types of scalers were compared, we realized that both are missing some information. The `bbite` scaler bank does not contain information about TDC hits for some of the scintillation bars. On the other hand, the `evbbite` bank is missing one of the gated scalers with information on trigger rates for one combination of beam-target spin states. Fortunately both banks are missing different parts of information. This way all information has been restored by combining information from both banks.

In addition to the calibration of the BigBite spectrometer, the calibration of the beam-charge monitors (BCM) was performed. Using dedicated data sets, calibration constants and offsets were determined that are required to transform the raw BCM readout to the collected physical charge (in coulombs).

The main physics goal of the experiment E05-102 is to measure double spin asymmetries in the quasi-elastic $^3\vec{\mathrm{He}}\,(\vec{\mathrm{e}},\mathrm{e}'\mathrm{p})$ and $^3\vec{\mathrm{He}}\,(\vec{\mathrm{e}},\mathrm{e}'\mathrm{d})$ processes as a function of momentum of the undetected particles (missing momentum). Now that the calibration of BigBite has been completed, we have extracted the asymmetries for the proton channel. The preliminary results are shown in Fig. 23.

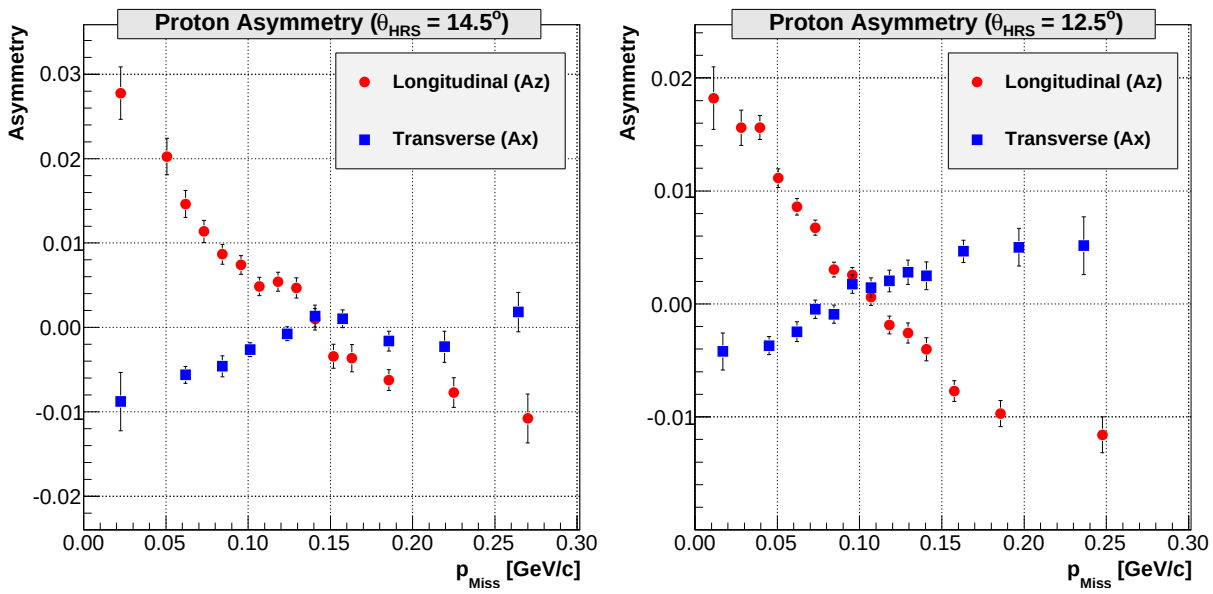

Figure 23: Double spin asymmetries in the quasi-elastic $^3\vec{\mathrm{He}}(\vec{\mathrm{e}},\mathrm{e}'\mathrm{p})$ process for two different target settings. In the longitudinal configuration the target spin was oriented in the direction of the beam. In the transverse configuration the target spin was pointing to the left of the beam direction. The asymmetries were measured at two different momentum transfers: [Left] $Q^2 = 0.35\,\mathrm{GeV}^2/c^2$, [Right] $Q^2 = 0.25\,\mathrm{GeV}^2/c^2$.

3.7 E06-002 - PREX

The PREX Collaboration

The Lead Radius Experiment (PREX) ran in the Spring of 2010. The first results were reported at the Spring 2011 APS meeting and, as this report is being written, a physics letter is on the verge of being submitted for publication. Many details of the experiment were described in the 2010 Hall A Annual Report. A follow-up measurement, PREX-II, was proposed and accepted by PAC38 [1]. A new proposal on ^{48}Ca is being developed for PAC39.

The experiment measures the parity violating asymmetry in elastic scattering $A_{PV} = (\sigma_R - \sigma_L)/(\sigma_R + \sigma_L)$ from the ^{208}Pb nucleus. This asymmetry is sensitive to the neutron radius R_n because the weak charge of the neutron is much larger than that of the proton [2]. In PWIA, the relationship between the asymmetry and the neutron form factor is given by equation (8)

$$A_{PV} = \frac{G_F Q^2}{4\pi\alpha\sqrt{2}} \left[1 - 4\sin^2\theta_W - \frac{F_n(Q^2)}{F_p(Q^2)} \right] \tag{8}$$

where G_F is the Fermi constant, $\alpha = \frac{1}{137}$ is the fine structure constant, θ_W is the Weinberg angle, and $F_n(Q^2)$ and $F_p(Q^2)$ are the neutron and proton form factor of the nucleus. Coulomb distortions are the largest correction and have been calculated by Horowitz[3].

The size of a heavy nucleus, or equivalently, the central density of nuclear matter ρ_0, is a fundamental property central to nuclear physics. Important applications include: 1) Neutron-rich matter in Astrophysics; 2) Understanding nuclear structure; 3) Structure of neutron rich radioactive beams; 4) Atomic parity-non-conservation (PNC) experiments.

In our forthcoming publication, we report a parity-violating asymmetry $A_{PV} = 0.656 \pm 0.060\ (\text{stat}) \pm 0.013\ (\text{syst})$ ppm. This corresponds to a difference between the radii of the neutron and proton distributions $R_n - R_p = 0.33^{+0.16}_{-0.18}$ fm. This provides the first electroweak observation of the neutron skin which is expected in a heavy, neutron-rich nucleus. The result is displayed in Figure 24, in which models predicting the point-neutron radius illustrate the correlation of A_{PV} and R_n [4]. For each model, the calculation is performed using the neutron and proton weak charges $q_n = 0.9878$ and $q_p = -0.0721$ and using the modeled neutron density but the experimental charge density. The importance of Coulomb distortions is emphasized by indicating results from plane-wave calculations, which are not all contained within the vertical axis range of the figure.

Clearly, a higher statistical accuracy will be needed to discriminate between the models and to pin down the symmetry energy to a level relevant for neutron stars and atomic parity violation. In the summer of 2011, PAC38 at JLab approved a proposal for a follow-up experiment (PREX-II) to reduce the error by a factor of 3. ^{208}Pb remains an attractive target because: 1) Lead is a very well-known nucleus and has a simple structure (doubly-magic); 2) It has the highest separation to the first excited state (2.6 MeV) of any heavy nucleus. Combined with the high momentum resolution of our spectrometers, this separation lends itself well to the flux integration detection technique; 3) ^{208}Pb is thought to have a relatively large value of R_n. 4) Since ^{208}Pb is a heavy nucleus, with a large number of extra neutrons, there should be a relatively clean interpretation of the skin thickness in terms of properties of bulk neutron matter.

There is also an interest in performing parity-violating measurements from other nuclei; the consensus on the candidates for a next series of runs are ^{48}Ca, ^{40}Ca, and isotopes of tin: ^{112}Sn, ^{120}Sn, and ^{124}Sn, see ref [4]. Statistical errors better than 1% appear to be feasible with 30 day runs. The ^{48}Ca measurement is optimized at a beam energy of $\sim$2 GeV, making it an ideal 1-pass experiment for Hall A in the 12 GeV era. We plan to propose a ^{48}Ca run at PAC39.

References

[1] PREX-II Proposal for PAC38, R. Michaels *et.al* (2011).

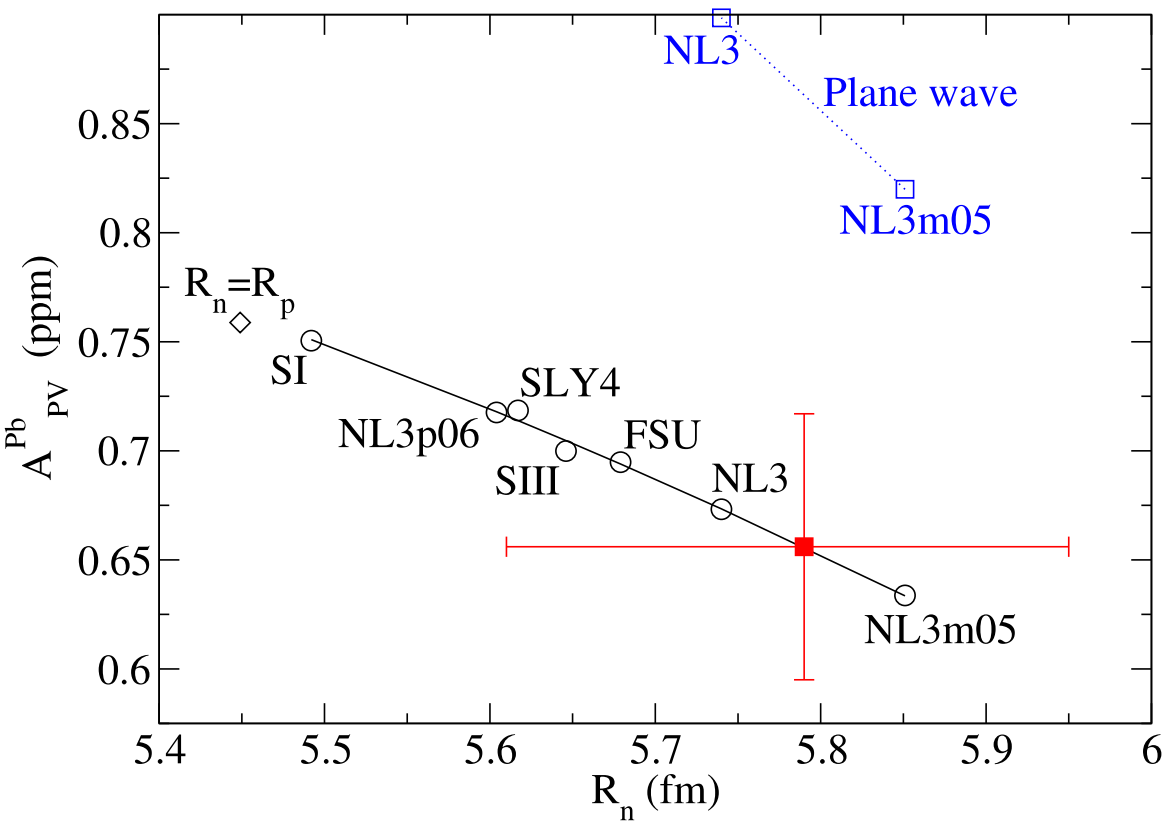

Figure 24: Result of this experiment (red square) vs neutron point radius R_n in ^{208}Pb. Distorted-wave calculations for seven mean-field neutron densities are circles, while the diamond marks the expectation for $R_n = R_p$. The blue squares show plane-wave impulse approximation results.

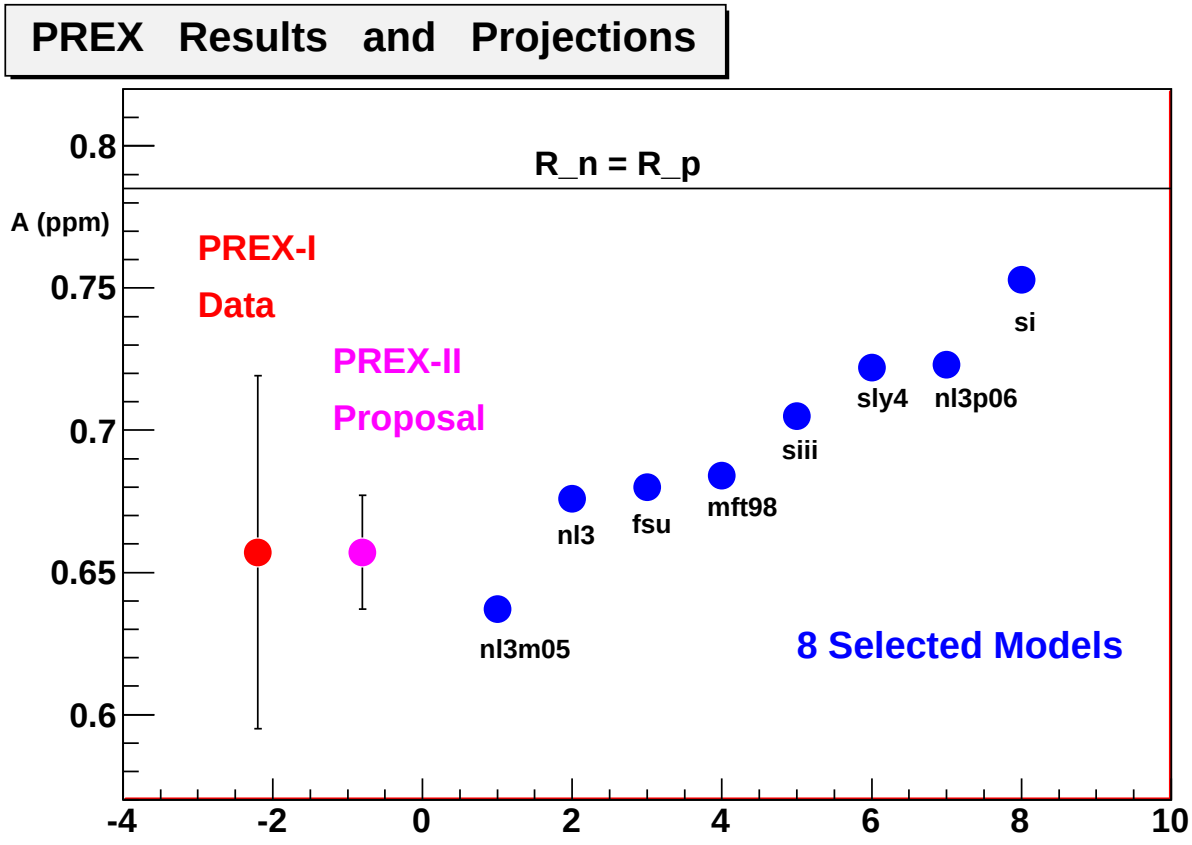

Figure 25: The PREX asymmetry for the PREX-I data, the PREX-II projections (new proposal for PAC38), and 8 selected models. Also shown is the asymmetry for the hypothesis that the neutron radius is the same as the proton radius. The references are shown in the PREX-II proposal.

[2] T.W. Donnelly, J. Dubach, and I. Sick, Nucl. Phys. A**503**, 589 (1989).

[3] C. J. Horowitz, Phys. Rev. C **57**, 3430 (1998).

[4] S. Ban, C.J. Horowitz, R. Michaels, J. Phys G **39** (2012) 015104.

3.8 E06-010 - Transversity

Measurement of Single Target-Spin Asymmetry in Semi-Inclusive Pion Electroproduction on a Transversely Polarized ^{3}He Target

J.-P. Chen, E. Cisbani, H. Gao, X. Jiang, J.-C. Peng co-spokespersons,
and
the Hall A Collaboration.

contributed by K. Allada. J. Huang, X. Qian

3.8.1 Introduction

Experiment E06-010 [1] collected data in Hall A from Oct. 2008 to Feb. 2009 using a transversely polarized ^{3}He target in order to measure target single-spin asymmetries (SSA) in ^{3}He$(e,e'h)$ reaction (where $h = \pi^+, \pi^-, K^+$ or K^-). The BigBite spectrometer was set at 30° on beam right to detect scattered electron with $0.8 < E' < 2.2$ GeV, the left HRS was used on beam left to detect the fragmented hadron in coincidence at $p_h = 2.35$ GeV/c and 16°. The goal of this experiment is to extract the Collins and Sivers single-spin asymmetry in semi-inclusive DIS reactions on neutron (^{3}He) in order to constrain quark transversity (quark transverse spin) and quark Sivers distributions, which reflect the correlation between the quark's transverse momentum and the nucleon's transverse spin.

Recently, the COMPASS experiment [2] published the Collins and Sivers SSA results on a transversely polarized proton target. While the proton Collins asymmetry of COMPASS, which is clearly non-zero, are consistent with that of HERMES [3], the Sivers asymmetry are smaller than those of HERMES [4] but not vanishing.

The data analysis of this experiment has been completed for the main reaction channels, which include SSA and DSA in the coincidence channels. The results are shown in Fig.1. Recently these results were published in [7, 8]. The upper panels of Figure 26 show the moments of the neutron Collins single-spin asymmetry for π^+ (left) and π^- (right)channels, respectively. The Collins moments on neutron are not large, mostly consistent with zero within the statistical uncertainties, except for the π^+ channel at the highest x-bin, where data favors a negative Collins moment. The lower panels of Figure 26 show the moments of the neutron Sivers single-spin asymmetry for π^+ (left) and π^- (right) channels. Again, the Sivers moments on neutron are relatively small, at the level of a few percent. For the π^+ channel, which favors the d-quark in nucleon, as π^+ carries a valence u-quark from neutron, and it is coupled with the "favored" fragmentation function, data suggests negative values for the Sivers moment, in general agreement with the trend predicted by Anselmino *et al*, noticeably smaller in magnitude. On the other hand, the Sivers moment of the π^- channel are consistent with zero within the total uncertainties.The DSA results are shown in Figure 27. The extracted $A^n_{LT}(\pi^+)$ is consistent with zero within the uncertainties, and $A^n_{LT}(\pi^-)$ is positive and its sign is consistent with various model predictions.

Currently our analysis is focused on two parasitic measurements done in the inclusive channels:

- Inclusive ^{3}He target single-spin asymmetry in the DIS A_y reaction ^{3}He$(e,e')X$.
- Single spin asymmetries in inclusive hadron production in Left HRS and the BigBite spectrometer.

The analysis of inclusive target SSA in DIS A_y is presented as a separate chapter in this report by J. Katich. We will discuss below the progress on the analysis of inclusive hadron production.

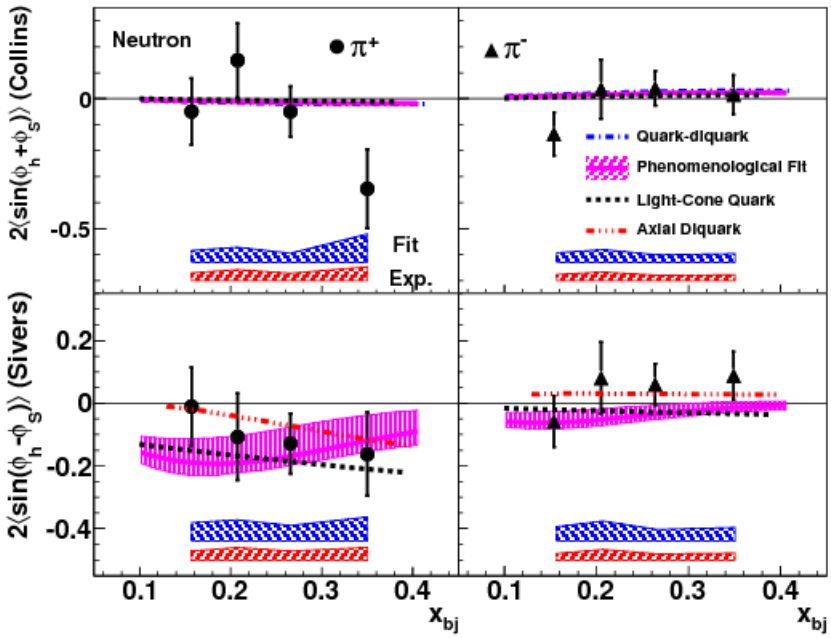

Figure 26: The results of Collins and Sivers moments of neutron are shown. The error bars represent the statistical uncertainties. The different sources of experimental systematic uncertainties are shown as a red band and systematics due to fitting an angular modulation to the asymmetry is shown in blue band. The magenta curve is the theoretical calculations from Anselmino *et al.* [5, 6]

3.8.2 Inclusive Hadron Production

Recently it has been suggested in [9] that the study of inclusive hadron production from a transversely polarized target, $eN^{\uparrow} \rightarrow hX$, where the scattered electron is not detected, can allow us to test the TMD factorization. This is essential in understanding the large single spin asymmetries (A_N) observed at high P_T in the proton-proton collisions, where one of the proton is transversely polarized [10, 11, 12].

In the E06-010 experiment, apart from the coincidence triggers, singles triggers on both Left HRS and BigBite were also collected. This allowed us to analyze the SSA for inclusive $\pi^{\pm}$, $K^{\pm}$, proton in the HRS, and for unidentified hadrons in the BigBite detector. In this experiment the BigBite detector did not have hadron identification capabilities. The phase space plot of P_T vs. x_F covered in this experiment is shown in Figure 29 for inclusive hadron SSA for $\pi^{\pm}$, proton and γ. The large acceptance of the BigBite detector and the two target spin states[1] allowed us to study the angular (ϕ_S) dependence of the asymmetries. Here ϕ_S is the angle between spin plane (defined by the incident beam direction and target spin direction), and the hadron plane (defined by the incident beam direction and the outgoing hadron direction).

At present the analysis is focused on identifying inclusive Kaons in the HRS using a RICH detector. During this experiment the performance of the RICH detector was not optimal, resulting in the overall inefficiency of this detector to be around 50%. Therefore the Kaon sample becomes statistically limited when cuts including the RICH detector were applied to the data. The Cerenkov angle reconstructed in the RICH detector is shown in Figure 28 for positive and negative HRS polarity data. The plot also shows the effectiveness of a Kaon χ^2 probability cut as described in [13] for identifying the Kaons. The bottom plots of Figure 28 shows clean Kaon sample after χ^2 cut.

[1]Target spin "Transverse" and "Vertical" with respect to the incoming beam direction.

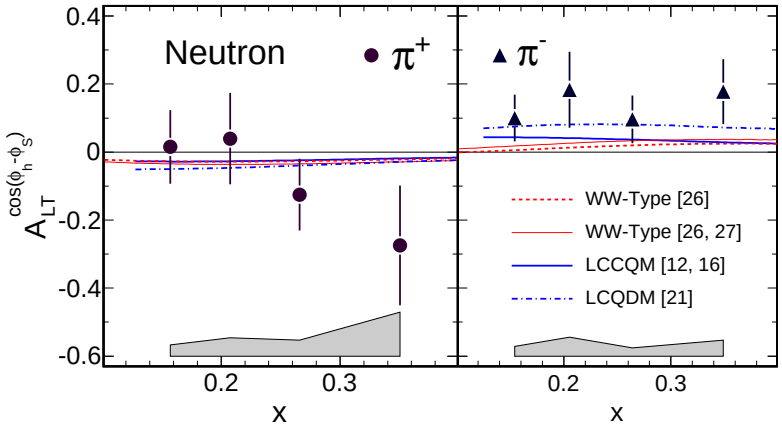

Figure 27: Neutron $A_{LT}^{cos(\phi_h-\phi_S)}$ azimuthal asymmetry for positive(left) and negative (right) charged pions vs Bjorken x.

The preliminary ^{3}He SSA obtained for π^+, π^- and proton in the HRS for two different target spin states are shown in Figure 30. When the target spin is in the transverse direction the asymmetry is near zero. This is due to the term $(k_1 \times k_2) \cdot S_T$ contributing to the cross-section. Here k_1 and k_2 are the momentum directions of the incoming electron and outgoing hadron, respectively, and S_T is the target spin direction. When the target spin is in vertical direction this term becomes non-zero, and hence we observe a non-zero asymmetry amplitude. The other feature of this result is that the asymmetry has an opposite sign for π^+ and π^-, and the asymmetry for protons has the same sign as that of π^+.

We expect to finish the analysis of SSA in inclusive hadron and SSA in the DIS A_y reaction within the next six months for publication.

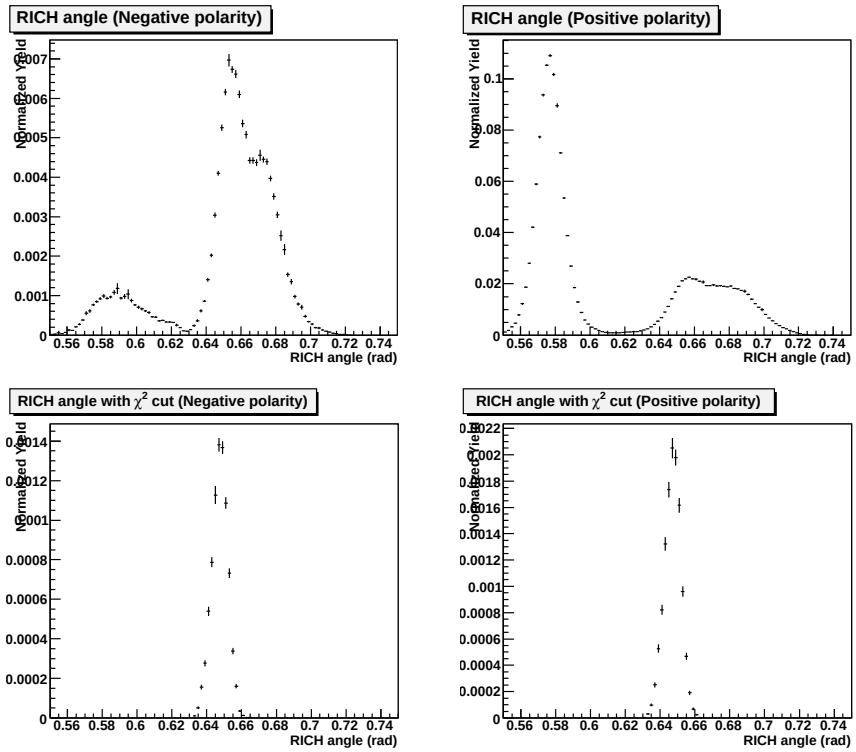

Figure 28: Reconstructed Cerenkov angle in the RICH detector for negative (top left) and positive (top right) HRS polarity. The bottom plots show the angle after χ^2 probability cut on Kaon angle reconstruction as described in [13]

References

[1] JLab E06-010, Spokespersons; J.-P. Chen, E. Cisbani, H. Gao, X. Jiang, and J.-C. Peng.

[2] M. G. Alekseev et al. *Phys. Lett.*, B692:240–246, 2010.

[3] A. Airapetian et al. *Phys. Rev. Lett.*, 94:012002, 2005.

[4] A. Airapetian et al. *Phys. Rev. Lett.*, 103:152002, 2009.

[5] M. Anselmino, M. Boglione, U. D'Alesio, A. Kotzinian, F. Murgia, A. Prokudin, and C. Türk. *Phys. Rev. D*, 75(5):054032, Mar 2007.

[6] M. Anselmino *et al.* *Phys. Rev.*, **D71**:074006, 2005.

[7] X. Qian et al. *Phys. Rev. Lett.*, 107:072003, 2011.

[8] J. Huang et al. arXiv:1108.0489.

[9] M. Anselmino *et al.* *Phys. Rev.*, **D81**:034007, 2010.

[10] D. L. Adam et al. *Phys. Lett. B*, 264:462, 1991.

[11] A. Braver et al. *Phys. Rev. Lett.*, 77:2626, 1996.

[12] L. Nogach et al. *AIP Conf. Proc.*, 915:543, 2007.

[13] G.M. Urciuoli *et al.* *NIM A*, 612:56, 2009.

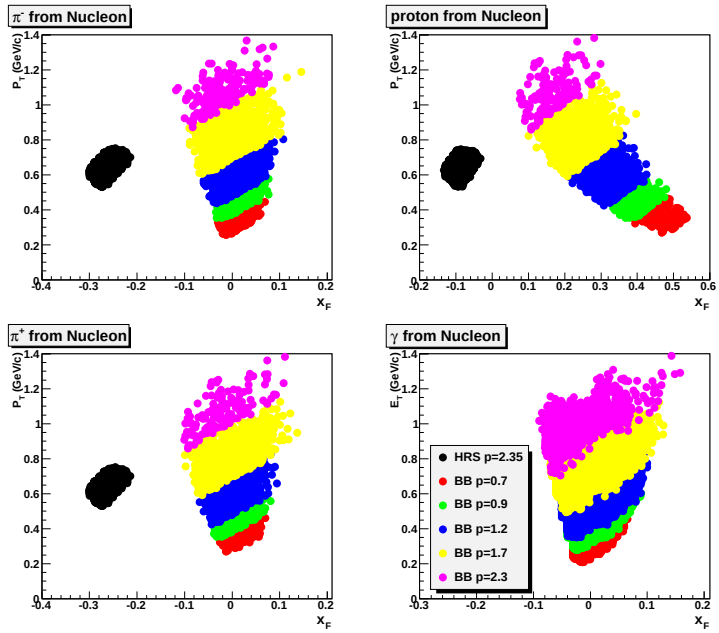

Figure 29: The phase space of P_T vs. x_F for different particles in the left HRS and in the BigBite. The BigBite phase space is shown in different momentum bins.

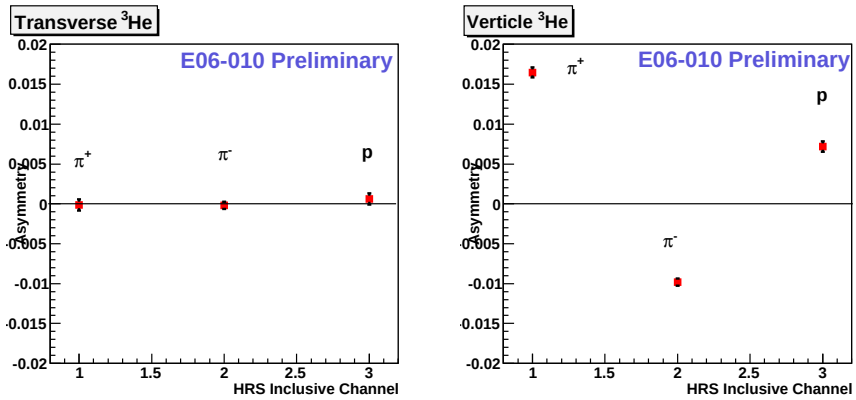

Figure 30: Preliminary ^{3}He SSA of π^+, π^- and proton obtained from HRS (p_0=2.35 GeV/c) for transverse (left) and vertical (right) target spin states. The asymmetries are corrected for target polarization but not corrected for the nitrogen dilution. The error bars represent only statistical uncertainties.

3.9 E06-014 - d_2^n

Precision Measurement of d_2^n: Probing the Lorentz Color Force

S. Choi, X. Jiang, Z.-E. Meziani, B. Sawatzky, spokespersons,
and
the d_2^n and Hall A Collaborations.
contributed by M. Posik, L. El Fassi, D. Flay, D. Parno, and Y. Zhang.

3.9.1 The Experiment

Experiment E06-014 ran in Hall A from February 7 to March 17, 2009, at two production beam energies of 4.73 and 5.89 GeV, on a polarized ^{3}He target. In this experiment the resonance and deep inelastic valence quark regions were probed, which corresponded to the ranges $0.15 \leq x \leq 1.0$ and $1.5\ \text{GeV}^2 \leq Q^2 \leq 7\ \text{GeV}^2$. Figure 31 shows the coverage in Q^2 and x. Included in this plot is the invariant mass W at a value of 2 GeV, which separates the resonance and deep inelastic regions. The LHRS and BigBite detector packages were each oriented at 45° relative to the beam line, with each of the detectors independent of one another, acting as its own single-arm experiment. The LHRS was used to measure the unpolarized cross-section, while the BigBite measured the double-spin asymmetries in scattering between a longitudinally polarized electron beam and a longitudinally and transversely polarized ^{3}He target.

E06-014 also served as the commissioning experiment for a gas Čerenkov detector, which was installed into the the BigBite stack, as well as a new photon detector and integrating data-acquisition system for the Compton polarimeter [1, 2, 3, 4].

The primary goal of E06-014 is the measurement of the quantity d_2^n. The neutron d_2 is a probe of the strong force that is formed by taking the second moment of a linear combination of the polarized structure functions g_1 and g_2:

$$d_2^n\left(Q^2\right) = \int_0^1 x^2 \left[2g_1^n\left(x,Q^2\right) + 3g_2^n\left(x,Q^2\right)\right] dx. \tag{9}$$

At low Q^2 where the virtual photon wavelength is larger than the nucleon, d_2 can be associated with spin polarizabilities of the nucleon [5, 6]. However, at larger Q^2, it is more appropriate to interpret d_2 as the average transverse Lorentz color force acting on a quark after being hit by a virtual photon [5, 7].

In addition to gaining insight into the nature of the color force, the precision measurement of d_2^n will also be a benchmark test for lattice QCD predictions.

E06-014 measured d_2^n by combining the unpolarized cross-section, σ_0 from the LHRS, as well as the parallel and perpendicular asymmetries, $A_\parallel$ and $A_\perp$ from BigBite. The asymmetries are defined through the counting rates of each spin orientation as:

$$A_\parallel = \frac{N^{\downarrow\Uparrow} - N^{\uparrow\Uparrow}}{N^{\downarrow\Uparrow} + N^{\uparrow\Uparrow}} \quad \text{and} \quad A_\perp = \frac{N^{\downarrow\Rightarrow} - N^{\uparrow\Rightarrow}}{N^{\downarrow\Rightarrow} + N^{\uparrow\Rightarrow}},$$

where single arrows represent the electron helicity direction, and double arrows represent the target polarization direction. By combining these independently measured quantities, d_2^n is expressed exclusively through experimental quantities as:

$$d_2^n = \int_0^1 \frac{MQ^2}{4\alpha^2} \frac{x^2y^2}{(1-y)(2-y)} \sigma_0 \left[\left(3\frac{1+(1-y)\cos\theta}{(1-y)\sin\theta} + \frac{4}{y}\tan(\theta/2)\right) A_\perp + \left(\frac{4}{y} - 3\right) A_\parallel\right] dx, \tag{10}$$

where $\nu = E - E'$ is the energy transfer from electron to target, θ is the scattering angle of the electron and $y = \nu/E$ is the fractional energy transfer from electron to target. The advantage of measuring d_2^n in terms of experimental quantities is that it allowed the allotted beam time to be divided between measuring $A_\parallel$ and $A_\perp$ in such a way that the error on d_2^n was minimized, rather than minimizing the error on the spin structure functions g_1^n and g_2^n. The measurement of $d_2^n\left(Q^2 \approx 3\ \text{GeV}^2\right)$ is expected to result in a fourfold improvement on the world data as shown in Figure 32, in advance of an approved 12 GeV experiment in Hall C that will extend the precision measurement of d_2^n to higher kinematic ranges [16].

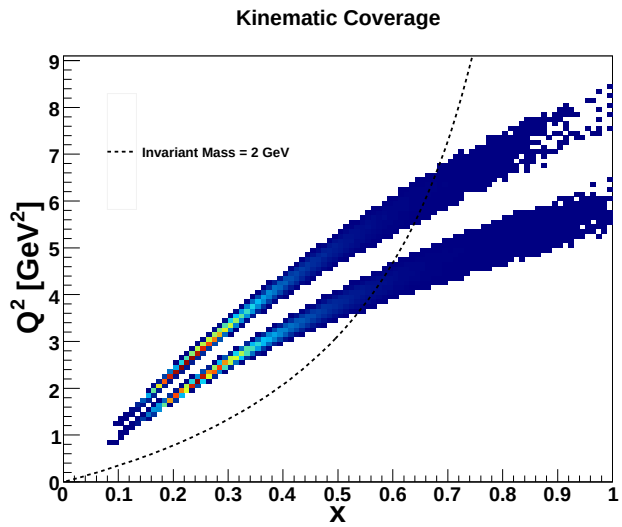

Figure 31: Shown is E06-014's coverage in Q^2 and x. The lower band is the 4.73 GeV dataset and the upper band is the 5.89 GeV dataset. The black dashed line shows W = 2 GeV. $W < 2$ GeV corresponds to x values to the right of the dashed line, which distinguishes the resonance region. $W > 2$ GeV corresponds to the x values to the left of the dashed line, which defines the deep inelastic region.

In addition to the primary goal of E06-014, the data collected can also be used to measure the longitudinal virtual photon-nucleon asymmetry for the neutron, A_1^n. The virtual photon-nucleon scattering cross section can be separated into two helicity-dependent cross sections, $\sigma_{1/2}$ and $\sigma_{3/2}$. The subscript 1/2(3/2) gives the projection of the total spin along the virtual photon's momentum direction, corresponding to anti-parallel (parallel). A_1 can then be defined as:

$$A_1\left(x,Q^2\right) \equiv \frac{\sigma_{1/2}-\sigma_{3/2}}{\sigma_{1/2}+\sigma_{3/2}} \approx \frac{g_1\left(x,Q^2\right)}{F_1\left(x,Q^2\right)} \text{ for high } Q^2, \tag{11}$$

were F_1 is the unpolarized structure function. We may also express A_1 in terms of the parallel and perpendicular asymmetries, $A_\parallel$ and $A_\perp$, that were measured in BigBite as:

$$A_1 = \frac{1}{D\left(1+\eta\xi\right)}A_\parallel - \frac{\eta}{d\left(1+\eta\xi\right)}A_\perp \tag{12}$$

where D is the virtual photon polarization factor and η, ξ, and d are quantities set by kinematics and by the virtual photon polarization vector [2].

Combining A_1^n data measured on an polarized effective neutron target with A_1^p data measured on a polarized proton target, allows access to the polarized-unpolarized parton distribution function ratios $\Delta u/u$ and $\Delta d/d$. Recent results from Hall A [17] and from CLAS [18] showed a significant deviation of $\Delta d/d$ from the predictions of perturbative

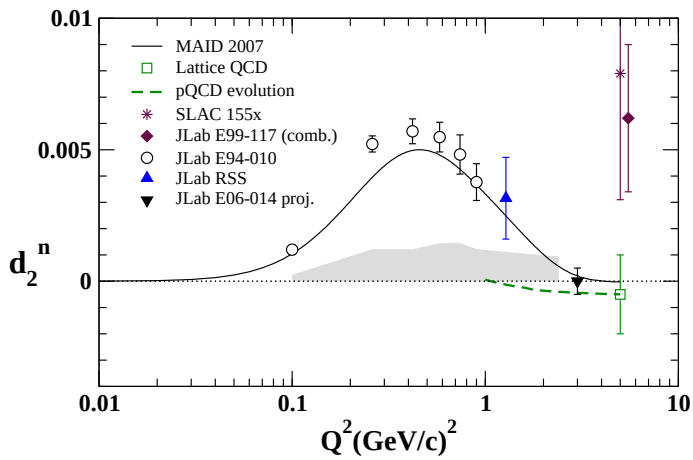

Figure 32: All the data shown with the exception of the SLAC E155x data, are dominated by resonance contribution. E06-014 data will observe mostly the DIS contribution. The projected error on from E06-014 [8] is shown, along with the lattice QCD result [9]. The pQCD evolution from the lattice point was performed by Patricia Solvignon, which was based on papers by Shuyak and Vainshein [10] and Ji and Chou [11]. Data from JLab experiments E94-010 [12] and RSS [13] are included in the plot. For comparison to the resonance contribution, a MAID model [14] is plotted. Also plotted is the total d_2 from SLAC experiment E155x [15].

QCD, which have that ratio approaching 1 in the limit of $x \to 1$. As part of the 12 GeV program, two approved experiments (one in Hall A [19] and one in Hall C [20]) will extend the accuracy and x range of this measurement, but a measurement of A_1^n at E06-014's kinematics will provide valuable support (or refutation) of prior Jefferson Lab results, while producing additional input for theoretical models in advance of the coming experiments at 12 GeV.

3.9.2 Analysis Progress: Target and Beam

When performing a double-spin asymmetry experiment, knowledge of the target and beam polarization is crucial. E06-014 used the standard Hall A polarized ^{3}He target with two holding field directions: longitudinal and transverse in plane with respect to the beam direction. To extract the target polarization, EPR and NMR measurements were done. Since the calculation of target polarization from EPR and NMR measurements depends on the ^{3}He density, a complete understanding of the density is essential.

The number density of ^{3}He was measured in both the pumping chamber and the target chamber. This measurement was achieved by using the fact that collisions with ^{3}He atoms broaden the D1 and D2 absorption lines of rubidium [21]. By measuring the width of the D1 and D2 absorption lines and subtracting a 1% N_2 contribution, a measurement of n_0, the ^{3}He number density at room temperature can be obtained.

$$n_{pc} = n_0 \left[1 + \frac{V_{pc}}{V_{tot}} \left(\frac{T_{tc}}{T_{pc}} - 1 \right) \right]^{-1} \tag{13}$$

$$n_{tc} = n_0 \left[1 + \frac{V_{tc}}{V_{tot}} \left(\frac{T_{pc}}{T_{tc}} - 1 \right) \right]^{-1} \tag{14}$$

Since the number density changes with temperature, Equations 13 and 14 were used to compute the number densities[2] in both the pumping and target chambers, where V_{tot} is the total volume of the target cell, T is the temperature and the subscripts pc (tc) refer to the pumping (target) chamber. The temperature of the chambers was measured using

[2]Densities were calculated in units of amagat, where an amagat (amg) is 2.687 $\times 10^{25}$ m^{-3}.

seven resistive thermal devices (RTDs), which were placed outside of the target and were stable within 2°C during production [2]. The ^{3}He number densities for the E06-014 target cell, Samantha, as a function of run number can be seen in Figure 33, with the average values listed in Table 6.

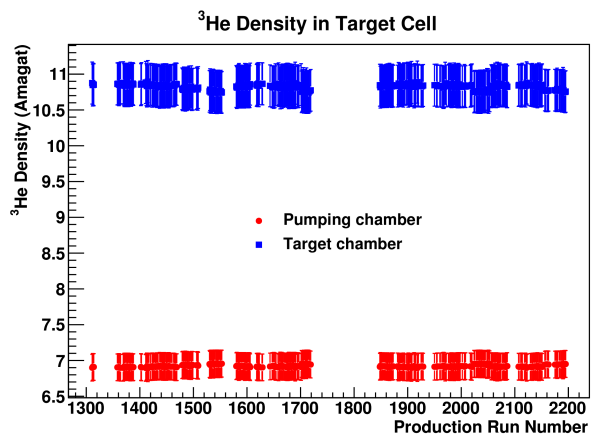

Figure 33: ^{3}He densities as a function of BigBite run number [2]

Chamber	^{3}He Density (amg)
Pumping	6.93 ± 0.19
Target	10.81 ± 0.29

Table 6: Average ^{3}He densities in target cell [2, 22]

During E06-014, EPR measurements were taken every several days, while NMR measurements were taken every four hours. During EPR measurements, the frequency shift of potassium level transitions in the presence of polarized ^{3}He was measured. This frequency shift $\Delta\nu_{EPR}$ can be related to the target polarization, $P_{^3\mathrm{He}}$:

$$\Delta\nu_{EPR} = \frac{4\mu_0}{3}\frac{d\nu_{EPR}}{dB}\kappa_0\mu_{^3\mathrm{He}}n_{pc}P_{^3\mathrm{He}}, \tag{15}$$

where μ_0 is the vacuum permeability, $\mu_{^3\mathrm{He}}$ is the magnetic moment, $\frac{d\nu_{EPR}}{dB}$ is the derivative of the EPR frequency with respect to the magnetic field, κ_0 is the enhancement factor and n_{pc} is the pumping chamber number density. During EPR measurements, a NMR measurement was done simultaneously. This allows for a comparison between the EPR polarization, $P_{^3\mathrm{He}}$, and the measured NMR amplitude, h. A conversion factor c' can then be formed that allows NMR measurements to be converted into an absolute ^{3}He polarization, and is defined as:

$$c' = \frac{P_{^3\mathrm{He}}}{h}. \tag{16}$$

In addition to obtaining the conversion factor c' from comparing EPR and NMR measurements, it can also be calculated by performing a calibration on a water target. The final NMR polarization is then computed by taking the weighted average of the polarization computed from the EPR and water calibrations. Although the water calibration still needs to be done in order to obtain the final target polarization, the EPR measurements can be used to obtain a preliminary target polarization. The average conversion factor c' for all EPR measurements in each target polarization direction, which can be seen in Table 7, was computed and applied to the NMR measurements. A linear interpolation was then done in order to obtain the polarization on a run-by-run basis. This procedure resulted in a combined systematic and statistical error of 4.9% as shown in Figure 34 [2, 22].

Polarization Direction	c'(%/mV)
Longitudinal	2.84 ± 0.14
Transverse	1.77 ± 0.09

Table 7: EPR-NMR conversion factors c' [2, 23]

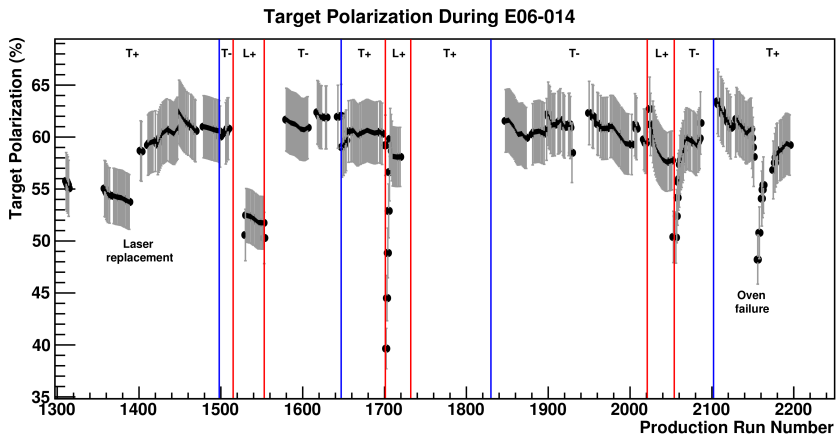

Figure 34: Preliminary target polarization based on linear interpolation of NMR polarization measurements calibrated using EPR results. Red lines show spin transitions between transverse and longitudinal orientations. Blue lines show 180° rotations of spin orientation within a polarization plane. The labels at the top of the graph give the polarization direction during that time period: $L_+ = 0°$,$T_- = 90°$ and $T_+ = 270$ [2].

In addition to the target polarization, the beam polarization also needs to be known. E06-014 used a polarized electron beam at energies of 4.73 and 5.89 GeV. The polarization of the electron beam was measured independently through Compton and Møller scattering. During the running of E06-014, there were several Møller measurements performed, while Compton measurements were taken continuously throughout the experiment. Figure 35 shows the beam polarization as a function of BigBite run number for the Møller and Compton results. The beam polarization data was split into four run sets and the average polarization for each run period was then computed by taking into account both the Compton and Møller data. The final beam polarizations can be seen in Table 8 [2].

Run Set	Beam Energy (GeV)	P_e from Compton	P_e from Møller	Combined P_e
1	5.90	0.726 ± 0.018	0.745 ± 0.015	0.737 ± 0.012
2	4.74	0.210 ± 0.011	-	0.210 ± 0.011
3	5.90	0.787 ± 0.020	0.797 ± 0.016	0.793 ± 0.012
4	4.74	0.623 ± 0.016	0.628 ± 0.012	0.626 ± 0.010

Table 8: Final beam polarization for E06-014, corrected for beam fluctuations. For run set 2 there was no Møller measurement. [2]

3.9.3 Analysis Progress: LHRS

The LHRS was used to measure the total unpolarized cross section, which will multiply the measured asymmetries in BigBite. In order to measure the unpolarized cross section, the LHRS hardware must be calibrated and particle identification (PID) cuts applied in order to select a particular particle type from the data [1]. The total unpolarized cross section is given as:

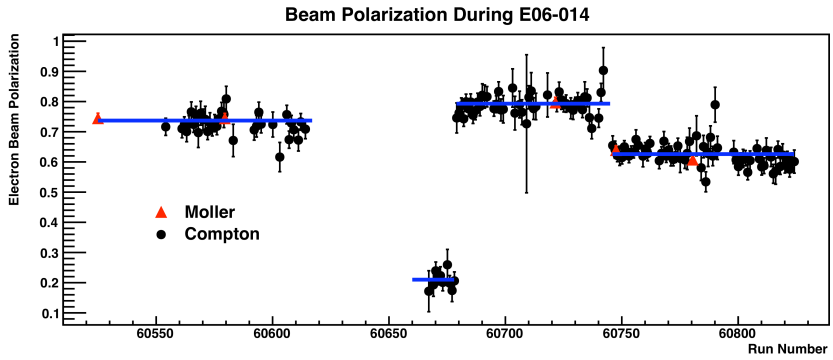

Figure 35: Final electron beam polarization from Møller and Compton measurements for E06-014. Note there was no Møller measurement for the second run set [2].

$$\sigma_0 = \frac{N \cdot ps \cdot e}{\varepsilon \cdot w \cdot Q \cdot t_{LT} \cdot n \cdot \Delta Z \Delta\theta \Delta\phi \Delta E'}, \tag{17}$$

where N is the number of events counted that passed the PID cuts, ps is the pre-scale factor, ε is the detector efficiency, Q is the the total charge on target, t_{LT} is the trigger live time, n is the target density, ΔZ is the effective target length as seen by the LHRS, $\Delta\theta$ is the vertical (dispersive) angle, $\Delta\phi$ is the horizontal (transverse) angle, $\Delta E'$ is the electron energy width seen by the LHRS, and w is an acceptance weight factor.

Due to the magnetic fields created by the LHRS magnets, the actual acceptance may not coincide with the geometrical apertures of the LHRS. To account for this difference, a weight factor is computed. In order to determine the weight factor w, a Single Arm Monte Carlo (SAMC) simulation was utilized. The simulation randomly generates particle trajectories that are larger in momentum and solid angle ranges than the actual acceptance. The same cuts that are used in determining the electron events from production data are then applied to the events generated from SAMC. This event count will now be referred to as N_{MC}^{trial}. The simulation then uses John LeRose's transport matrices [24], to propagate the N_{MC}^{trial} events through the LHRS. As the particle approaches each magnet aperture in the LHRS, a check is performed to see if the particle passes through the aperture. For all events that make it to the focal plane, the event is reconstructed at the target. These events are referred to as N_{MC}^{acc}. The ratio of $\frac{N_{MC}^{acc}}{N_{MC}^{trial}}$ then forms the acceptance weight factor w [25]. In Figure 36, we see the results from SAMC compared to actual production data for the target length seen by the LHRS, the vertical and horizontal angular distributions and $\delta p/p$. The acceptance weight is approximately 0.99.

The raw ^{3}He cross-section measured in the LHRS, σ_{raw}, contains contributions from electrons which do not originate from scattering off ^{3}He nuclei, but rather from pair production processes and scattering from nitrogen nuclei. Nitrogen gas is present in the pumping chamber to optimize ^{3}He polarization [21]. Some of the nitrogen gas diffuses from the pumping chamber into the target chamber where interactions with the electron beam take place. In order to remove the pair production and nitrogen contributions from σ_{raw}, several runs were taken with the LHRS in positive polarity mode during which positrons were detected. From these runs a positron cross-section, σ_{e+}, was measured. To obtain the nitrogen scattering contribution that is present during ^{3}He runs, a reference target cell was used. The reference cell was similar in geometry to the ^{3}He cell but was filled with nitrogen gas. By scattering electrons from the nitrogen target, a nitrogen cross-section, $\sigma_{N_2}^{e-}$ was measured. Since pair production is also present when scattering electrons off of nitrogen nuclei, a nitrogen positron cross-section, $\sigma_{N_2}^{e+}$ was also measured with the LHRS in positive polarity mode. The nitrogen positron cross-section was subtracted from the nitrogen cross-section to avoid double counting pair production events which were already accounted for in the ^{3}He positron cross-section. In order to account for the probability of scattering from nitrogen nuclei present in the ^{3}He target cell, the nitrogen cross-sections were weighted by the atomic densities. The weighted nitrogen cross-section, $\sigma_{N_2}^{dil}$, is called the diluted

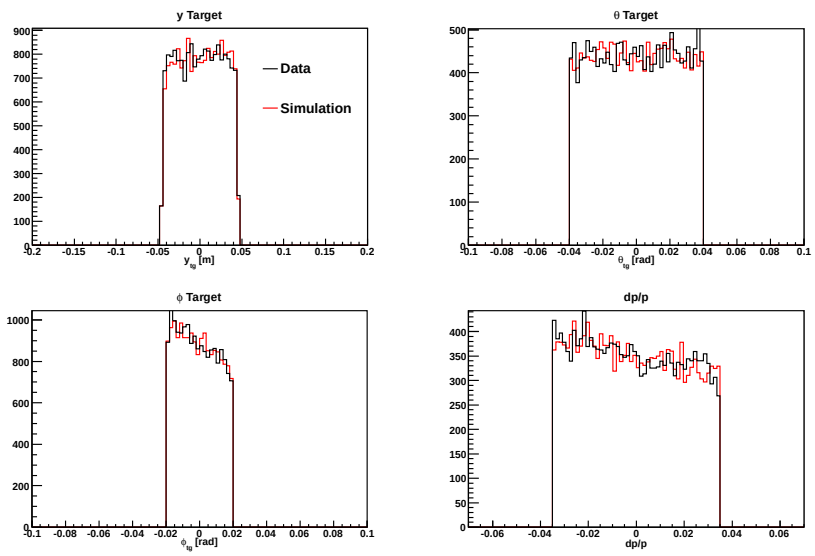

Figure 36: Comparison of events that passed in SAMC to E06-014 production data from LHRS.

nitrogen cross-section and is defined as:

$$\sigma_{N_2}^{dil} = \frac{n_{N_2}}{n_{N_2} + n_{^3He}} \left(\sigma_{N_2} - \sigma_{N_2}^{e+} \right) = \sigma_{N_2}^{dil,e-} - \sigma_{N_2}^{dil,e+}, \tag{18}$$

where n_{N_2} and $n_{^3He}$ are the nitrogen and ^{3}He densities.

σ_{raw} can now be corrected for pair production processes and nitrogen scattering contributions by:

$$\sigma_{exp} = \sigma_{raw} - \sigma_{e+} - \sigma_{N_2}^{dil} \tag{19}$$

Figure 37 shows the 4.73 and 5.89 GeV raw, positron, nitrogen, diluted nitrogen and corrected cross-sections measured in the LHRS as a function of x. With the preliminary 4.73 and 5.89 GeV cross-sections completed [26], analysis is now being done to apply radiative corrections to the cross sections.

3.9.4 Analysis Progress: BigBite

E06-014 used the BigBite detector package to measure the double spin asymmetry between longitudinally polarized electrons and a longitudinally and transversely polarized ^{3}He target. The BigBite detector calibrations and data quality checks have been completed for the 4.73 GeV data set [1, 2]. Preliminary asymmetry analysis at a beam energy of 4.73 GeV has also been completed. The longitudinal and transverse asymmetries were computed using Equation 10. The kinematic range ($0.15 \leq x \leq 1.0$) has been divided into 17 equally spaced x bins. As can be seen from Figure 31, this data set is in the deep-inelastic scattering (DIS) regime ($W > 2$) for $x \leq 0.52$; above this value, the data are in the resonance region.

Since the ^{3}He target has a small percentage of N_2 present, as shown in Section 3.9.3, the unpolarized N_2 gas will tend to dilute the measured asymmetries. In order to correct for this in BigBite, counting rates from a pure N_2 target was also measured. Comparing the N_2 target counting rates to the ^{3}He production cell scattering rates, a dilution factor can be formed and applied to the measured asymmetry. The dilution factor is given by Equation (20):

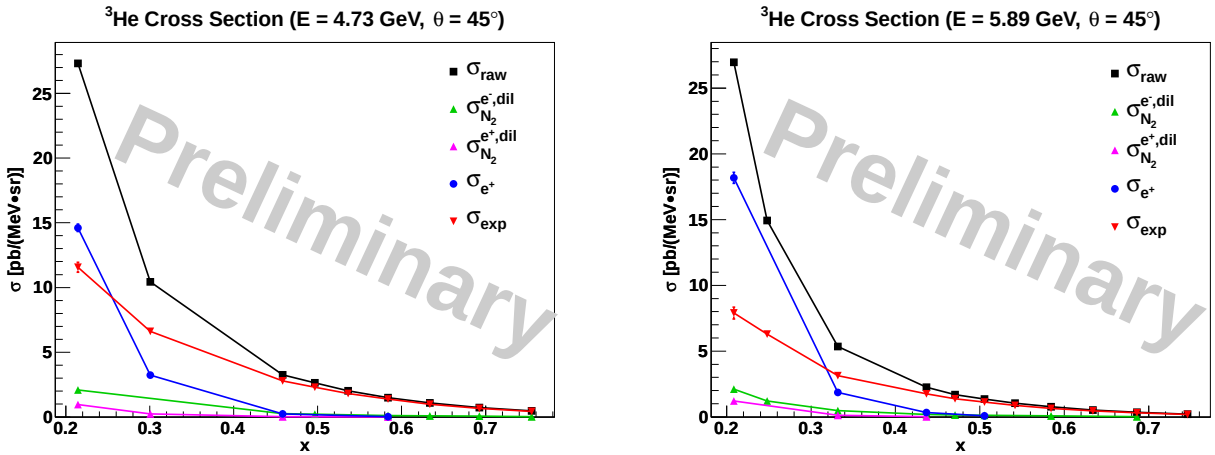

(a) 4.73 GeV (b) 5.89 GeV

Figure 37: LHRS preliminary cross sections as a function of x. Radiative corrections have not been applied to the cross sections, and error bars shown are statistical only.

$$D_{N_2} = 1 - \frac{\Sigma_{N_2}(N_2)}{\Sigma_{total}(^3He)} \frac{Q(^3He) n_{N_2}(^3He)}{Q(N_2) n_{N_2}(N_2)}, \tag{20}$$

where Σ_{N_2} and Σ_{total} are the total scattering counts that pass data-quality and PID cuts detected during the N_2 and ^{3}He target runs. Q(N_2) and Q(^{3}He) are the total charge deposited on the two targets and $n_{N_2}(N_2)$ and $n_{N_2}(^3He)$ are the nitrogen number densities present in the two targets. The dilution factor was computed at each of the 17 x bins. Figure 38 shows the results of the nitrogen dilution calculations.

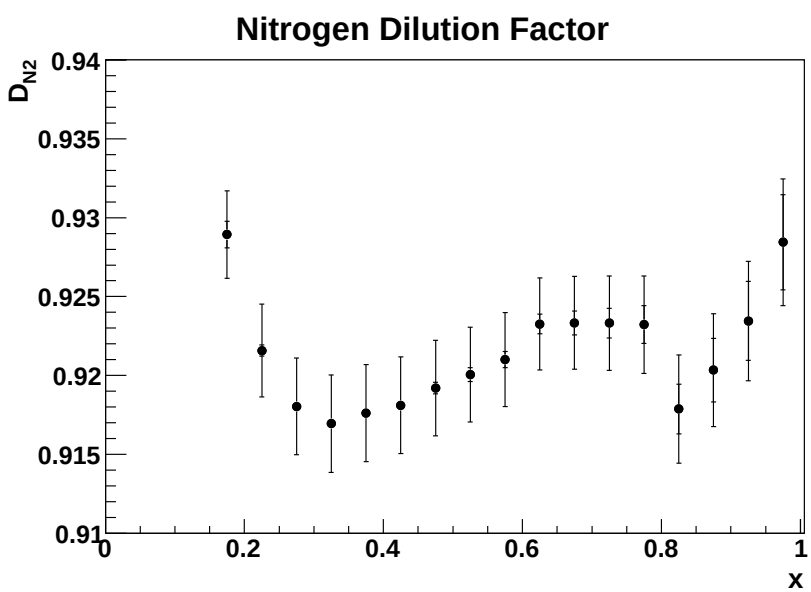

Figure 38: Preliminary N_2 dilution factor is plotted vs x at a beam energy of 4.73 GeV. Outer error bars show combined systematic and statistical errors. The inner error bars show only statistical errors. In some bins, the statistical error is too small to be seen on the graph.

In addition to correcting for nitrogen dilution, corrections for target and beam polarizations must also be applied

since the target and beam were not fully polarized. This is accounted for by dividing the asymmetries by the measured target and beam polarizations, P_t and P_b, found in Figure 34 and Table 8. The physics asymmetries are then given as:

$$A_{\parallel} = \frac{1}{P_b P_t D_{\mathrm{N}_2}} A_{\parallel}^{raw},\ A_{\perp} = \frac{1}{P_b P_t D_{\mathrm{N}_2} \cos(\phi)} A_{\perp}^{raw}, \tag{21}$$

where ϕ is the vertical scattering angle. Figure 39 shows the physics asymmetries on ^{3}He at an electron beam energy of 4.73 GeV as a function of x. These asymmetries can also be used to form longitudinal virtual photon-nucleus asymmetry on ^{3}He, $A_1^{^3\mathrm{He}}$ via Equation 12. Preliminary E06-014 A_1 asymmetry measurements on ^{3}He are in good agreement with previous A_1 asymmetry measurements, as can be seen in Figure 40. E06-014's largest sources of systematic error on the 4.73 GeV data set are due to the target polarization measurement, the contamination of the DIS electron sample by pair-production processes, and errors in momentum assignment. Completing and finalizing the target water calibration will substantially reduce the systematic error. A complete study of backgrounds must await analysis of the larger 5.89 GeV data set, during which time trigger thresholds were lower and correspondingly background rates were higher. Initial calibrations and data quality checks have just been completed on the 5.89 GeV data set, with asymmetry and background studies to follow shortly.

The extraction of the neutron asymmetry A_1^n at 4.73 GeV beam energy is also underway, however, the extraction is model-dependent. Previous experiments [17] have used Bissey *et al.*'s complete model in the DIS regime [27]. However, E06-014's 4.73 GeV data set spans both the DIS and resonance regions. A consistent treatment of both DIS and resonance data requires careful consideration of structure-function smearing [28]. We are working with W. Melnitchouk to extract neutron asymmetries across our entire kinematic range.

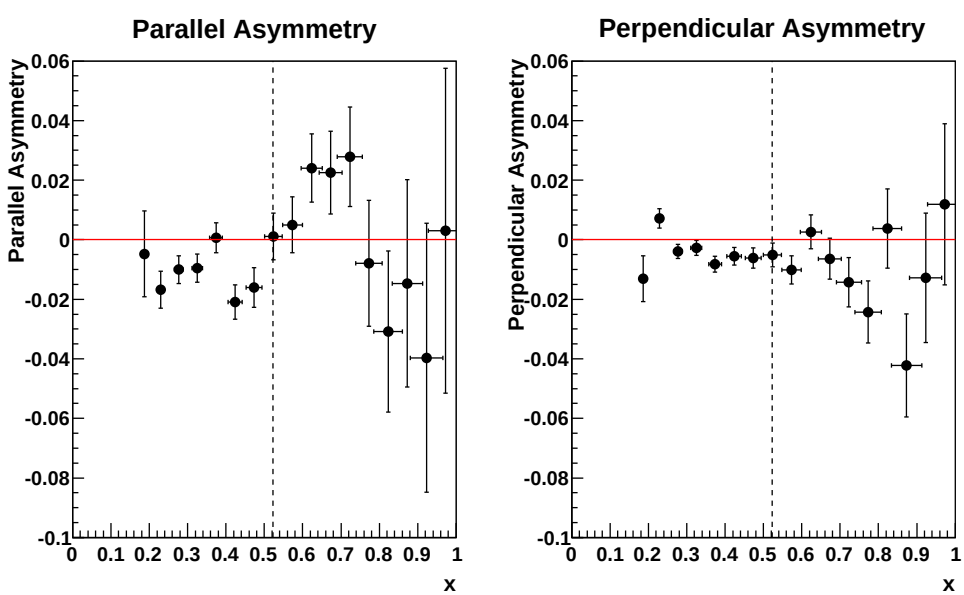

Figure 39: Preliminary $A_{\parallel}$ and $A_{\perp}$ on ^{3}He are plotted vs x at a beam energy of 4.73 GeV [2]. The dashed line is $W = 2$ GeV, which distinguishes the DIS region (to the left of the dashed line) from the resonance region (to the right of the dashed line).

References

[1] D. Parno *et al.*, http://hallaweb.jlab.org/experiment/E06-014/talks/index.html, E06014 Analysis Status Report (12/2010)

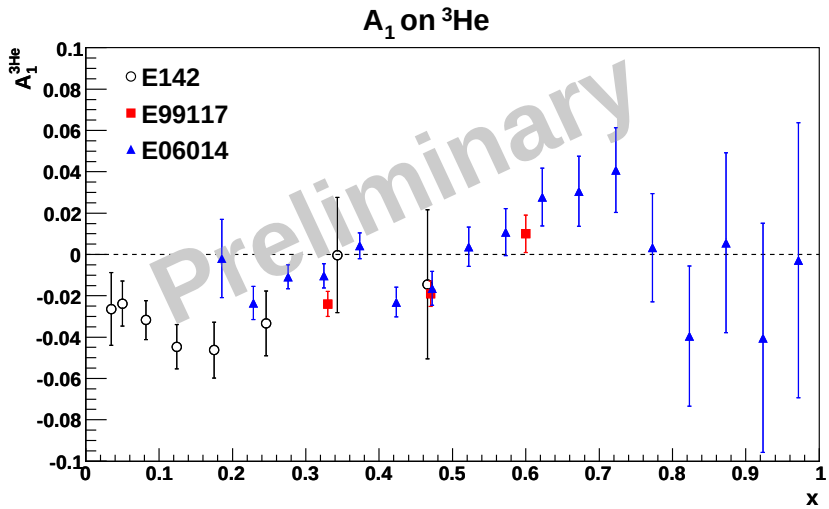

Figure 40: Preliminary E06-014 measurement of $A_1^{^3\mathrm{He}}$ at 4.73 GeV, compared to ^{3}He data from E142 at SLAC [29] and E99-117 in Hall A [17] [2].

[2] D. Parno, PhD thesis, Carnegie Mellon University (2011).

[3] D. Parno *et al.*, Proceedings of the 2010 International Nuclear Physics Conference, J. Phys.: Conf. Ser. **312** 052018 (2011), arXiv:1106.4851 [physics.ins-det]

[4] M. Friend *et al.*, arXiv:1108.3116 [physics.ins-det]

[5] M. Burkardt, hep-ph/0905.4079v1 (2009).

[6] E. Stein *et al.*, Phys. Lett. B **343**, 369 (1995).

[7] M. Burkardt, AIP Conference Proceedings **1149**, 62 (2008), hep-ph/0902.0163v1.

[8] S. Choi, Z.-E. Meziani, X Jiang, B. Sawatzky, *et al.*, Jefferson Lab PAC PR-06-014 (2005).

[9] M. Gockeler *et al.*, Phys. Rev. D **72**, 054507 (2005), [arXiv:hep-lat/0506017].

[10] Shuyak and Vainshein, Nucl. Phys. B **201**, 141 (1982).

[11] Ji and Chou, Phys. Rev. D **42**, 3637 (1990).

[12] M. Amerian *et al.*, Phys. Rev. Lett. **89**, 242301 (2002); Phys. Rev. Lett. **92**, 022301 (2004); Phys. Rev. Lett. **93**, 152301 (2004); Z.-E. Meziani *et al.*, Phys. Lett. B **613**, 148 (2005); K. Slifer *et al.*, Phys. Rev. Lett. **101**, 22303 (2008).

[13] K. Slifer *et al.*, (Resonance Spin Structure) (2008), 0812.0031.

[14] D. Drechsel, S. S. Kamolov, and L. Tiatar, Eur. Phys. J. **A34**,69 (2007), 0710.0306.

[15] P. L. Anthony *et al.*, (E155), Phys. Lett. B **553**, 18 (2003), hep-ex/0204028.

[16] T. Averett, W. Korsch, Z.-E. Meziani, B. Sawatzky*et al.*, Jefferson Lab PAC E1206121 (2010).

[17] X. Zheng *et al.*, Phys. Rev. C **70**, 065207 (2004).

[18] K. V. Dharmawardane *et al.*, Phys. Lett. B **641**, 11 (2006).

[19] G. Cates, N. Liyanage, Z.-E. Meziani, G. Rosner, B. Wojtsekhowski, X. Zheng, *et al.*, Jefferson Lab PAC E1206122 (2006).

[20] G. Cates, J.-P. Chen, Z.-E. Meziani, X. Zheng *et al.*, Jefferson Lab PAC E1210101 (2010).

[21] I. Kominis, Ph.D. thesis, Princeton University (2001)

[22] Y. Zhang, Target analysis for E06-014. http://jlab.org/yawei/d2n/targ ana.html

[23] Y. Zhang, Electron paramagnetic resonance (EPR) project summary. Technical report, Hall A Collaboration (2011), http://www.jlab.org/yawei/weeklymeeting/110209/epr.pdf

[24] J. J. Lerose, Transfer Functions for Hall A Spectrometers, *http://hallaweb.jlab.org/news/minutes/tranferfuncs.html*

[25] V. Sulkosky, Ph.D. thesis, The College of William and Mary (2007).

[26] D. Flay, PANIC 2011 Presentation, http://hallaweb.jlab.org/experiment/E06-014/talks/flay_panic11_final.pdf

[27] F. Bissey *et al.*, Phys. Rev. C **65**, 064317 (2002).

[28] S. A. Kulagin and W. Melnitchouk, Phys. Rev. C **78**, 065203 (2008).

[29] P. L. Anthony *et al.*, Phys. Rev. D **54**, 6620 (1996).

3.10 E07-006 - Short Range Correlations

Graduate students: Or Hen (TAU), Igor Korover (TAU), Navaphon Muangma (MIT).

S. Gilad (MIT), D. Higinbotham (JLab), V. Sulkosky (MIT) and J. Watson (KSU), spokespersons,
and
the Hall A Collaboration.
contributed by E. Piasetzky (TAU).

Experiment E07-006 (SRC) [1] was proposed to continue the study of short-range nucleon-nucleon (NN) correlations. During the first high luminosity triple coincidence experiment at JLab, E01-015, we measured the $(\mathrm{e},\mathrm{e}'\mathrm{pp})$ and $(\mathrm{e},\mathrm{e}'\mathrm{pn})$ reactions on ^{12}C over the $(\mathrm{e},\mathrm{e}'\mathrm{p})$ missing momentum range from 275 to 550 MeV/c. These measurements were sensitive to the short-range NN tensor force. The new triple coincidence experiment was proposed to measure these reactions on ^{4}He over the missing momentum range from 400 to 875 MeV/c in order to study the short-range repulsive part of the NN interaction and investigate the transition from a tensor-force-dominated region. The kinematic conditions $\left(Q^2 = 2\ \mathrm{GeV}^2 \text{ and } x_B > 1\right)$ allow us to extract the abundance of pn- and pp-correlated pairs with minimal interference from final state interactions, meson exchange currents and resonance production. The experiment was approved for 23 PAC days to perform the measurements at four values of missing momenta.

The scientific goals for this experiment were partially achieved in terms of the data acquisition with three missing momentum values of 500, 625 and 755 MeV/c (covering an acceptance of 350-840 MeV/c). The missing momentum distributions normalized to the accumulated beam charge for the three kinematic points are shown in Fig. 41. Analysis for the experiment is proceeding, and we expect final results within the next two years.

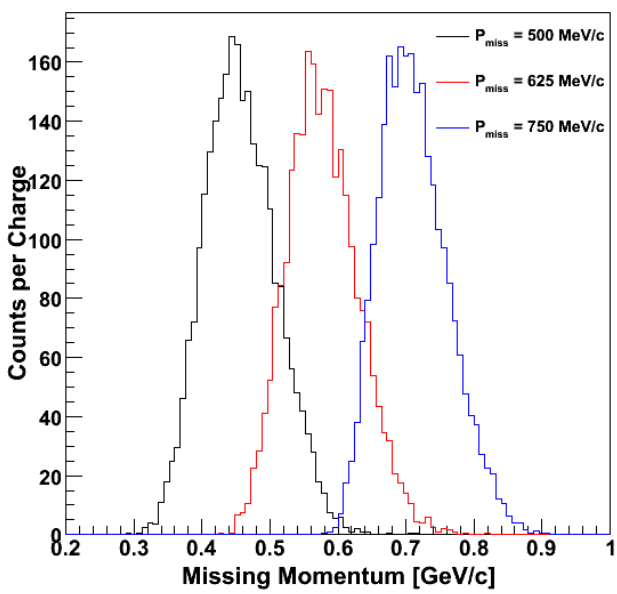

Figure 41: Missing momentum distributions for values of 500, 625 and 755 MeV/c normalized to charge.

At this point, the analysis is focused on three main direction. One focus of the analysis is to study the triple coincidence reactions: $^{4}\mathrm{He}(\mathrm{e},\mathrm{e}'\mathrm{pn})$ and $^{4}\mathrm{He}(\mathrm{e},\mathrm{e}'\mathrm{pp})$, determine the number of events for each of the reactions and calculate their cross section ratio. As the missing mass increases, the dominance of the tensor force is expected to be reduced and the short range repulsive force is expected to be more important. The ratio of the two different isospin channels can hopefully teach us about the interplay between these components of the short distance nucleon-nucleon force.

Another focus of the analysis is to examine the possibility of detecting SRCs using double coincidence measurements. We are in the process of analyzing events where the scattered electron is detected in the left HRS and the recoil partner (a proton or a neutron) is detected in coincidence in either the Hall A Neutron Detector (HAND) or the BigBite spectrometer. The advantage of this analysis is that if we can identify the events corresponding to SRCs, then their statistics will be much improved compared to that of the triple coincidence events. Success in this analysis will also pave the way to use recoil high momentum nucleons as a trigger for DIS from correlated pairs [2].

The last analysis direction is an effort to use the new high precision $^4\mathrm{He}(\mathrm{e},\mathrm{e}'\mathrm{p})$ data at high missing momentum together with measurements of the same reaction with lower missing momentum [3] to check the theoretical calculations of the ^{4}He nuclei. The high momentum part is a great theoretical challenge due to the importance of relativistic effects.

References

[1] S. Gilad, D. Higinbotham, E. Piasetzky, V. Sulkosky and J. Watson (spokespersons) JLab experiment E07-006 (2007).

[2] S. Gilad, O. Hen, L. Weinstein and S. A. Wood (spokespersons) JLab experiment E12-11-107 (2011).

[3] K. Aniol, F. Benmokhtar, S. Gilad, D. Higinbotham and A. Saha (spokespersons) JLab experiment E08-009 (2008).

3.11 E07-013 - A_y in DIS ^{3}He(e,e')

A Measurement of the Target Normal Single-Spin Asymmetry in Inclusive DIS Scattering

Todd Averett, Tim Holmstrom, and Xiaodong Jiang (spokespersons)
and the Hall A Collaboration.

contributed by Joseph Katich and Xin Qian

The Experiment

Experiment E07-013 has measured the target single-spin asymmetry (SSA) in inclusive DIS scattering of electrons from a vertically polarized ^{3}He target. The reaction channel is a clean window into the realm of two-photon exchange (2γ) physics, as the asymmetry is identically zero in the Born approximation. A non-zero asymmetry is a clear indication of a 2γ effect. The experiment ran parasitically to E06-010 ('Transversity') from late October 2008 until early February of 2009, during which more than 16 coulombs of good vertical-target production data were acquired. The experiment also made use of data collected from a transversely polarized target. This transverse data serves as a systematic check, as its the single-spin asymmetry is expected to be identically zero.

^{3}He Target

For the experiment, the recently developed 'hybrid' ^{3}He cells were implemented; the second experiment to do so. This modification to the target allows for in beam target polarization to reach nearly 50%. Further, the usual FAP Coherent lasers were replaced with narrow-band lasers that better match the absorption spectrum of Rubidium. This is the first experiment to use these lasers with the ^{3}He setup, and the result was another increase of in-beam polarization, averaging better than 60% (absolute).

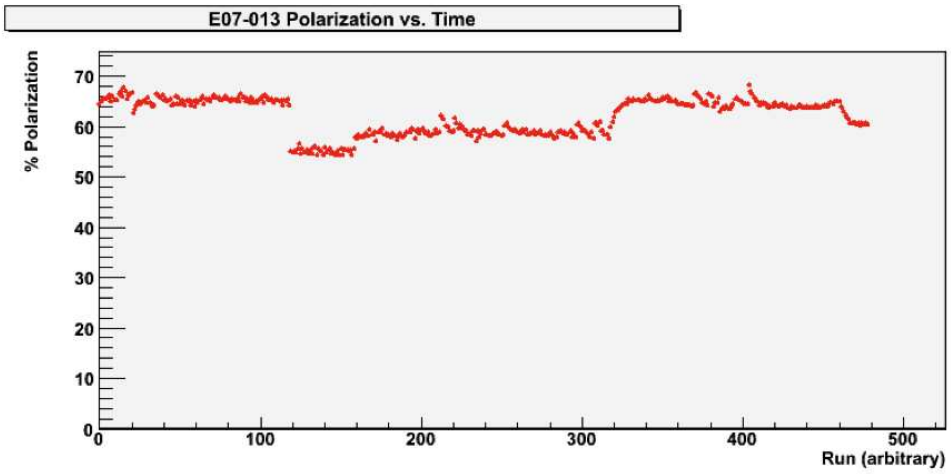

Figure 42: ^{3}He target performance for vertical production data runs (plotted versus arbitrary run numbers).

The experiment also took advantage of a highly modified ^{3}He oven and laser setup that was designed to provide target polarization along any of X,Y or Z axes. This new feature allowed not only for the vertical (out of scattering plane) target polarization that is needed to maximize the 2γ signal, but also the transverse (in-plane) polarization for a systematic check.

Analysis Progress

The biggest challenge regarding data analysis is the separation of 'good' electrons from background in the BigBite detector for the three individual triggers with good singles data: T1 (Preshower+Shower sum), T2 (Preshower, Shower and a gas Cerenkov) and T6 (identical to T1, but with a higher Preshower threshold). By far the largest source of background comes from photon-induced electron-positron pairs. There is also a small amount of negative pion contamination. Estimation of the negative pion contamination is straightforward and is achieved by fitting the preshower energy deposition for electrons and negative pions. These numbers are also compared with the BigBite GEANT3 Monte Carlo,and were found to be in good agreement. Pair-produced contamination is estimated by applying positron cuts to positive-polarity BigBite runs, then comparing this yield to that of a normal production run. This process is complicated by positive hadron contamination in the positron sample. Estimates of each of these contaminations are shown below for six data bins.

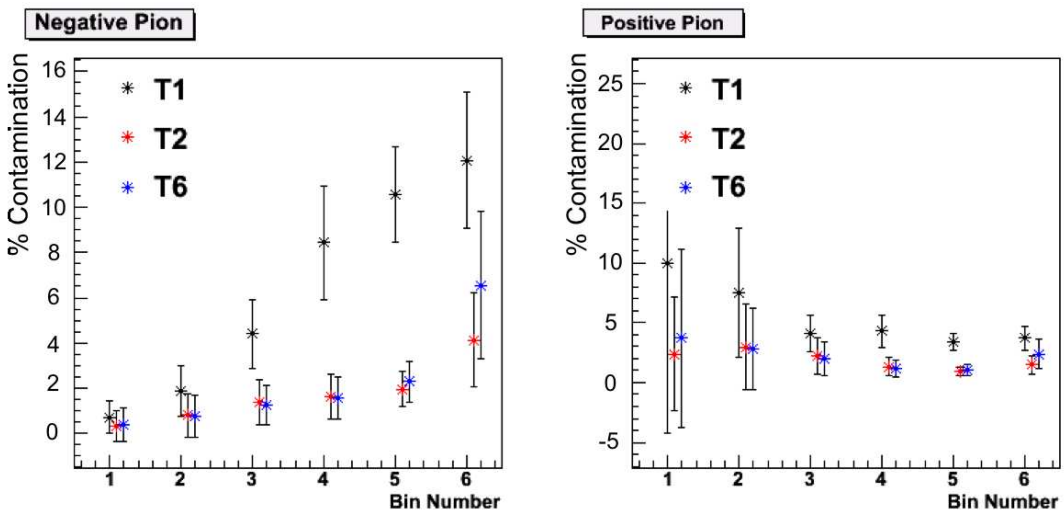

Figure 43: Contamination estimates of π^- (from negative polarity runs) and π^+ (from positive polarity runs) for six data bins.

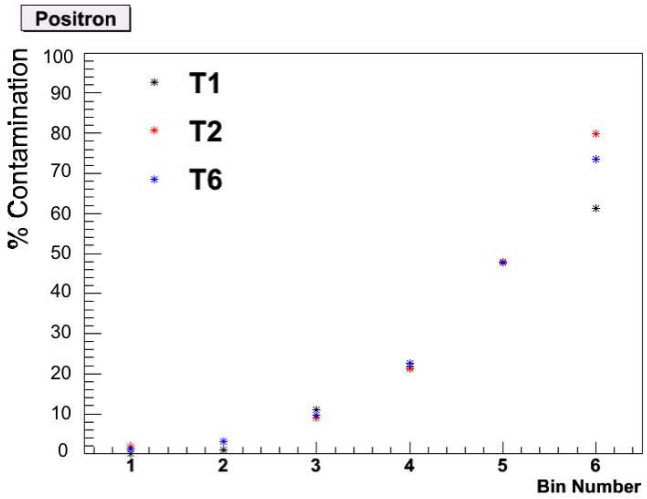

Figure 44: Photo-induced positron contamination for six data bins. Only the central values are shown. Error bars are still to come, see 'Remaining Tasks'.

Preliminary Results

Preliminary raw asymmetries are plotted below for six W bins. BigBite data is shown in black, with bins of $0 < W_1 < 2.0 < W_2 < 2.3 < W_3 < 2.6 < W_4 < 2.8 < W_5 < 3.0$. The LHRS data was analyzed as a single point and is shown in red. All data have been corrected for both pion and pair-production contamination, however, other dilution factors are yet to be taken into account for. Asymmetries at low W are consistent with the preliminary quasi-elastic A_y results. The intermediate W asymmetries show a clear positive signal at the 3σ level. The high W results favor a positive asymmetry, but with a very large systematic uncertainty. The single LHRS data point is in agreement with the trend of the BigBite data. The results have been generated by two independent analyses using completely different code, and are in very good agreement.

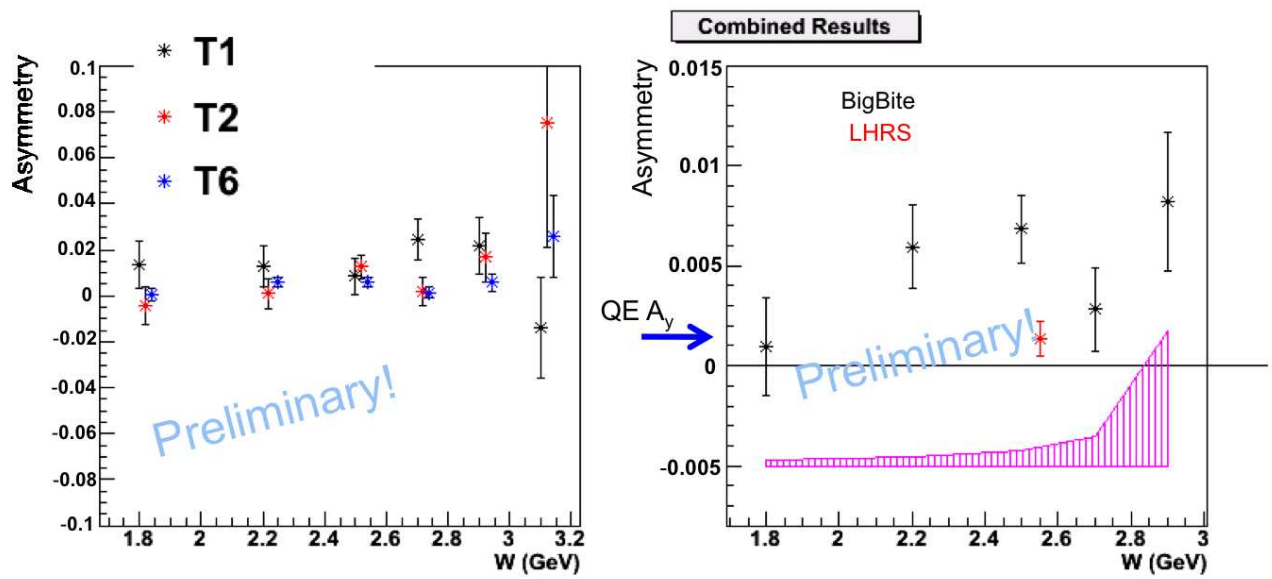

Figure 45: A_y^{raw} on ^{3}He for six W bins. Contamination corrections are applied; N_2 dilution is not. The red band on the right side plot corresponds to the BigBite systematic uncertainties.

Remaining Tasks

A few tasks remain before publication. First a correction for Nitrogen dilution (from the ^{3}He target) must be applied. The data must also be corrected for proton dilution if we are to show A_y^n rather than $A_y^{^3He}$. Radiative corrections are also to be considered. This study will primarily be concerned with leakage from the quasi-elastic tail. Finally, the systematic uncertainties budget must be finalized. Generating reliable estimates for most systematics will be straightforward, as they will be very similar to the E06-010 systematics (already published). However, there are a few challenges, such as minimizing the error bars on the pair-produced background.

3.12 E08-005 - A_y in ^{3}He(e,e'n)

T. Averett, D. Higinbotham, V. Sulkosky, spokespersons,
and
the Hall A Collaboration.
contributed by E. Long (Kent State University).

3.12.1 Progress of ^{3}He$^\uparrow(e,e'n)$ Target Single-Spin Asymmetries

Progress has been made on the ^{3}He$^\uparrow(e,e'n)$ Single-Spin Asymmetries for experiment E08-005, Measurement of the Target Single-Spin Asymmetry A_y in the Quasi-Elastic ^{3}He$^\uparrow$(e,e'n) Reaction where the target was polarized in the vertical direction (transverse to both the beam and the q-vector). The A_y observable is correlated to final state interactions (FSI) and meson exchange currents (MEC). At low Q^2, contributions from FSI and MEC are expected to be large and decrease at higher Q^2.

Data from the HRS were used to isolate the quasi-elastic peak and apply basic kinematic cuts, as shown in Figure 46 for Q^2=1.0 GeV^2, were applied to identify scattered electrons. Figures 47-50 show the Hall A Neutron Detector's time of flight (ToF) spectra. For the ToF spectra, the left plot of each set is for target spin up events and the right is for target spin down events. Figure 47 shows the background fit, which is then removed from the ToF as shown in Figure 48. This was repeated for each Q^2. From the ToF spectra, it is obvious that the asymmetry is changing with Q^2. This process will then be applied to the E05-102 experiment so that the longitudinal and Transverse $^3\vec{\text{He}}(\vec{e},e'n)$ Double-Spin Asymmetries at Q^2=0.5 and 1.0 GeV^2 can be measured.

The Q^2=0.1 GeV^2 point includes both protons and neutrons in the ToF peak. It is expected that protons dilute the asymmetry, and it will become larger when they are removed. Proton dilution for this Q^2 is in progress. For the higher Q^2, a veto on charged particles is included, which restricts the sample to neutral particles.

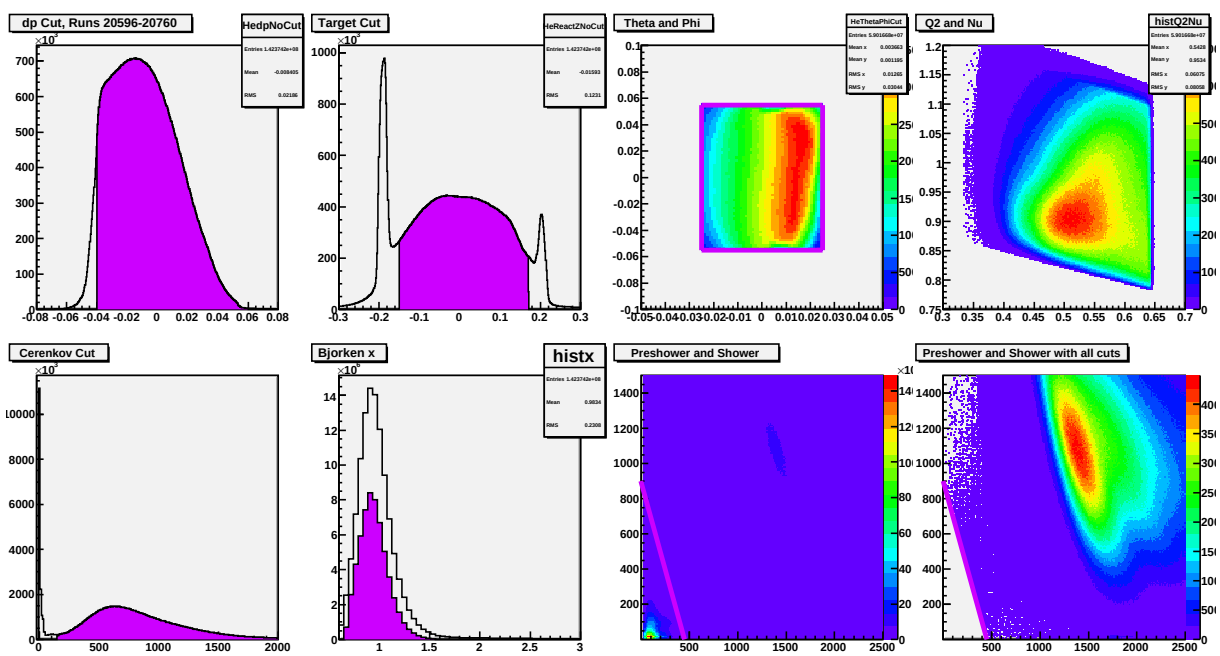

Figure 46: Basic kinematic cuts for Q^2=1.0 GeV^2. The magenta and boxed events show which electrons were selected for analysis. Similar cuts were made for the other Q^2 points.

Figure 47: ToF for Q^2=1.0 $(GeV/c)^2$ with vetoes. The plot on the left shows the ToF spectra with a background fit for spin up events and the plot on the right shows the ToF spectra with spin down events.

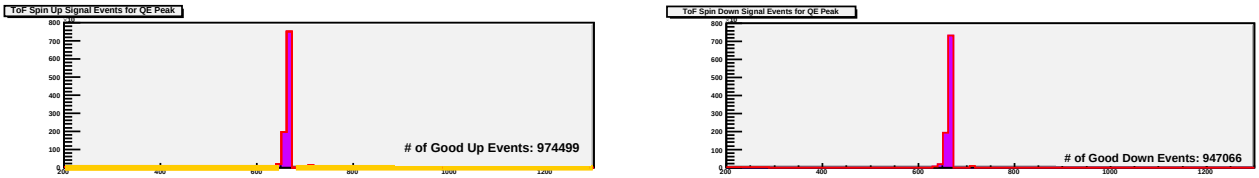

Figure 48: ToF for Q^2=1.0 GeV^2 with vetoes with background subtracted. These plots show the ToF spectra with the background subtracted. The peak is then integrated over and the number of events in the peak is displayed.

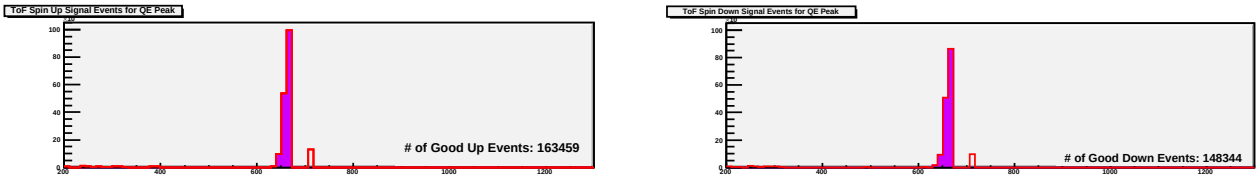

Figure 49: ToF for Q^2=0.5 GeV^2 with vetoes with background subtracted. These plots show the ToF spectra with the background subtracted. The peak is then integrated over and the number of events in the peak is displayed.

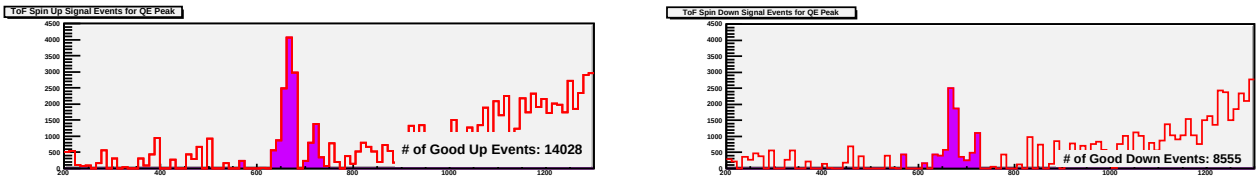

Figure 50: ToF for Q^2=0.1 GeV^2 without vetoes with background subtracted. These plots show the ToF spectra with the background subtracted. The peak is then integrated over and the number of events in the peak is displayed.

3.13 E08-009 - ^{4}He

Study of ^{4}He(e, e′p) reaction up to high missing Energies and Momenta.

K. Aniol, F. Benmokhtar, D. Higinbotham, S. Gilad and A.Saha (Spokesperson)
S. Iqbal and N. McMahon (Students)
the Hall A Collaboration.
contributed by F. Benmokhtar.

3.13.1 Motivation

Semi-inclusive $(e,e'p)$ experiments have provided a wealth of information on the effective nucleon momentum distributions, Final State Interactions (FSI) and wave function correlations. The E08-009 experiment was designed to study the ^{4}He nucleus via the reaction dynamics of the $(e,e^{'}p)$ process up to high missing energies and high missing momenta. The measurement of the cross section of two body break-up channel ^{4}He$(e,e^{'}p)$T allows the study of the triton ground state wave function, while the measurements of the continuum channel is one way to study the proton-neutron correlations.

By measuring the scattered electron and the knocked-out proton in coincidence one can increase the sensitivity to the interaction of two nucleons with small inter-nucleon separation inside a nucleus. For example, consider an electron scattering on a proton belonging to a pair of correlated nucleons inside a nucleus, ^{4}He in our case. In the center of mass system of the two nucleons, due to their closeness, these nucleons have large, equal and opposite momenta. As a first approximation we can neglect the momentum of the pair relative to the remaining nucleon. In PWIA, the struck proton is ejected with momentum $\vec{q}-\vec{p}_r$, while the other nucleon of the pair moves off with the recoil momentum of the reaction, p_r. The spectator nucleons are at rest, so this is the three-body breakup (3bbu) reaction channel, as opposed to the two-body breakup (2bbu) channel with a pT final state.

The spectator nucleons and the undetected nucleon of the pair constitute a recoil system of mass:

$$M_r^2 = [M_{A-2} + \sqrt{M_N^2 + p_r^2}]^2 - p_r^2 \tag{22}$$

Thus, the signature of this process is the appearance of a peak in E_{miss} in the continuum region whose position depends on p_r: $E_{miss} = M_r + M_p - M_A$. The peak width reflects the motion of the center of mass with respect to the spectator nucleons and its height is directly related to the relative wave function of the two nucleons. The peak thus signifies the absorption of virtual photons on nucleons correlated in pairs.

The integral over the continuum will give the momentum distribution of the proton in the pair. It is obtained experimentally by dividing the experimental cross section by the elementary off-shell electron-proton cross section σ_{ep}, and by integrating over missing energy:

$$\eta(p_{miss}) = \int \left(\frac{d^6\sigma}{dE_f dE_p d\Omega_e d\Omega_p} / \sigma_{ep} \right) \, dE_{miss} \tag{23}$$

This momentum density distribution is an actual density only in the PWIA limit. What one gets experimentally is the distorted momentum density distribution.

3.13.2 The experiment

The E08009 experiment ran its perpendicular kinematics during the spring of 2011 concurrently with a series of Short Range Correlation (SRC) experiments for high missing momenta up to 1 GeV/c and ran with its dedicated beam time at low missing momenta down to 150 MeV/c. The continuum region of the ^{4}He$(\mathrm{e},\mathrm{e}'\mathrm{p})$ reaction is under study in order to investigate high-nucleon-momenta components in the ^{4}He wave function with the absorption of virtual photons on proton-neutron correlated in pairs in the ^{4}He ground state.

The measurements were performed at $x_B = 1.25$ and at a fixed transferred four-momentum $Q^2 = 2(GeV/c)^2$. These measurements will complement a previous experimental study of the same reaction on ^{3}He carried in Hall A of Jefferson Lab, which was the thesis subject of Fatiha Benmokhtar and Marat Rvachev [1, 2].
Comparison of the distorted density distributions of the continuum channels of ^4He and ^3He might show a scaling behavior between the two reaction, since in the case of ^3He, the proton couples to the only neutron of the nucleus, while in ^4He it has the possibility to couple to any of the two neutrons.

3.13.3 Status of the Analysis

Two students Sophia Iqbal; a master student from California State University Los Angeles. and Nicholas McMahon; a summer student from Christopher Newport University, worked on some aspects of the analysis of the experiment. Data quality check, acceptance study and background subtraction are all done.

Target density was extracted for both temperatures of 18 K and 20 K and our study showed that one has to apply a 2% adjustments due to the virial corrections for the lower temperature. These corrections count for the deviation of the density from an ideal gas model by taking into account the change in the surface pressure when the temperature is changing. Our study also showed that these corrections stay the same with the changes in target pressure during the experiment and just depend on the Temperature.

Figure 51 shows samples of missing energy spectra for different missing momenta. These spectra are corrected from outside spectrometer coincidence events, fortuitous coincidences as well target wall contributions. at lower missing momenta the contribution is dominated by the two body breakup channel, while going to higher missing momenta the continuum is predominant. We can also see the motion of the position of the continuum bump to higher missing energies when going higher in missing momentum. See here as well is the show-up of the bump of the pion electroproduction after missing energy values corresponding to the pion mass at 140 MeV.

Theoretical calculations are underway by Udias' group and we got a big interest from other theorists who are interested on doing the calculations for us.

References

[1] F. Benmokhtar *et al.*, Phys. Rev. Lett **94** ,082305 (2005).

[2] M. M. Rvachev *et al.*, Phys. Rev. Lett **94** ,192302 (2005).

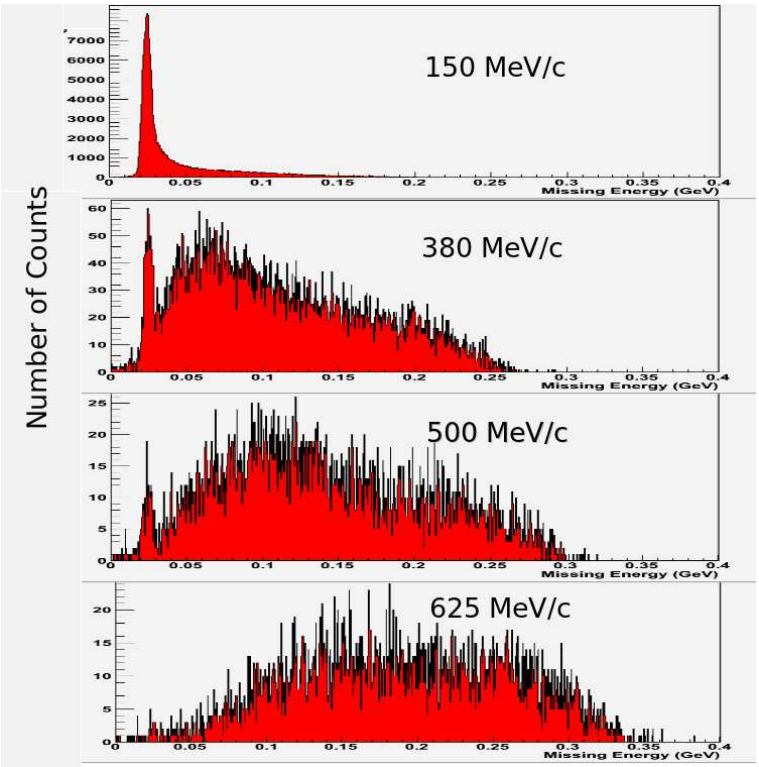

Figure 51: Sample of Missing Energy spectra for different values of Missing Momenta for the $^4\mathrm{He}(\mathrm{e},\mathrm{e}'\mathrm{p})\mathrm{X}$ reaction. Work done by N. McMahon, Christopher Newport University student. This spectra are acceptance corrected and cleaned from accidental coincidences.

3.14 E08-010 - N - Δ

Measurement of the Coulomb quadrupole amplitude at the $\gamma^* p \to \Delta(1232)$ in the low momentum transfer region

S. Gilad, D. W. Higinbotham, A. Sarty and N. F. Sparveris, spokespersons,
and
the Hall A Collaboration.
contributed by N.F. Sparveris

3.14.1 Introduction

The complex quark-gluon and meson cloud dynamics of hadrons give rise to non-spherical components in their wavefunction which in a classical limit and at large wavelengths will correspond to a "deformation". Understanding the origin of possible non-spherical components in the nucleon wavefunction has been the subject of an extensive experimental and theoretical effort in recent years [1, 2, 3, 4, 5, 6, 7, 8, 9, 10, 11, 12, 13, 14, 15, 16, 17, 18, 19, 20, 21, 22, 23, 24, 25, 26, 27, 28]. The spectroscopic quadrupole moment provides the most reliable and interpretable measurement of the presence of these components; for the proton, the only stable hadron, it vanishes identically because of its spin 1/2 nature. As a result, the presence of resonant quadrupole amplitudes in the $N \to \Delta$ transition has emerged as the definitive experimental signature of these components. Spin-parity selection rules in the $\gamma^* N \to \Delta$ transition allow only magnetic dipole (M1) and electric quadrupole (E2) or Coulomb quadrupole (C2) photon absorption multipoles (or the corresponding pion production multipoles $M_{1+}^{3/2}, E_{1+}^{3/2}$ and $S_{1+}^{3/2}$ ($L_{1+}^{3/2}$) respectively) to contribute. The ratios CMR $= Re(S_{1+}^{3/2}/M_{1+}^{3/2})$ and EMR $= Re(E_{1+}^{3/2}/M_{1+}^{3/2})$ are routinely used to present the relative magnitude of the amplitudes of interest. Non-vanishing resonant quadrupole amplitudes will signify the presence of non-spherical components in either the proton or in the $\Delta^+(1232)$, or more likely at both; moreover, their Q^2 evolution is expected to provide insight into the mechanism that generate them.

The origin of these components is attributed to a number of different processes depending on the interpretative framework adopted. In the quark model, the nonspherical amplitudes in the nucleon and Δ are caused by the noncentral, tensor interaction between quarks [29]. However, the effect for the predicted E2 and C2 amplitudes [2] is at least an order of magnitude too small to explain the experimental results, and even the dominant M1 matrix element is $\approx 30\%$ low [2]. A likely cause of these dynamical shortcomings is that the quark model does not respect chiral symmetry, whose spontaneous breaking leads to strong emission of virtual pions (Nambu-Goldstone bosons) [28]. These couple to nucleons as $\vec{\sigma} \cdot \vec{p}$, where $\vec{\sigma}$ is the nucleon spin, and $\vec{p}$ is the pion momentum. The coupling is strong in the p-wave and mixes in nonzero angular-momentum components. Based on this, it is physically reasonable to expect that the pionic contributions increase the M1 and dominate the E2 and C2 transition matrix elements in the low-Q^2 (large distance) domain. This was first indicated by adding pionic effects to quark models [30], subsequently shown in pion cloud model calculations [21, 23], and recently demonstrated in chiral effective field theory calculations [27, 31]. Our current understanding of the nucleon suggests that at low-Q^2 (large distance) the pionic cloud effect dominates while at high-Q^2 (short distance) intra-quark forces dominate. Recent precise experimental results [3, 4, 5, 6, 7, 8, 9, 10, 11, 12, 13, 15, 16, 17, 18, 19] are in reasonable agreement with predictions of models suggesting the presence of non-spherical components and in strong disagreement with all nucleon models that assume sphericity for the proton and the Δ. With the existence of these components well established, recent investigations have focused on understanding the various mechanisms that could generate them.

Dynamical reaction models with pion cloud effects [21], [22] bridge the constituent quark models gap and are in qualitative agreement with the Q^2 evolution of the data. The models calculate the resonant channels from dynamical equations; they calculate the virtual pion cloud contribution dynamically but have an empirical parameterization of the inner (quark) core contribution which gives them some flexibility in the observables. They find that a large fraction of the quadrupole multipole strength arises due to the pionic cloud with the effect reaching a maximum value in the region $Q^2 = 0.10\ (GeV/c)^2$ (see Fig. 52). Results from effective field theoretical (chiral) calculations [27, 31], solidly based on QCD, can also successfully account for the magnitude of the effects giving further credence to the dominance of the

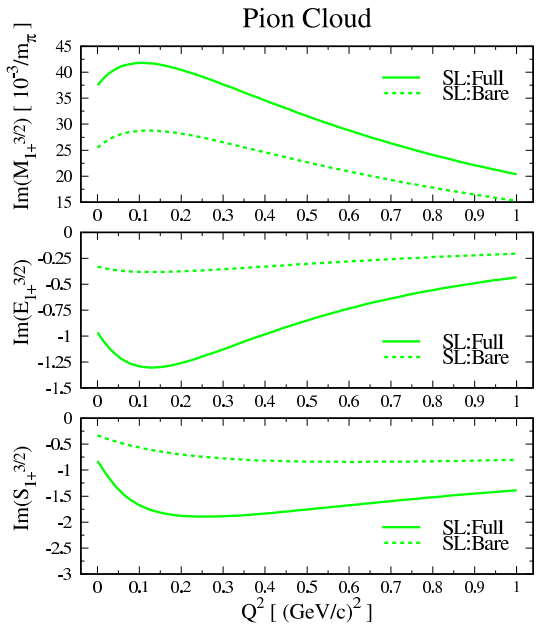

Figure 52: The effect of the pionic cloud to the resonant amplitudes as predicted by the Sato-Lee calculation [21]. Solid line includes the pion cloud contribution while the dashed line neglects the pion cloud effect.

meson cloud effect in the low Q^2 region. Recent results from lattice QCD [20] are also of special interest since they are for the first time accurate enough to allow a comparison to experiment. The chirally extrapolated [27] values of CMR and EMR are found to be nonzero and negative in the low Q^2 region, in qualitative agreement with the experimental results, thus linking the experimental evidence for the nonspherical amplitudes directly to QCD while highlighting the importance of future lattice calculations using lighter quark masses and further refining the chiral extrapolation procedure.

3.14.2 The Experiment

The E08-010 experiment aim to explore the low momentum transfer region at the nucleon - $\Delta(1232)$ transition, where the pionic cloud effects are expected to dominate. The experiment ran in February and March of 2011 and achieved all the quantitative and qualitative goals of the experiment proposal. High precision measurements of the $p(e,e'p)\pi^\circ$ excitation channel were provided. The two High Resolution Spectrometers (HRS) were utilized to detect in coincidence electrons and protons respectively while the 6 cm and 15 cm liquid hydrogen targets and an electron beam of $E_o =$ 1.15 GeV at 75 μA were used throughout the experiment. High precision measurements were conducted in the $Q^2 = 0.04$ $(GeV/c)^2$ to 0.13 $(GeV/c)^2$ range. The experiment will offer results of unprecedented precision in the low momentum transfer region, it will extend the knowledge of the Coulomb quadrupole amplitude lower in momentum transfer, and will resolve discrepancies between measurements of other labs. The analysis of the data is currently at a preliminary stage. The projected uncertainties for the CMR are presented in Fig. 53. The results will allow to identify the various mechanisms responsible for the presence of non-spherical components in the nucleon wavefunction, will provide a precise signature of the pion cloud, offer a deeper understanding of the interplay of the quark-gluon and mesonic degrees of freedom inside the nucleon, and will provide strong constraints to the modern theoretical calculations leading to a more complete understanding of the nucleon dynamics.

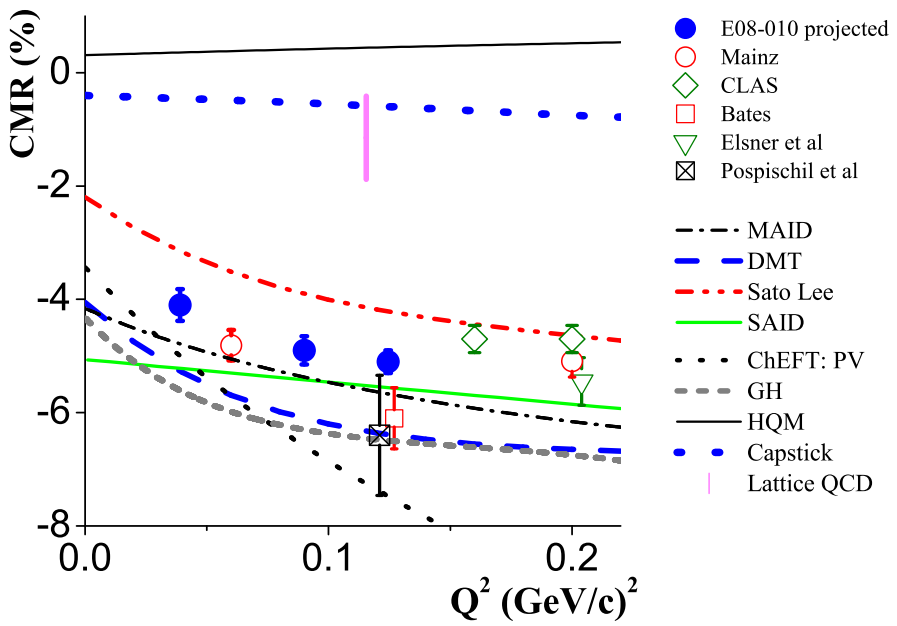

Figure 53: The CMR at the low momentum transfer region. The projected E08-010 uncertainties are presented along with the world data and the theoretical model predictions

References

[1] A. de Rujula, H. Georgi and S.L. Glashow *et al.*, Phys. Rev **D12**, 147 (1975).

[2] N. Isgur, G. Karl and R. Koniuk, *Phys. Rev.* **D25**, 2394 (1982); S. Capstick and G. Karl, *Phys. Rev.* **D41**, 2767 (1990).

[3] G. Blanpied *et al.*, Phys. Rev. Lett. **79**, 4337 (1997).

[4] R. Beck *et al.*, Phys. Rev. Lett. **78**, 606 (1997);
ibid. 79, 4515 (1997) (Erratum).
R. Beck *et al.*, Phys. Rev. **C61**, 35204 (2000).

[5] V.V. Frolov *et al.*, Phys. Rev. Lett. **82**, 45 (1999).

[6] T. Pospischil *et al.*, Phys. Rev. Lett. **86**, 2959 (2001).

[7] C. Mertz *et al.*, Phys. Rev. Lett. **86**, 2963 (2001).

[8] P. Bartsch *et al.*, Phys. Rev. Lett. **88**, 142001 (2002).

[9] L.D. van Buuren *et al.*, Phys. Rev. Lett. **89**, 12001 (2002).

[10] N.F. Sparveris *et al.*, Phys. Rev. Lett. **94**, 022003 (2005).

[11] J.J. Kelly *et al.*, Phys. Rev. Lett. **95**, 102001 (2005).

[12] N.F. Sparveris *et al.*, Phys. Lett. **B 651**, 102 (2007).

[13] S. Stave *et al.*, Eur. Phys. J. **A 30**, 471 (2006).

[14] D. Elsner *et al.*, Eur. Phys. J. **A 27** 91-97 (2006).

[15] K. Joo *et al.*, Phys. Rev. **C68**, 032201 (2003); K. Joo *et al.*, Phys. Rev. **C70**, 042201 (2004)

[16] S. Stave, N. Sparveris *et al.*, Physical Review **C78**, 025209 (2008)

[17] M. Ungaro *et al.*, Phys. Rev. Lett. **97**, 112003 (2006).

[18] A. N. Villano *et al.*, Phys. Rev. C 80, 035203 (2009)

[19] I.G. Aznauryan *et al.* Phys. Rev. C 80, 055203 (2009)

[20] C. Alexandrou *et al.*, Phys. Rev **D83** 014501 (2011); Phys. Rev. Lett. **94**, 021601 (2005).

[21] T. Sato and T.-S.H. Lee, Phys. Rev. **C63**, 055201 (2001).

[22] S.S. Kamalov and S. Yang, Phys. Rev. Lett. **83**, 4494 (1999)

[23] S.S. Kamalov *et al.*, Phys. Lett. **B 522**, 27 (2001).

[24] D. Drechsel *et al.*, Nucl. Phys. **A 645**, 145 (1999).

[25] D. Drechsel and L. Tiator, J. Phys. **G18**, 449 (1992)

[26] R.A. Arndt, *et al.* Phys. Rev. **C66**, 055213 (2002); nucl-th/0301068 and http://gwdac.phys.gwu.edu

[27] V. Pascalutsa and M. Vanderhaegen *et al.*, Phys. Rev. Lett. **95**, 232001 (2005) and V. Pascalutsa and M. Vanderhaegen *et al.*, Phys. Rev. **D73**, 034003 (2006).

[28] A.M. Bernstein, Eur. Phys. J. **A 17**, 349 (2003).

[29] S.L. Glashow, Physica A **96**, 27 (1979)

[30] D.H. Lu, A.W. Thomas, A.G. Williams, Phys. Rev. **C55**, 3108 (1997); U. Meyer, E. Hernandez, A.J. Buchmann, Phys. Rev. **C64**, 035203 (2001); M. Fiolhais, B. Golli, S. Sirca, Phys. Lett. **B 373**, 229 (1996)

[31] T. A. Gail and T. R. Hemmert, Eur. Phys. J. **A 28** (1), 91-105 (2006)

3.15 E08-011 - PVDIS

$\vec{e}-^2$H Parity Violating Deep Inelastic Scattering (PVDIS) at CEBAF 6 GeV

R. Michaels, P.E. Reimer, X. Zheng, spokespersons,
K. Pan, D. Wang, PhD students,
and
the Hall A Collaboration.
contributed by X. Zheng

The parity violating asymmetry of $\vec{e}-^2$H deep inelastic scattering (PVDIS) was measured more than thirty years ago at SLAC [1, 2], and was the first experiment that established the value of the Standard Model weak mixing angle $\sin^2\theta_W$. The goal of E08-011 is to provide an up-to-date measurement on the $\vec{e}-^2$H PVDIS asymmetry. This will not only improve the world knowledge on the electron and the quark neutral weak couplings, but also serve as an exploratory step for the future PVDIS program at the 12 GeV Upgrade.

The PV asymmetry of electron deep inelastic scattering (DIS) off a nuclear target is

$$\begin{aligned} A_{PV}^{DIS} &= -\frac{G_F Q^2}{4\sqrt{2}\pi\alpha}\left[2g_A^e Y_1(y)\frac{F_1^{\gamma Z}}{F_1^Z} + g_V^e Y_3(y)\frac{F_3^{\gamma Z}}{F_1^Z}\right] \\ &= -\frac{G_F Q^2}{4\sqrt{2}\pi\alpha}\left[a_1(x)Y_1(y) + a_3(x)Y_3(y)\right] \end{aligned} \tag{24}$$

where G_F is the Fermi constant, α is the fine structure constant, x is the Bjorken scaling variable, $y = \nu/E$ is the fractional energy loss of the electron with E the incident electron energy. With $r^2 = 1 + \frac{Q^2}{\nu^2}$ and $R^{\gamma,\gamma Z}$ the ratio of the longitudinal and transverse virtual photon electromagnetic absorption and the $\gamma - Z^0$ interference cross sections, respectively:

$$Y_1 = \left[\frac{1+R^{\gamma Z}}{1+R^{\gamma}}\right]\frac{1+(1-y)^2 - y^2\left[1-\frac{r^2}{1+R^{\gamma Z}}\right] - xy\frac{M}{E}}{1+(1-y)^2 - y^2\left[1-\frac{r^2}{1+R^{\gamma}}\right] - xy\frac{M}{E}} \tag{25}$$

and

$$Y_3 = \left[\frac{r^2}{1+R^{\gamma}}\right]\frac{1+(1-y)^2}{1+(1-y)^2 - y^2\left[1-\frac{r^2}{1+R^{\gamma}}\right] - xy\frac{M}{E}} \ . \tag{26}$$

In the quark parton model,

$$a_1(x) = 2g_A^e\frac{F_1^{\gamma Z}}{F_1^Z} = 2\frac{\sum C_{1i}Q_i q_i^+(x)}{\sum Q_i^2 q_i^+(x)} \quad \text{and} \quad a_3(x) = g_V^e\frac{F_3^{\gamma Z}}{F_1^Z} = 2\frac{\sum C_{2i}Q_i q_i^-(x)}{\sum Q_i^2 q_i^+(x)} \ , \tag{27}$$

where the summation is over the quark flavor $i = u, d, s\cdots$, Q_i is the corresponding quark electric charge, $q_i^{\pm}(x)$ are defined from the PDF $q_i(x)$ and $\bar{q}_i(x)$ as $q_i^+(x) \equiv q_i(x) + \bar{q}_i(x)$ and $q_i^-(x) \equiv q_{i,V}(x) = q_i(x) + \bar{q}_i(x)$. For an isoscalar target such as the deuteron, the functions $a_{1,3}(x)$ simplify to

$$a_1(x) = \frac{6\left[2C_{1u}(1+R_c) - C_{1d}(1+R_s)\right]}{5+R_s+4R_c} \quad \text{and} \quad a_3(x) = \frac{6\left(2C_{2u} - C_{2d}\right)R_v}{5+R_s+4R_c} \ . \tag{28}$$

Neglecting effects from heavier quark flavors and assuming that $u^p = d^n$, $d^p = u^n$ [$u, d^{p(n)}$ are the up and down quark PDF in the proton (neutron)], $s = \bar{s}$, and $c = \bar{c}$, the PDF's give

$$R_c \equiv \frac{2(c+\bar{c})}{u+\bar{u}+d+\bar{d}}, \ R_s \equiv \frac{2(s+\bar{s})}{u+\bar{u}+d+\bar{d}}, \text{ and } R_V \equiv \frac{u-\bar{u}+d-\bar{d}}{u+\bar{u}+d+\bar{d}}. \tag{29}$$

For E08-011, the central setting of the spectrometer was $Q^2 = 1.121$ and 1.925 (GeV/c)^2, comparable to the SLAC experiment. At $Q^2 = 1.925$ (GeV/c)^2, the asymmetry was measured to a $\approx 4\%$ (stat.) level. Not including the uncertainty from non-perturbative hadronic effects, the electron and quark neutral weak coupling constant combination, $2C_{2u} - C_{2d} \equiv 2g_V^e g_A^u - g_V^e g_A^d$, can be extracted from this result. The asymmetry at $Q^2 = 1.121$ (GeV/c)^2 was measured to a 3% level (stat.), and will set a constraint on the higher twist effect.

E08-011 ran from late October to end of December 2009. We utilized the two HRSs for detecting the scattered electrons in the inclusive mode. Because the expected asymmetries as well as their statistical uncertainties are larger by 1-2 orders of magnitude than other parity experiments of the same period (HAPPEX-III and PREX), control of beam-related systematic uncertainties which was the major challenge to these parity experiments, is less of a concern for PVDIS. In contrast, because of the high pion background typical to DIS measurements, the integration method could not be used for this experiment. Instead a specially-designed, fast counting DAQ was used and a major part of the analysis effort in the past two years was devoted to understanding the DAQ performance. In the following we will present the analysis status of the experiment.

The polarization of the electron beam was measured by the Møller polarimetry intermittently during the experiment, with an average value of $P_b = [88.47 \pm 0.047(stat.) \pm 1.8(syst.)]\%$. The uncertainty was dominated by the knowledge of the Møller target polarization. The Compton polarimeter monitored the polarization throughout the experiment and found $P_b = [90.18 \pm 1.8(syst.)]\%$. The uncertainty of the Compton measurement came primarily from the limit in understanding the shielding used to reduce the background events.

The target was a 20-cm long liquid deuterium cell with two 5 mil aluminum windows. The helicity-correlated density fluctuation was monitored by the luminosity monitor. Assuming a $\pm 10\%$ difference in the PVDIS asymmetry between aluminum and deuterium, the correction to the measured deuteron asymmetry is 0.2% for both Q^2 results.

The scattered particles were detected by the Hall A High Resolution Spectrometer (HRS) pair at two scattering angles of 12.9° and 20.0°. A CO_2 gas Čerenkov detector and a double-layered lead-glass shower counter were used to separate electrons from the pion background. Dedicated measurements on a carbon multi-foil target were performed to determine the uncertainty of the scattering angle and the spectrometer momentum reconstruction. The uncertainties on the Q^2 were determined from the method of the optical calibration and the instrumentation limit, and were found to be 0.725% for $Q^2 = 1.121$ and $(0.58 - 0.64)\%$ for $Q^2 = 1.925$ (GeV/c^2), respectively.

In order to count the ≈ 500 kHz electrons and reject the pion photo- and electro-production background typical for DIS, a trigger and DAQ system was specially designed for this experiment. Both electron and pion triggers were formed. For electron triggers, the overall electron efficiency is found to be $\approx 95\%$ with a $> 1000:1$ pion rejection thanks to both the lead glass and the gas cherenkov counters. The pion contamination are found to 'decrease ("dilute") the absolute value of the measured electron asymmetry by 10^{-4}.

The deadtime correction from the DAQ contributes as a major systematic uncertainty for this experiment. The deadtime of the DAQ consists of three parts: the "path" deadtime caused by summing and discriminating the preshower and shower signals to form preliminary electron and pion triggers; the "veto" deadtime caused by combining the preshower/shower triggers with the HRS T1 trigger and cherenkov signals; and the "final or" deadtime caused by taking the logical OR of 6 (8) paths to form the final electron and pion triggers for the left (right) HRS. A full scale simulation package was developed to study specifically the timing performance of the DAQ: Measured T1 and detector rates were used as inputs to the simulation, as well as the preshower and the shower ADC amplitudes from the HRS DAQ. The software then simulate the performance of each electric module in real time. In addition, each component of the deadtime is confirmed by a second method: the "path" deadtime is confirmed by data from the pre-installed "tagger" system. The "veto" deadtime is checked by both first-order calculations and data from the flash-ADCs. The "or" deadtime is checked by first-order calculations. The final deadtime correction to the electron trigger is at the 1-2% level for the two DIS kinematics, with an error bar of 20% relative depending on how well the simulated results agree with the second, cross-checking method.

Two independent asymmetry analyzes are being carried out. To avoid bias in the analysis, the electron asymmetries from DIS kinematics are blinded. All pion asymmetries are not blinded, neither are electron asymmetries in the transverse, the resonance, and the positron measurements. So far, blinded DIS electron asymmetries from the two analyzes

agree within 0.2 ppm, about 1/20 of the statistical uncertainty. The statistical quality and some preliminary results on the blinded asymmetries are shown in Figs. 54-55. The non-Gaussian tail for kinematics #1 ($Q^2 = 1.121$ (GeV/c)^2) taken on the left HRS and for #2 ($Q^2 = 1.925$ (GeV/c)^2) taken on the right HRS were due to variations in the beam current (85-105 μA) used at the beginning of the experiment. This non-Gaussian tail is not present in later data taking where a consistent 105 μA current was used, as can be seen from data on kinematics #2 collected from the left HRS.

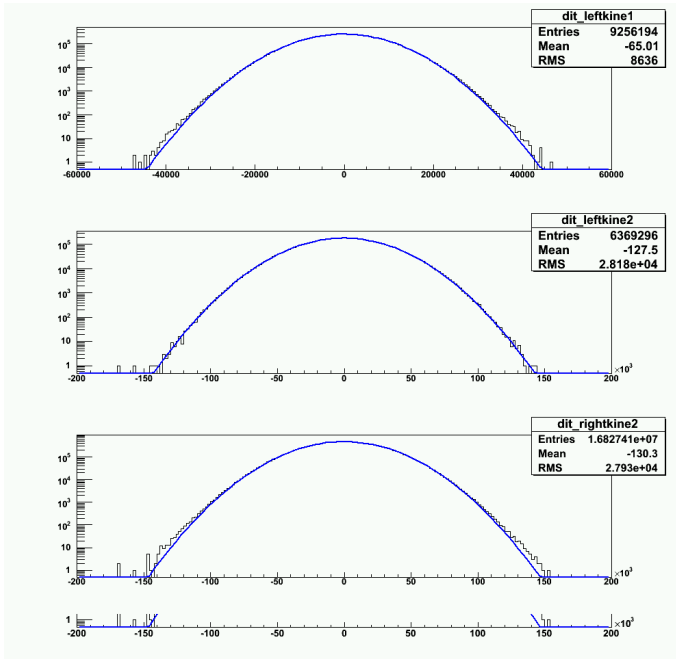

Figure 54: Overall statistical quality of the data after dithering correction. From top to bottom: kinematics #1 taken on the left HRS, kinematics #2 taken on the left HRS, and kinematics #2 taken on the right HRS. All asymmetries shown are blinded.

The transverse asymmetry were found to be 26.9 ± 15.66 ppm for $Q^2 = 1.121$ and 11.84 ± 49.89 ppm for $Q^2 = 1.925$ (GeV/c)^2, respectively, and would cause a 10^{-4} uncertainty to the measured PVDIS asymmetries.

Asymmetries of pion triggers formed from inclusive pion electro- and photo-production events are being extracted. Because the pion triggers of our DAQ used only the gas cherenkov to reject electrons, while for the lead glass detector, only a low threshold was used to reject low energy background, but no high threshold was used (to reject electrons), a high electron contamination is expected for the pion trigger. To interpret correctly the measured pion asymmetry, we must therefore understand this electron contamination first.

Effects from the pair production background were studied by reversing the polarity of the spectrometer magnet settings and were found to be at the 10^{-4} level for $Q^2 = 1.121$ GeV$/c^2$. The asymmetry of the pair production at this Q^2 was found to be 723.2 ± 1154.7 ppm, consistent with zero. False asymmetries were found to be consistent with zero from measurements of polarized beam scattering off unpolarized ^{12}C targets.

Radiative corrections were performed for both the internal and the external radiation effects. External radiative corrections were performed based on the procedure first described by Mo and Tsai [3]. Apart from elastic and quasi-elastic $e-^2$H scattering asymmetries, parity violation asymmetries of the nucleon resonances calculated from two models [4, 5] [with [4] for the $\Delta(1232)$ only] have been used, while a third set of calculation is underway [6]. Each calculation was provided to us in tabulated forms to cover the full range of E, E' and θ needed by our simulation. For kinematics that these tables do not cover but are within the resonance region ($W < 2$ GeV), we constructed "toy" models which scale the asymmetry calculated from the DIS formula by the ratio of resonance to DIS cross sections. The toy model thus has the quark-hadron duality "built-in" but may not work for the Δ region. Measurements of the

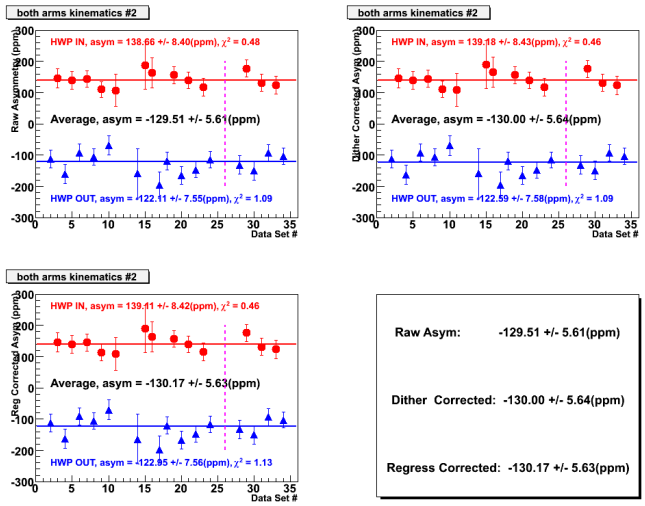

Figure 55: Preliminary results on the electron asymmetry at $Q^2 = 1.925$ (GeV$/c)^2$. All asymmetries shown are blinded.

resonance PV asymmetries were performed with a beam energy of 4.8674 GeV and provide a $\pm(10-15)\%$ precision each for the $\Delta(1232)$, the 2nd and the 3rd resonances. These are being used to check the validity of the resonance calculations and thus provide an estimate on how reliable these inputs to the radiative correction are.

So far, the raw (not corrected for the DAQ deadtime) $\Delta(1232)$ results agree with the two calculations (almost identical within the Δ region) at a ≈ 2 standard deviation level. The deadtime correction would reduce the difference, perhaps by a factor of two. Analyzes for the 2nd and the 3rd resonances are currently underway. The first preliminary results on the DIS kinematics indicate that the radiative corrections are at the 2-4% level, with an uncertainty below 0.5%.

In comparing with the asymmetry from the Standard Model, we used CTEQ6 and CTEQ10 [7, 8], MRST2008 [9] and MSTW2010 [10] as PDF inputs to Eq.(28). The uncertainty was estimated using the difference between these parameterizations. For R^γ we used Ref. [11]. Effect of possible difference between $R^{\gamma Z}$ and R^γ have been studied as follows: The latest NLO calculations for the deuteron [12] show that $R^{\gamma Z}/R^\gamma \approx 0.99$ at $Q^2 = 2$ (GeV/$c)^2$ and the Q^2 dependence is small. This sets the limit that the effect on our measurement asymmetry due to $R^{\gamma Z}/R^\gamma$ is ≈ 0.15 and ≈ 0.2 ppm, for $Q^2 = 1.121$ and 1.925 (GeV/c^2), respectively.

The non-perturbative couplings between quarks – often called the "higher twist" effects – introduce a Q^2-dependence to the structure functions, in addition to the perturbative QCD evolution. The higher twist effects on the a_3 term was estimated using neutrino data [13] and are found to shift the asymmetry by $+0.70$ ppm and $+1.2$ ppm for the lower and the higher Q^2. The higher twist effects on R^γ were estimated in Ref. [13] and the effect on the asymmetry is < 0.2 ppm for $Q^2 = 1.121$ but is as large as 0.5 ppm for $Q^2 = 1.925$ (GeV/c^2).

Our result at $Q^2 = 1.121$ (GeV/c^2) will set an upper limit on the Q^2-dependence of the hadronic correction. Assuming the Standard Model value for C_{1q} and no corrections from hadronic effects, we will extract the value of $2C_{2u} - C_{2d}$ from the $Q^2 = 1.925$ (GeV/c^2) asymmetry results. The current statistical uncertainty of the asymmetry indicates that we will improve this coupling combination by a factor of five to six compared to the current PDG value [14]. We expect to finalize the analysis and publish these results within the next year.

References

[1] C.Y. Prescott *et al.*, Phys. Lett. **B77**, 347 (1978).

[2] C.Y. Prescott *et al.*, Phys. Lett. **B84**, 524 (1979).

[3] L.W. Mo and Y.-S. Tsai, Rev. Mod. Phys. **41**, 205 (1969).

[4] K. Matsui, T. Sato and T.-S. H. Lee, Phys. Rev. **C72**, 025204 (2005).

[5] M. Gorchtein, C.J. Horowitz, and M. Ramsey-Musolf, Phys. Rev. **C84**, 015502 (2011).

[6] A.V. Afanasev, I. Akushevich and N.P. Merenkov", J. Exp. Theor. Phys. **98**, 403 (2004).

[7] J. Pumplin *et al.*, JHEP **07**, 012 (2002).

[8] H.-L. Lai, M. Guzzi, J. Huston, Z. Li, P.M. Nadolsky *et al.*, Phys. Rev. **D82**, 074024 (2010).

[9] A.D. Martin, W.J. Stirling, R.S. Thorne, G. Watt, Phys. Lett. **B652**, 292 (2007).

[10] A.D. Martin, W.J. Stirling, R.S. Thorne, G. Watt, Eur. Phys. J. **C63**, 189 (2009).

[11] K. Abe *et al.*, Phys. Lett. **B452**, 194 (1999).

[12] L.T. Brady, A. Accardi, T.J. Hobbs, W. Melnitchouk, Phys. Rev. D **84**, 074008 (2011).

[13] S. Alekhin, S.A. Kulagin and R. Petti, AIP Conf. Proc. **967**, 215 (2007); arXiv:0710.0124[hep-ph].

[14] K. Nakamura *et al.* (Particle Data Group), J. Phys. **G37**, 075021 (2010).

3.16 E08-014 - $x > 2$

The $x > 2$ experiment

J. Arrington, D. Day, D. Higinbotham and P. Solvignon, spokespersons,
and
the Hall A Collaboration.
contributed by P. Solvignon and Zhihong Ye.

3.16.1 Motivations

The shell model has been partially successful in describing many features of nuclei such as the structure and energies of the nuclear excited states. However, about 30-40% of the nucleonic strength predicted by the shell model to be in shells below the Fermi level is not seen in the experimental data [1]. This missing strength is thought to be due to the nucleon-nucleon (NN) interaction at short distances and the fact that the close packing of nucleons in nuclei results in a significant probability of overlapping nucleon wavefunctions. These overlapping nucleons belong to a short range correlated cluster and exhibit high momenta, well above the Fermi momentum in the nucleus [2].

Short-range correlations (SRC) are now well accepted as a key ingredient in the formulation of realistic nuclear wave functions. This means that the experimental characterization of SRC is crucial to the development of accurate nuclear structure calculations. Recent results from JLab experiment E01-015 [3] confirmed the overwhelming dominance of the proton-neutron pairs in two-nucleon SRCs. The amplitude and properties of SRCs have important implications not only for the structure of the neutron stars and their cooling process but also in the search for neutrino oscillation.

However, two-nucleon knockout experiments are susceptible to several effects large enough to impact the quantitative conclusions that can be drawn from them. One important aspect is isospin sensitivity. Although inclusive scattering is typically isospin-blind, isospin sensitivity, also called "tensor dominance", can be identified through a careful choice of complementary targets. Isospin-independent and isospin-dependent models predict 25% differences in the cross-section ratios of the two medium-weight nuclei, ^{48}Ca and ^{40}Ca. This experiment complements two-nucleon knockout experiments, for which other physical processes make it difficult to extract a model-independent and precise quantitative measure of the isospin asymmetry.

At $x > 2$, the cross-sections from nuclei heavier than deuterium are expected to be dominated by three-nucleon short-range correlations (3N-SRCs). Results from Hall C experiment E02-019 [4] show a discrepancy with the CLAS results [5] in the $x > 2$ region, while being in very good agreement the 2N-SRC region (see Fig. 56). E02-019 is at higher Q^2 than CLAS, and this is consistent with the hint of possible Q^2 dependence in the CLAS results (see figure 3 of the original proposal [6]). These new data and observations make our measurement decisive in the effort to map precisely the 3N-SRC region and resolve this new issue. E08-014 will also be the first measurement of isospin dependence of 3N-SRC.

3.16.2 Analysis status

JLab experiment E08-014 ran in April-May 2011. This experiment aims at mapping the 2N and 3N-SRC scaling behaviors. It should also provide the first test of the SRC isospin dependence in inclusive electron-nucleus scattering by using two Calcium isotopes. This experiment used the standard Hall A spectrometer configurations for electron detection.

The data analysis is well underway. All detectors performed very well all along the experiment and calibrations (detectors, beamline elements, optics) are considered done at this point.

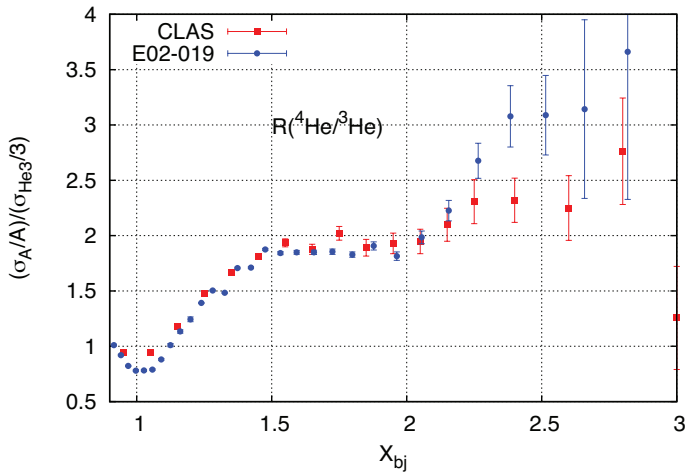

Figure 56: Preliminary results from Hall C experiment E02-019 [4]

- The optics calibration required extra work for the right HRS due to RQ3-mismatching. It was discovered during experiment E08-008, which ran in February 2011, that the right third quadrupole power supply could not reach a current higher than 1100A. E08-008 performed the right optics calibration with a momentum offset for RQ3. It was decided to use the same momentum offset and therefore the same optics calibration data. Figure 57 shows the sieve and multi-foils distributions before and after calibration for the right HRS, and only after calibration for the left HRS.

- The VDC tracking efficiency for one-track events in both HRSs is above 99% after selecting events with number of hits between 5 and 7.

- For some kinematics the background rates (mostly pions) were projected to be an order of magnitude higher than our physics rates. Therefore the main trigger on both HRSs includes the "Cerenkov trigger" requirement. The triggers configuration during E08-014 was as follows:

  – main trigger: S1 **AND** S2 **AND** cerenkov,

  – second trigger: (S1 **OR** S2) **AND** cerenkov,

  – third trigger: S1 **AND** S2.

  The main, second and third triggers are assigned the labels T1, T2 and T6 respectively for the right HRS and T3, T4 and T7 respectively for the left HRS. The trigger scintillator efficiency is then evaluated using:

$$\varepsilon_{scin} = \frac{ps1(3) * N_{T1(3)} + ps6(7) * N_{T6(7)}}{ps1(3) * N_{T1(3)} + ps6(7) * N_{T6(7)} + ps2(4) * N_{T2(4)}} \tag{30}$$

  where $ps[i]$ is the prescale factor and $N_{T[i]}$ the number of event triggers. It was found to be better than 99.95% for the right HRS and better than 99.80% for the left HRS.

- The study of the performance of the Cerenkov detectors requires the use of the third trigger. The detection efficiency is 99.95% for the right HRS cerenkov and 99.77% for the left one. The lower efficiency of the left HRS cerenkov is due to the shorter tank.

- The calorimeters of both spectrometers are also calibrated as shown on Fig. 58 and the resolution is 4.6%(right) and 5.1%(left) for momenta between 2.5 and 3.1 GeV/c.

- The combination of cuts on Cerenkov and calorimeter distributions allows a total pion rejection better than 250:1 (700:1) while keeping 99.86% (99.58%) of the "good electrons" in the right (left) HRS.

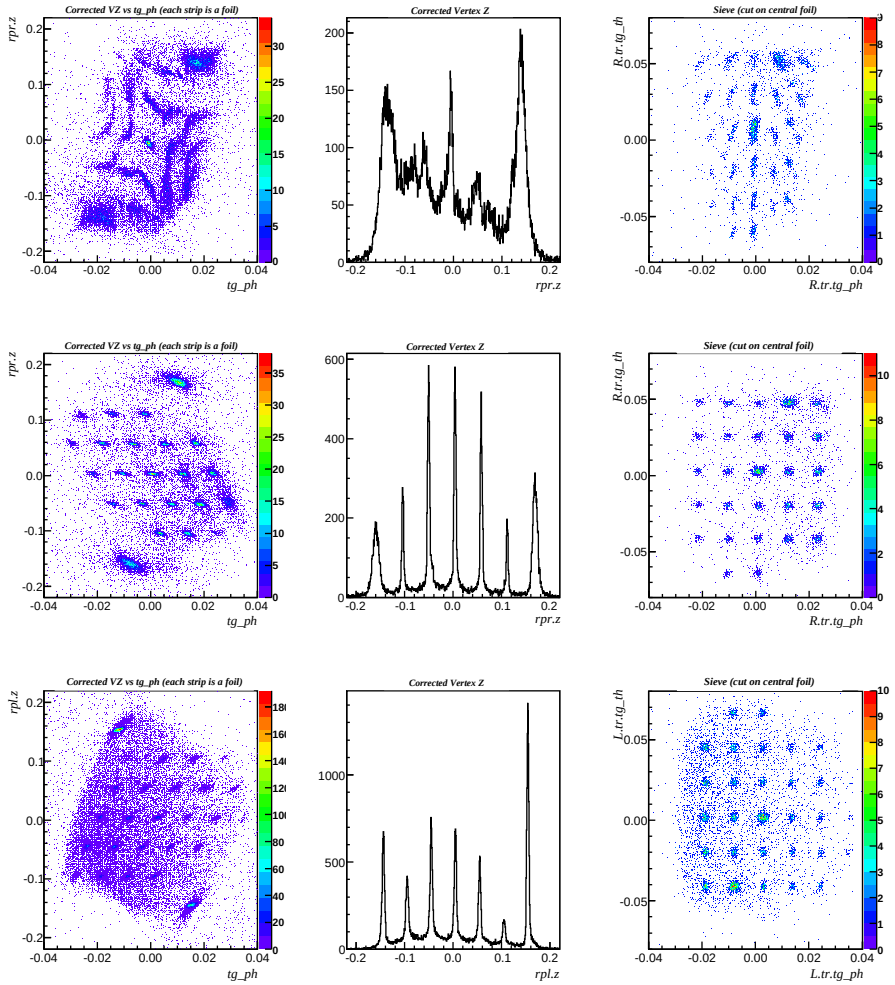

Figure 57: HRS optics calibration. Right HRS with RQ3-mismatching before (top plots) and after (middle plots) calibration. Left HRS after calibration (bottom plots).

At present, efforts are focusing on the target analysis and also on the acceptance/bin centering correction, which are progressing very well. The ^{2}H, ^{3}He and ^{4}He target density will be extracted from the "boiling study". The online analysis shows a density decrease of 18%, 24% and 22% for the ^{2}H (@ 45μA), ^{3}He (@ 120μA) and ^{4}He (@ 95μA) targets respectively, while the rate dependence, measured on carbon up to 95μA, is less than 1%. These numbers were used to adjust the data taking time at each kinematics.

Preliminary SRC ratios are expected to be released during Summer 2012. Figure 59 shows the statistical quality of the isospin study, i.e. taking the cross-section ratios of ^{48}Ca and ^{40}Ca. Due to miscommunication between JLab and Oak Ridge National Lab (ORNL), only the ^{48}Ca foil was made at ORNL. Therefore JLab target group used natural ^{40}Ca to make the foil needed for the experiment. With the equipment available at JLab, it was not possible to obtain a ^{40}Ca foil as uniform as the ^{48}Ca foil made at ORNL. During E08-014, data were taken to look at the thickness and uniformity of the foils. Even though the systematic uncertainty of the isospin ratio is anticipated to be higher than previously estimated in the proposal.

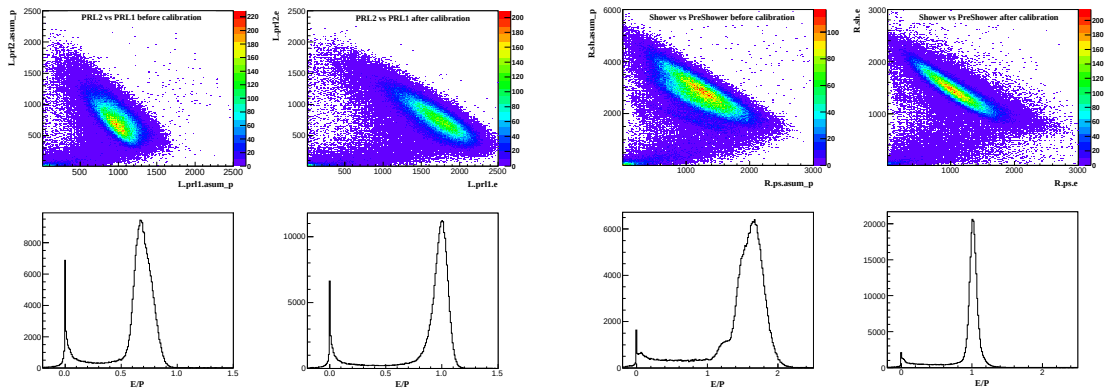

Figure 58: HRS calorimeters calibration. The four left (right) plots are for the left (right) HRS calorimeter.

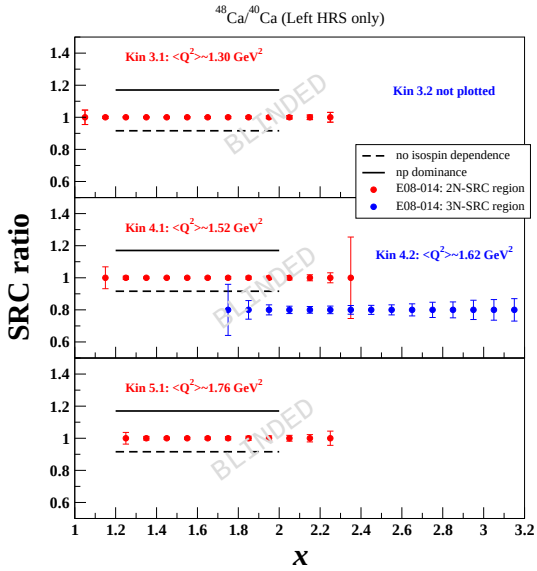

Figure 59: Isospin study: statistical precision (blinded) and the expected values of the 2N-SRC plateau in both isospin scenarios. Only left HRS data are included in the plot.

References

[1] L. Lapikas, Nucl. Phys. **A553**, 297c (1993).

[2] L.L. Frankfurt, M.I. Strikman, D.B. Day, M. Sargsian, Phys. Rev. C **48**, 2451 (1993).

[3] R. Shneor *et al*, Phys. Rev. Lett. **99**, 072501 (2007).

[4] N. Fomin *et al*, arXiv:1107.3583, submitted to PRL.

[5] K.S. Egiyan *et al*, Phys. Rev. Lett. **96**, 082501 (2006).

[6] P. Solvignon, J. Arrington, D.B. Day, D. Higinbotham *et al.*, Jefferson Lab experiment E08-014.

3.17 E08-027 - g_2^p

A. Camsonne, J.P. Chen, D. Crabb, K. Slifer, spokespersons,
and
the Hall A Collaboration.
contributed by K. Slifer

3.17.1 Introduction

The inclusive scattering spin structure functions (SSF) g_1 and g_2 are fundamental spin observables which characterize the deviation of the nucleon's spin-dependent properties from point-like behavior. Their measurement provides insight into QCD via tests of sum rule predictions, chiral perturbation (χPT) and lattice gauge theory calculations, and insight into higher twists and the nature of confinement. Recently, it has also become apparent that poor knowledge of the SSFs (which are purely QCD quantities) at low Q^2 limits the precision of QED calculations of simple bound systems, such as the hydrogen-like atom [1, 2]. Energy levels in these systems can be measured to extremely high precision, so the corresponding QED calculations have been pushed to a level where the finite size of the nucleon, as characterized by the structure functions and elastic form factors (FF), has become a leading uncertainty. Of particular interest, researchers from PSI [2] have obtained a value for the proton charge radius $\langle R_p \rangle$ via measurements of the Lamb shift in muonic hydrogen, which differs significantly from the value from elastic electron proton scattering. The deviation in $\langle R_p \rangle$ would have many troubling consequences, such as requiring a sizable shift in the fundamental Rydberg constant, so all aspects of the PSI calculations are being re-examined. The main uncertainties in the PSI results originate from the proton polarizability and from different values of the Zemach radius. These quantities are determined from integrals of the SSF and elastic form factors, which due to kinematic weighting, are dominated by the low Q^2 region. It is prudent to question whether these uncertainties are underestimated, since g_2^p is largely unmeasured, and g_1^p data extends only down to $Q^2 \approx 0.05$ GeV^2. The Zemach radius, is similarly dominated by the low Q^2 behavior of the proton elastic form factors G_E and G_M.

The existing data has also revealed a striking discrepancy [3] of χPT calculations with the longitudinal-transverse polarizability δ_{LT}^n. This is surprising since δ_{LT} was expected to be a good testing ground for the chiral dynamics of QCD [4, 5] due to it's relative insensitivity to resonance contributions. Measurement of g_2^p at low Q^2 will give access to δ_{LT}^p and allow an isospin examination of this 'δ_{LT} puzzle'.

3.17.2 The Experiment

E08-027 installation in Hall A is in progress. We will perform an inclusive measurement at forward angle of the proton spin-dependent cross sections in order to determine the g_2^p structure function and the longitudinal-transverse spin polarizability δ_{LT} in the resonance region for $0.02 < Q^2 < 0.20$ GeV^2. To reach the lowest possible momentum transfer, a pair of room temperature septa magnets have been installed to allow detection of scattered electrons at 5.69°. The Dynamical Nuclear Polarization (DNP) proton target is being prepared in the EEL large bay. The target's superconducting magnet coil was damaged during testing in September, and is in the process of being replaced with a similar coil package from the Hall B polarized target. Repairs are on schedule to be completed before the holiday break, which will allow target installation in the Hall to begin in early January.

We expect the experiment to be ready for production in early to mid February. This late start permits complete running of five planned configurations, but jeopardizes two planned kinematics at large Q^2 (See Fig. 60). These two bands required a disproportionately large number of calendar days due to the drop in rates as the scattering angle increases, and the transition time needed to remove the septa magnets. As shown in Fig. 62, this impacts only the largest Q^2 bin of E08-027. The low Q^2 portion remains. This represents a large fraction of the planned kinematics,

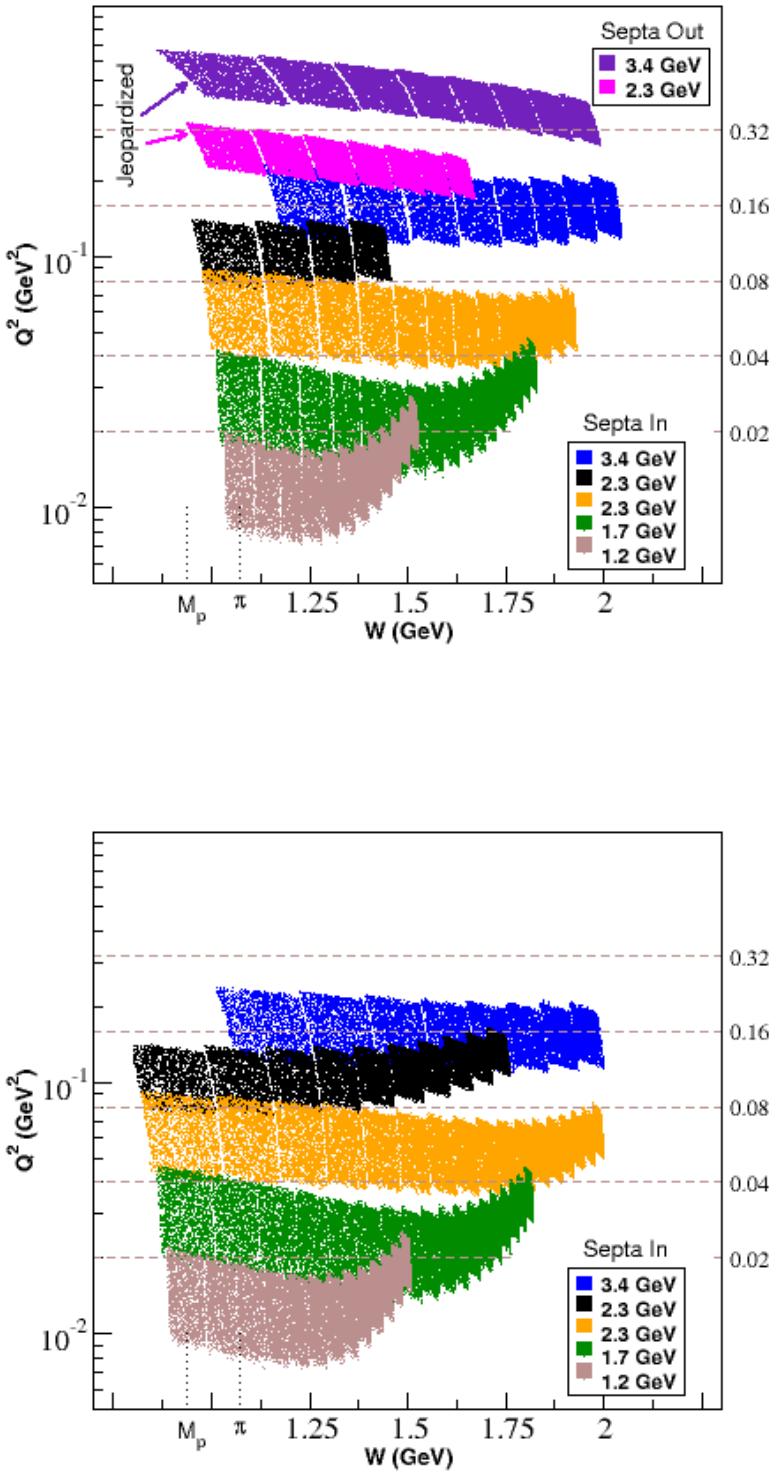

Figure 60: **Top**: Full kinematic coverage. **Bottom**: Reduced kinematics assuming Feb. 14 start date and use of the Hall B magnet coil.

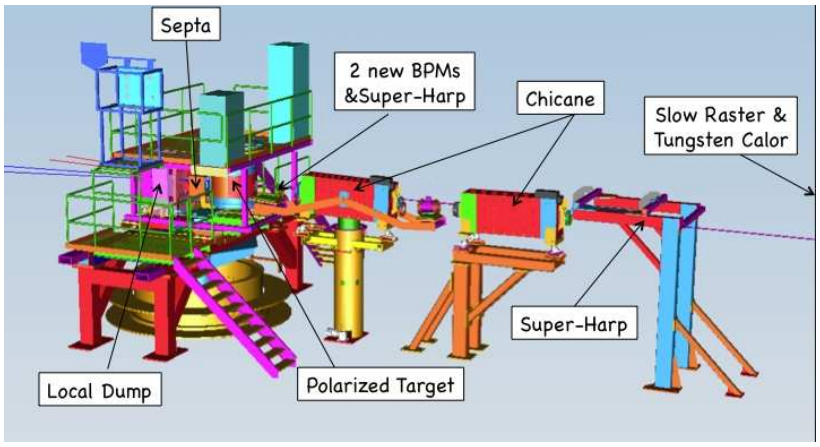

Figure 61: E08-027 installation in Hall A.

and covers the region which most heavily impacts the proton polarizability, the HF splitting, and the proton charge radius uncertainty.

The lower panel of Fig. 60 shows the expected coverage for the run starting at Feb. 14 and continuing to the planned Hall A stoppage at May 11. With the Hall B coil package, we anticipate a drop in the target's figure of merit compared to the previous configuration. This is due to the smaller uniform field region, which will require a reduction of the target length. The projected results in Fig. 62 assumes 75 calendar days, which are now available since we will not require a lengthy transition time to remove the septa magnets. Additional commissioning days will be performed in December and February. The December commissioning will focus on the new beamline diagnostics, Moller polarimeter, HRS detector stack, new 3rd arm detector, and all associated data acquisition systems. We will commission the chicane and local dump when the polarized target has been installed.

E08-027 complements two other related experiments : EG4 which will measure the proton g_1 structure function, and E08-007 which will measure the proton form factor ratio G_E/G_M in the same kinematic region as E08-027. Because of the similarities in technique and equipment, the E08-027 and E08-007 collaborations are highly cooperative and the two experiments will run simultaneously. E08-007 will focus on elastic scattering, while E08-027 measures the inelastic data. Together, these experiments will provide the definitive measurement of proton's spin-dependent structure at low Q^2.

To help reduce the impact of the losses at large Q^2, we are using a portion of the previously planned 'transition days' to extend the 2.2 GeV energy coverage to larger invariant mass W (black and yellow bands in Fig. 60), and will spend additional time in the elastic/Q.E. region. This data will be useful to help constrain the Q^2 interpolation, and provide an independent check of the product of beam and target polarizations via measurement of the elastic asymmetry. It is also necessary for E08-007 in order to compensate for the loss of sensitivity to G_E/G_M in the allowed target orientations.

3.17.3 Recent Progress

E08-027 has 6 full time Ph.D. students onsite: **T. Badman (UNH), M. Cummings (W&M), C. Gu (UVa), M. Huang (Duke), P. Zhu (USCT)**, and **R. Zielinski (UNH).** An additional student, **J. Chen (UVa)**, is splitting his Ph.D. work between E08-027 and a 12 GeV project. Four post-docs are working on E08-027: **K. Allada (JLab), J. Maxwell (UNH), V. Sulkosky (MIT**), and **J. Zhang (JLab)**. There is also additional significant contributions from students and post-docs of the E08-007 collaboration.

Installation in the hall is nearly complete. The beamline has been modified with two large FZ magnets to provide

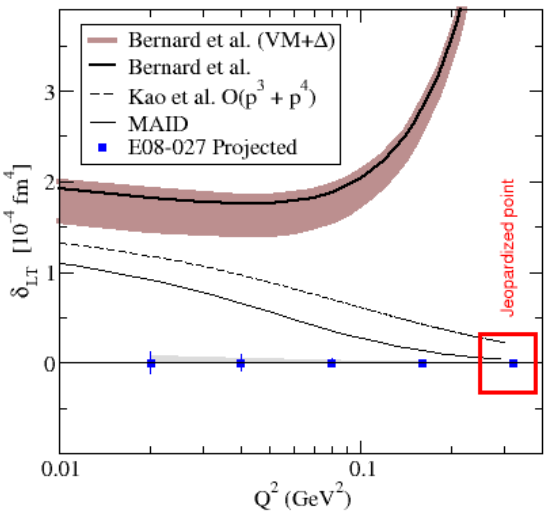

Figure 62: E08-027 projection for the LT polarizability showing the data point at $Q^2 = 0.32$ that will be lost.

upstream chicaning of the beam prior to encountering the polarized target magnetic field. Two new super-harps and two new M15 antennae style BPMs have been installed to enable full characterization of the low current ($\sim$100 nA) beam as it is transported thru the chicane. New software and electronic needed to operate the precise 4 channel BPM readouts are being completed and are expected ready by January. For the December commissioning, the new BPMs will be readout using the existing SEE electronics and software. The Happex DAQ will be used to readout the BPMs and BCMs, to provide significantly lower noise during operation at low current. A low current tungsten calorimeter has been installed upstream. It is operational and ready for commissioning. The large target cup diameter ($\sim$ 2 cm) required the installation of a new slow raster, which is also ready for commissioning. Collaboration students have been trained in the operation of both devices.

The room temperature septum is on the target pivot, fully powered, and ready for testing in early December to determine the hysteresis curve and resolve its maximum operational field. A third arm detector to independently monitor the product of beam and target polarizations has been designed and installed on beam left at an angle of approximately 70°. This device will serve as a cross-check of the primary polarimetry provided by the target NMR and beam Moller measurements. A full simulation of the new beamline, polarized target and septa has been included in the Hall A Geant4 simulation. SNAKE modeling of the passage of the beam through the Septum field and spectrometer has also been completed.

Target installation has begun in the hall, with construction of a new bunker for electronics racks and control computers. The target will rest on the new two level target platform shown if Fig. 61. Besides the onsite target preparations, the UVa group recently lead two target material irradiations at NIST, in Gaithersburg MD. Another is planned for January 2012. This is necessary to prepare the ammonia samples with paramagnetic centers needed for the DNP process. There was also a target cooldown at UVa to test the operation of the polarizing apparatus at the non-standard configuration (2.5 T/70 GHz) planned for a portion of E08-027. Another cooldown will occur before the end of the year to test the new material from NIST and to finish optimization of the 2.5T configuration.

In January, there will be a review to evaluate the readiness of the experiment to move safely into production mode.

References

[1] V. Nazaryan, C. E. Carlson and K. A. Griffioen, Phys. Rev. Lett. **96**, 163001 (2006).

[2] R. Pohl *et al.*, Nature **466**, 213 (2010).

[3] M. Amarian *et al.* [Jefferson Lab E94010 Collaboration], Phys. Rev. Lett. **93**, 152301 (2004).

[4] V. Bernard, T. R. Hemmert and U. G. Meissner, Phys. Lett. B **545**, 105 (2002).

[5] C. W. Kao, T. Spitzenberg and M. Vanderhaeghen, Phys. Rev. D **67**, 016001 (2003).

3.18 E12-10-009 - APEX

An Electron Fixed-Target Experiment to Search for a New Vector Boson A' Decaying to e^+e^-

Rouven Essig, Philip Schuster, Natalia Toro, Bogdan Wojtsekhowski
and the Hall A Collaboration.

3.18.1 Introduction

The development of the Standard Model of particle interactions is the culmination of a century of searches and analyses with fixed-target and colliding beam experiments. The Standard Model describes all known matter, and its interactions through the strong, weak, and electromagnetic forces mediated by vector bosons of the Standard Model. New forces beyond the Standard Model could have escaped detection only if their mediators are either heavier than $O(\text{TeV})$ or quite weakly coupled. The latter possibility can arise through a simple and generic mechanism proposed by Holdom [1], in which a new vector particle A'_μ (the *dark photon*) mixes via quantum loops with the Standard Model photon. This mixing, with a typical strength $\varepsilon \sim 10^{-2} - 10^{-6}$, in turn induces a minute charge for ordinary matter under the new force, so that the dark photons coupling to matter is smaller than that of the photon by $\alpha'/\alpha = \varepsilon^2$. In this context, MeV–GeV masses for the A' are both well-motivated and weakly constrained, with limits at $\varepsilon e \lesssim 0.3 \times 10^{-2} e$ for most A' masses between 10 MeV and 1 GeV.

Fixed-target experiments with high-intensity electron beams and existing precision spectrometers are ideally suited to explore sub-GeV forces by probing reactions in which a new A' vector particle is produced by radiation off an electron beam [2, 3]. The A' can decay to an electron and positron pair and appears as a narrow resonance of small magnitude in the invariant mass spectrum. In [2], several fixed-target experimental strategies were outlined to search for new sub-GeV vector interactions.

The C12-10-009 experiment is a concrete plan for an A' search using the CEBAF accelerator and the High Resolution Spectrometers (HRS) in Hall A [4]. This experiment, the A' *Experiment* (APEX), can probe charged particle couplings with new forces as small as $3 \times 10^{-4} e$ and masses between 65 MeV and 525 MeV — an improvement by two orders of magnitude in cross section sensitivity over present limits across most of this mass range.

Fixed-target experiments of this form are particularly timely in light of a series of recent anomalies from terrestrial, balloon-borne, and satellite experiments that suggest that dark matter interacts with Standard Model particles. Much of this data hints that dark matter is directly charged under a new force mediated by an A' and not described by the Standard Model. Theoretical as well as phenomenological expectations suggest an A' mass $m_{A'} \lesssim 1\,\text{GeV}$ and $\varepsilon e \lesssim 10^{-2} e$.

Expected reach and impact APEX will be sensitive to new gauge bosons with couplings as small as $\varepsilon^2 \equiv \alpha'/\alpha \sim 9 \times 10^{-8}$ and masses in the range $65 - 525\,\text{MeV}$ (here α (α') is the coupling of the photon (A') to electrically charged matter). This is about a factor of $3 - 10$ times lower in ε than existing constraints (several of which also rely on an A' coupling also to muons), and corresponds to $\sim 10 - 100$ times smaller cross-sections.

The precise mass range probed by this type of experiment can be varied by changing the spectrometer angular settings and/or the beam energies, see the APEX plan in Figure 63. The parameter range probed by APEX is interesting for several reasons. This region of mass and coupling is compatible with A''s explaining the annual modulation signal seen by the dark matter direct detection experiment DAMA/LIBRA, and also with dark matter annihilating into A's, which explains a myriad of recent cosmic-ray and other astrophysical anomalies. In addition, and independently of any connection to dark matter, the APEX experiment would be the first to probe A's of mass $\gtrsim 50\,\text{MeV}$ with gauge kinetic mixing significantly below $\varepsilon \sim 10^{-3}$, the range most compatible if the Standard Model hypercharge gauge

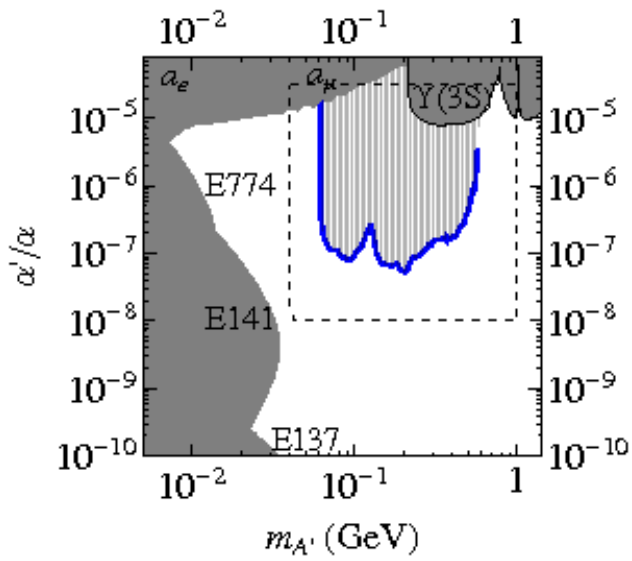

Figure 63: The reach of the APEX experiment (blue contour), existing constraints (gray shaded and hatched regions), and other proposed experiments (colored lines). The region in which an A' could explain the anomalous measurement of the muon $g-2$ is shaded in green.

force is part of a Grand Unified Theory.

The importance for fundamental physics of precision searching for new forces near the GeV scale cannot be overstated.

Concept In the APEX experiment, we are interested in collecting as many true e^+e^- coincidence events as possible, since the A' is expected to decay to e^+e^- pairs. A large background of such true coincidence events is expected also from Standard Model QED Bethe-Heitler and radiative trident processes, but the A' would appear as a narrow spike on top of this large Standard Model background. A further background is the accidental e^+e^- coincidences that come from two distinct scattering events, in which an electron scatters into the L-HRS from one event, while a positron scatters into the R-HRS in a second event within the timing window of the trigger. Lastly, there are both true and accidental $e^-\pi^+$ coincidence events. Rejection of these two backgrounds is key to the A' search and is achieved by means of a short trigger timing window and good particle identification (PID).

The other crucial factor in determining the sensitivity of this experiment is the optics, which determines the ultimate mass resolution of the experiment. Since we are looking for a narrow spike on top of a large, smooth QED background, excellent mass resolution is essential to achieve the best possible sensitivity to an A'. In the APEX experiment it is crucial to take into account the above considerations.

Figure 64 shows the layout of the APEX experiment. The central momenta of the both spectrometers are set to half of the beam energy. At such a setting the background rates are minimized. The same time most of A' events will be detected in spite of small momentum bite of the HRSs.

Our *coincidence trigger* is defined as a signal in the S2m of both the left HRS *and* the right HRS, *and* a signal in the Gas Cherenkov counters of the right HRS. The coincidence trigger based on these three signals allows us to collect true coincidence events with high efficiency and acceptable DAQ dead time. Such events are candidates for true coincident e^+e^- signal events.

The design of the target for the APEX experiment shown in Figure 65 has a number of interesting ideas including a concept of narrow ribbons, a tension mechanism, and alignment and calibration target sets.

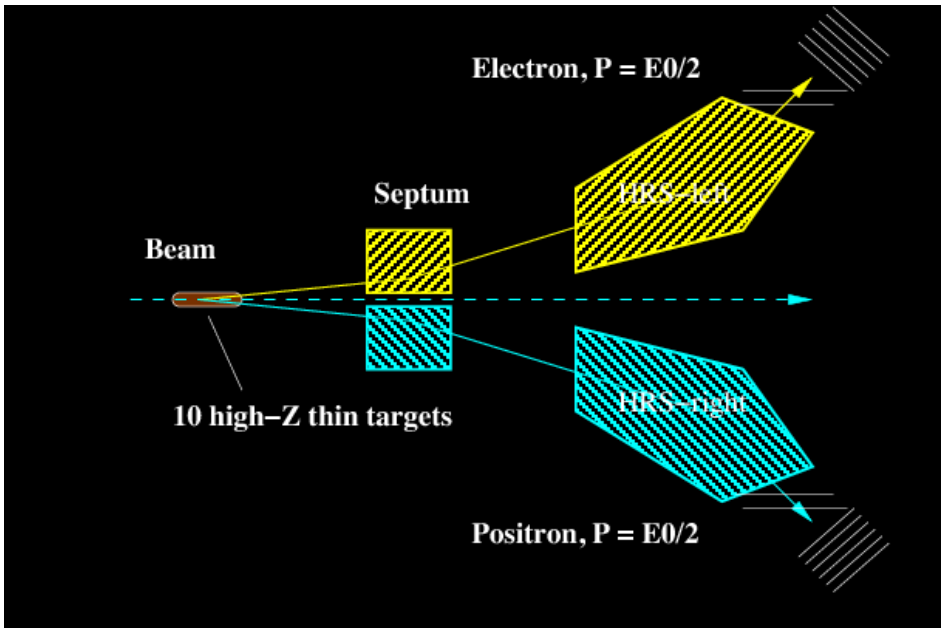

Figure 64: The layout of the APEX experimental setup.

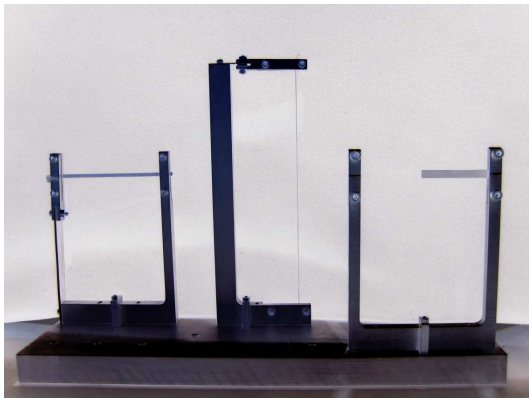

Figure 65: The components of the target for the APEX experiment.

3.18.2 Test Run Results and Future Plans

A test run was recommended by PAC35, and realized after the PREX experiment in June 2010. The primary purpose of the test-run was to demonstrate the detector performance necessary for a full APEX run, including:

1. Demonstrate that the gas Cherenkov counters can be used effectively in a coincidence trigger to reduce the pion accidental trigger rate, even at high count rates (a sufficient online rejection of $1/30$ was achieved)
2. Measure the importance of different contributions to background and their agreement with simulation (all QED backgrounds agreed within 10–20% uncertainties; pion background rates were lower than the WISER expectation by a factor of 6 at 2 GeV).
3. Prove that a successful 20 ns triple-coincidence trigger (S0-S0-C) can be achieved.
4. Prove that the vertical drift chambers (VDCs) can operate at a rate higher than 20 kHz/wire (performance was sufficient up to the anticipated 6 MHz singles rate; efforts to reduce inefficiencies at these high rates are ongoing)

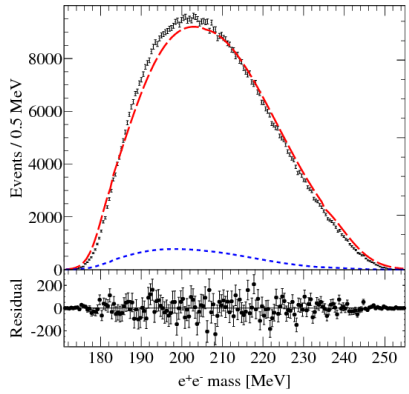

Figure 66: Upper panel: The invariant mass spectrum of e^+e^- pair events in the final event sample (black points, with error bars), accidental e^+e^- coincidence events (blue short-dash line), and the QED calculation of the trident background added to the accidental event sample (red long-dash line). Lower panel: the bin-by-bin residuals with respect to a 10-parameter fit to the global distribution (for illustration only, not used in the analysis).

The detectors were tested in all the extreme conditions expected during the APEX production run. Further results on these topics were presented at the A'-boson workshop [5] at JLab in September 2010. The observed detector performance was found to be in compliance with the APEX requirements.

In addition, a science dataset of 700,000 QED e^+e^- events (Fig. 66) was obtained during the test run. These allowed an A' search over the mass range from 175 to 250 MeV, which in the lower half of the mass range exceeds all other experiments' sensitivity by an order of magnitude [6]. As no signal was seen, an upper limit on α'/α was obtained, shown in Figure 67.

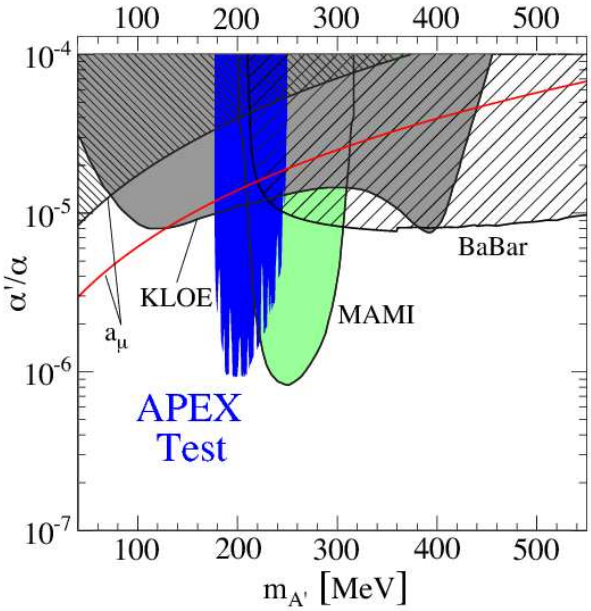

Figure 67: The 90% confidence upper limit on α'/α versus A' mass for the APEX test run (solid blue). Also shown are existing 90% confidence level limits from the muon anomalous magnetic moment a_μ (fine hatched) [7], KLOE (solid gray) [8], the result reported by Mainz (solid green) [9], and an estimate using a BaBar result (wide hatched) [2, 3, 10]. Between the red line and fine hatched region, the A' can explain the observed discrepancy between the calculated and measured muon anomalous magnetic moment [7] at 90% confidence level. The full APEX experiment will roughly cover the entire area of the plot.

References

[1] B. Holdom, *Two U(1)'s and Epsilon Charge Shifts*, *Phys. Lett.* **B166** (1986) 196.

[2] J. D. Bjorken, R. Essig, P. Schuster, and N. Toro, *New Fixed-Target Experiments to Search for Dark Gauge Forces*, *Phys. Rev.* **D80** (2009) 075018, [0906.0580].

[3] M. Reece and L.-T. Wang, *Searching for the light dark gauge boson in GeV-scale experiments*, 0904.1743.

[4] A New Proposal to Jefferson Lab PAC35: Search for a New Vector Boson A' Decaying to e^+e^-, "http://hallaweb.jlab.org/collab/PAC/PAC35/PR-10-009-Dark-Matter-Search.pdf."

[5] The Workshop "Searching for a New Gauge Boson at JLab", September 20-21, 2010,"http://conferences.jlab.org/boson2010/index.html."

[6] S. Abrahamyan *et al.* [APEX Collaboration], Phys. Rev. Lett. **107**, 191804 (2011) [arXiv:1108.2750 [hep-ex]].

[7] M. Pospelov, Phys. Rev. D **80**, 095002 (2009) [arXiv:0811.1030 [hep-ph]].

[8] KLOE-2 Collaboration, arXiv:1110.0411 [hep-ex].

[9] H. Merkel *et al.* [A1 Collaboration], Phys. Rev. Lett. **106**, 251802 (2011) [arXiv:1101.4091 [nucl-ex]].

[10] B. Aubert *et al.* [BABAR Collaboration], arXiv:0902.2176 [hep-ex].

4 Publications

1. J. Huang, *et al.*, Beam-Target Double Spin Asymmetry A_{LT} in Charged Pion Production from Deep Inelastic Scattering on a Transversely Polarized ^{3}He Target at $1.4 < Q^2 < 2.7\mathrm{GeV}^2$, arXiv:1108.0489 [nucl-ex]

2. K. Paschke *et al.*, New Precision Limit on the Strange Vector Form Factors of the Proton, arXiv:1107.0913 [nucl-ex]

3. X. Qian, *et al.*, Single Spin Asymmetries in Charged Pion Production from Semi-Inclusive Deep Inelastic Scattering on a Transversely Polarized ^{3}He Target, Phys. Rev. Lett. **107**, 072003 (2011)

4. G. Ron *et al.*, Low Q^2 measurements of the proton form factor ratio $mu_p G_E/G_M$, arXiv:1103.5784 [nucl-ex]

5. A.J.R. Puckett *et al.*, Reanalysis of Proton Form Factor Ratio Data at $Q^2 = 4.0$, 4.8, and 5.6 GeV^2, arXiv:1102.5737 [nucl-ex]

6. S. P. Malace *et al.*, Precise Extraction of the Induced Polarization in the $^4\mathrm{He}(e,e'p)^3\mathrm{H}$ Reaction, Phys. Rev. Lett. **106**, 052501 (2011)

7. E. Fuchey, *et al.*, Exclusive Neutral Pion Electroproduction in the Deeply Virtual Regime, Phys. Rev. **C83**, 025201 (2011)

8. J. Glister *et al.*, Polarization Observables in Deuteron Photodisintegration below 360 MeV, Phys. Lett. **B697**, 194-198 (2011)

9. G.D. Cates *et al.*, Flavor Decomposition of Elastic Nucleon Electromagnetic Form Factors, Phys. Rev. Lett. **106**, 252003 (2011)

10. X. Zhan *et al.*, High-precision Measurement of the Proton Elastic FF Ratio at low Q^2, Phys. Lett. **B705**, 59 (2011)

11. M. Friend *et al.*, Upgraded photon calorimeter with integrating readout for Hall A Compton Polarimeter at Jefferson Lab, arXiv:1108:3116 [nucl-ex]

12. S. Ban *et al.*, Parity Violating Electron Scattering Measurements of Neutron Densities, J. Phys. **G39**, 015104 (2012)

13. L. B. Weinsten *et al.*, Short Range Correlations and the EMC Effect, Phys. Rev. Lett. **106**, 052301 (2011)

14. J. Arrington *et al.*, Hard Probes of Short-Range Nucleon-Nucleon Correlations, arXiv:1104.1196 [nucl-ex]

15. M. Meziane *et al.*, Search for Effects Beyond the Born Approximation in Polarization Transfer Observables in $\vec{e}p$ Elastic Scattering, Phys. Rev. Lett **106**, 132501 (2011)

16. S. Abrahamyan *et al.*, Measurement of the Neutron Radius of ^{208}Pb Through Parity-violation in Electron Scattering, arXiv:1201:2568 [nucl-ex]

5 Theses

1. *Measuring of Neutron Electric Form-Factor G_E^n at High Momentum Transfer*, Sergey Abrahamyan, Yerevan Physics Institute

2. *Double Spin Asymmetry A_{LT} in Charged Pion Production from Deep Inealstic Scattering on a Transversely Polarized* ^{3}He *Target*, Jin Huang, Massachusetts Institute of Technology

3. *Extraction of G_E^n at $Q^2 = 1.0\ (\mathrm{GeV/c})^2$ from Measurements of* $^3\overrightarrow{\mathrm{He}}(\vec{e}, e')$, Ge Jin, University of Virginia

4. *Measurements of the Double-Spin Asymmetry A_1 on Helium-3: Toward a Precise Measurement of the Neutron A_1*, Diana Parno, Carnegie Mellon University

5. *The Design and Construction of a Green Laser and Fabry-Perot Cavity System for Jefferson Lab's Hall A Compton Polarimeter*, Abdurahim Rakhman, Syracuse University

6. *Measurment of Target Single-spin Asymmetry in Charged Kaon Electroproduction on a Transversely Polarized* ^{3}He *Target*, Youcai Wang, University of Illinois at Urbana-Champaign

7. *Precision Measurement of Longitudinal and Transverse Response Functions of Quasi-Elastic Electron Scattering in the Momentum Transfer Range* $0.55\ \mathrm{GeV/c} \leq |q| \leq 1.0\ \mathrm{GeV/c}$, Xinhu Yan, University of Science and Technology of China

8. *Precision Measurement of Longitudinal and Transverse Response Functions of Quasi-Elastic Electron Scattering in the Momentum Transfer Range* $0.55\ \mathrm{GeV/c} \leq |q| \leq 1.0\ \mathrm{GeV/c}$, Huan Yao, Temple University

6 Hall A Collaboration Member List

Argonne National Lab
John Arrington
Frank Dohrmann
Paul Reimer
Jaideep Singh
Krishni Wijesooriya
Xiaohui Zhan

Budker Institute of Nuclear Physics
Dima Nikolenko
Igor Rachek

Cairo University
Hassan Ibrahim

California Institute of Technology
Steffen Jensen
Cathleen Jones
Xin Qian

California State University
Konrad A. Aniol
Martin B. Epstein
Dimitri Margaziotis

Carnegie Mellon University
Gregg Franklin
Megan Friend
Vahe Mamyan
Brian Quinn
Luminita Todor

The Catholic University of America
Tanja Horn

China Institute of Atomic Energy (CIAE)
Xiaomei Li
XinHu Yan
Shuhua Zhou

Christopher Newport University
Ed Brash
Fatiha Benmokhtar

College of William and Mary
David S. Armstrong
Todd Averett
Juan Carlos Cornejo
Melissa Cummings
Wouter Deconinck
Keith Griffioen
Joe Katich
Lubomir Pentchev
Charles Perdrisat
Bo Zhao

Dapnia/SphN
Etienne Burtin
Christian Cavata
Nicole d'Hose
Jean-Eric Ducret
Stephanie Escoffier
Bernard Frois
Sophie Kerhoas
David Lhuillier
Jacques Marroncle
Damien Neyret
Stephane Platchkov
Thierry Pussieux
Franck Sabatie
Antonin Vacheret
Pascal Vernin

Duke University
Steve Churchwell
Haiyan Gao
Calvin Howell
Min Huang
Simona Malace
Yi Qiang
Richard Walter
Qiujian Ye

Faculte des Sciences de Monastir (Tunisia)
Malek Mazouz

Florida International University
Armando Acha
Werner Boeglin
Luminiya Coman
Marius Coman
Hari Khanal
Laird Kramer
Pete Markowitz
Brian Raue

Jeorg Reinhold

Fudan University
Xiaofeng Zhu

General Electric
Jianguo Zhao

Gent State University
Natalie Degrande
Luc Van de Hoorebeke
Robert Van de Vyver

The George Washington University
Ramesh Subedi

Gesellschaft fur Schwerionenforschung (GSI)
Javier Rodriguez Vignote

Hampton University
Leon Cole
Ashot Gasparian
Peter Monaghan

Harvard Medical School
Hong Xiang

Harvard University
Richard Wilson

Hebrew University of Jerusalem
Moshe Friedman
Guy Ron

Huangshan University
Xinhu Yan

Idaho State University
Dustin McNulty

INFN/Bari
Raffaele de Leo

INFN/Catania
Vincenzo Bellini
Sutera Concetta Maria
Antonio Guisa
Francesco Mammoliti
Giuseppe Russo
Maria Leda Sperduto

INFN/Lecce
Roberto Perrino

INFN/Roma
Marco Capogni
Francesco Cusanno
Salvatore Frullani
Franco Garibaldi
Franco Meddi
Guido Maria Urciuoli
Evaristo Cisbani
Rachel di Salvo
Mauro Iodice

Institut de Physique Nucleaire
Louis Bimbot
Alejandro Marti Jimenez-Arguello

Institute of Modern Physics, Chinese Academy of Sciences
Xurong Zhen

ISN Grenoble
Serge Kox
Jean Mougey
Gilles Quemener
Eric Voutier

Jefferson Lab
Kalyan Allada
Alexandre Camsonne
Larry Cardman
Jian-Ping Chen
Eugene Chudakov
Kees de Jager
Alexandre Deur
Ed Folts
David Gaskell
Javier Gomez
Ole Hansen
Douglas Higinbotham
Mark K. Jones

John Lerose
Bert Manzlak
David Meekins
Robert Michaels
Bryan Moffit
Sirish Nanda
Noel Okay
Lester Richardson
Yves Roblin
Brad Sawatzky
Jack Segal
Dennis Skopik
Patricia Solvignon
Mark Stevens
Riad Suleiman
Stephanie Tysor
Bogdan Wojtsekowski
Jixie Zhang

Jozef Stefan Institute
Miha Mihovilovic
Simon Sirca

Kent State University
Bryon Anderson
Mina Katramatou
Elena Khrosinkova
Elena Long
Richard Madey
Mark Manley
Gerassimos G. Petratos
Larry Selvey
Andrei Semenov
John Watson

Kharkov Institute of Physics and Technology
Oleksandr Glamazdin
Viktor Gorbenko
Roman Pomatsalyuk

Kharkov State University
Pavel Sorokin

Lanzhou University
Yi Zhang

Longwood University
Tim Holmstrom
Keith Rider

Jeremy St. John
Wolfgang Troth

Los Alamos Laboratory
Lei Guo
Jin Huang
Xiaodong Jiang
Han Liu
Ming Xiong Liu
Andrew Puckett

LPC Clermont-Ferrand France
Pierre Bertin
Helene Fonvielle
Eric Fuchey
Florian Itard
Bernard Michel
Carlos Munoz Camacho

Mississippi State University
Dipangkar Dutta
Mitra Shabestari
Amrendra Narayan
Nuruzzaman

MIT
Bill Bertozzi
Shalev Gilad
Aidan Kelleher
Navaphon “Tai” Muangma
Kai Pan
Cesar Fernandez Ramirez
Vincent Sulkosky
Wang Xu

Negev Nuclear Research Center
Arie Beck
Sharon Beck

NIKHEF
Jeff Templon

Norfolk State University
Mahbub Khandaker
Vina Punjabi

North Carolina Central University
Benjamin Crowe
Branislav (Branko) Vlahovic

Northwestern University
Issam Qattan
Ralph Segel

Ohio University
Julie Roche

Old Dominion University
Gagik Gavalian
Mohamed Hafez
Wendy Hinton
Larry Weinstein
Charles Hyde

Pacific Northwest National Lab
Kathy McCormick
Brian Milbrath

Princeton University
Ioannis Kominis

Regina University
Alexander Kozlov

Renaissance Tech
Robert Lourie
Joseph Mitchell
Paul Ulmer

Rutgers University
Lamiaa El Fassi
Ron Gilman
Gerfried Kumbartzki
Ronald Ransome
Yawei Zhang

Saint Norbert College
Michael Olson

Seoul National University
Seonho Choi
Byungwuek Lee

Smith College
Piotr Decowski

St Mary's University
Davis Anez Jackie Glister
Adam Sarty

Stanford Linear Accelerator
Rouven Essig

SUBATECH
Jacques Martino

Syracuse University
Zafar Ahmed
Richard Holmes
Abdurahim Rakhman
Paul A. Souder

Tel Aviv University
Nathaniel Bubis
Or Chen
Igor Korover
Jechiel Lichtenstadt
Eli Piasetzky
Ishay Pomerantz
Ran Shneor
Israel Yaron

Temple University
David Flay
Sebastian Incerti
Zein-Eddine Meziani
Matthew Posik
Nikos Sparveris
Huan Yao

Tohoku University
Kouichi Kino
Kazushige Maeda
Teijiro Saito
Tatsuo Terasawa
H. Tsubota

Tsinghua University
Zhigang Xiao

Universidad Complutense de Madrid (UCM)
Joaquin Lopez Herraiz
Luis Mario Fraile
Maria Christina Martinez Perez
Jose Udias Moinelo

Universitat Pavia
Sigfrido Boffi

University "La Sapienza" of Rome
Fulvio De Persio

University of Glasgow
John Annand
David Hamilton
Dave Ireland
Ken Livingston
Dan Protopopescu
Guenther Rosner
Johan Sjoegren

University of Illinois
Ting Chang
Areg Danagoulian
Alan Nathan
J.C. Peng
Mike Roedelbronn
Youcai Wang
Lindgyan Zhu

University of Kentucky
Dan Dale
Chiranjib Dutta
Tim Gorringe
Wolfgang Korsch
Piotr Zolnierczuk

University of Lund
Kevin Fissum

University of Maryland
Elizabeth Beise
Herbert Breuer
George Chang

Nicholas Chant
Harry Holmgren
Philip Roos

University of Massachusetts, Amherst
Krishna S. Kumar
Luis Mercado
Juliette Mammei
Seamus Riordan
Jon Wexler

University of New Hampshire
Toby Badman
Trevor Bielarski
John Calarco
Greg Hadcock
Bill Hersman
Maurik Holtrop
Donahy John
Mark Leuschner
James Maxwell
Sarah Phillips
Karl Slifer
Timothy Smith
Ryan Zielinski

University of Regina
Garth Huber
George Lolos
Zisia Papandreou

University of Saskatchewan
Ru Igarashi

University of Science and Technology of China (USTC)
Yi Jiang
Hai-jiang Lu
Wenbiao Yan Yunxiu Ye
Zhengguo Zhao
Pengjia Zhu

University of South Carolina
Mike Paolone
Steffen Strauch

University of Virginia
Khem Chirapatpimol
Brandon Craver

Mark Dalton
Xiaoyan Deng
Gordon D. Gates
Gu Chao
Charles Hanretty
Ge Jin
Sudirukkuge Tharanga Jinasundera
Richard Lindgren
Jie Liu
Nilanga Liyanage
Vladimir Nelyubin
Blaine Norum
Kent Paschke
Peng Chao
Oscar Rondon
Kiadtisak Saenboonruang
Rupesh Silwal
William “Al” Tobias Diancheng Wang
Kebin Wang
Zhihong Yi
Zhiwen Zhao
Xiaochao Zheng
Jiayao Zhou

University of Washington
Diana Parno

Yamagata University
Seigo Kato
Hiroaki Ueno

Yerevan Physics Institute
Sergey Abrahamyan
Nerses Gevorgyan
Edik Hovhannisyan
Armen Ketikyan
Samvel Mayilyan
Artush Petrosyan
Albert Shahinyan
Hakob Voskanian

Past Members
Mattias Anderson
Maud Baylac
Hachemi Benaoum
J. Berthot
Tim Black
Alexander Borissov
Vincent Breton
Zhengwei Chai
Pibero Djawotho

Kim Egiyan
Catherine Ferdi
Robert Feuerbach
Mike Finn
Oliver Gayou
Charles Glashausser
Brian Hahn
Riccardo Iommi
Stephanie Jaminion
Lisa Kaufman
James D. Kellie
Ameya Kolarkar
Norm Kolb
Kevin Kramer
Elena Kuchina
Serguei Kuleshov
Jeff Lachniet
Geraud Lavessiere
Antonio Leone
Meihua Liang
Justin McIntyre
Wilson Miller
Pierre Moussiegt
Bodo Reitz
Rikki Roche
David Rowntree
Gary Rutledge
Marat Rvachev
Arun Saha
Neil Thompson
Dan Watts
Jingdong Yuan
Jingdong Zhou